TÉCNICO LISBOA

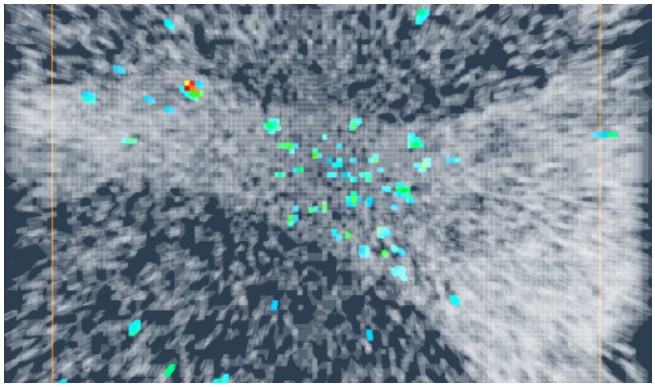

3D map of the distribution of metals in a cell:

Applications to the toxicity of nanoparticles

Miguel Serras Vasco

Thesis to obtain the Master of Science Degree in

Engineering Physics

Supervisors: Prof. Doutora Maria Teresa Ferreira Marques Pinheiro
Doutor Luís Manuel Cerqueira Lopes Alves

Examination Committee

Chairperson:	Prof. Doutora Maria Teresa Haderer de la Peña Stadler
Supervisor:	Prof. Doutora Maria Teresa Ferreira Marques Pinheiro
Member of the Committee:	Doutora Victoria Corregidor Berdasco

May, 2016

Acknowledgments

First and foremost, I wish to express my sincerest gratitude to Professor Maria Teresa Ferreira Marques Pinheiro and Professor Luís Manuel Cerqueira Lopes Alves, whose expert knowledge, patience and encouragement, since the earliest moment, have been a constant guiding presence in the development of this thesis.

I would also like to thank Professor Frank Watt for kindly providing an external analysis file, valuable for the validation of the methodology of the program. I am also grateful to Professor Rui Silva for its invaluable assistance in reverse engineering the structure of unknown data files and to all my colleagues at CTN, whose welcoming and friendly advice was of great value to the outcome of this thesis.

A word of gratitude is also due to my friends Miguel Furtado, Miguel Vasconcelos, Rui Martins and Tomás Nunes, whose friendly support was an unbroken source of stability not only for this thesis, but in all of my academic path.

Last but not the least, I would like to thank my family: my parents, Fernando and Lurdes, my sister Catarina, my brother-in-law João, my nephews Beatriz e Tomás and my girlfriend Rita for providing a constant origin of love, encouragement and support, abiding even in the most difficult moments.

Resumo

Atualmente, aplicações nanotecnológicas permitem o acesso a processos biológicos abaixo da escala celular. Contudo, a avaliação completa dos efeitos biológicos da proliferação destas nanopartículas requer o desenvolvimento de técnicas de imagiologia mais precisas. Rutherford Backscattering Spectrometry (RBS), uma técnica de análise de microssonda nuclear baseada na extração de informação da amostra a partir da energia do ião incidente retro-difundido após interagir com um núcleo na amostra, é capaz de simultaneamente identificar a matriz elementar de uma amostra desconhecida e obter o perfil em profundidade desses elementos.

Embora existam atualmente vários códigos numéricos disponíveis para análise de espectros de RBS, as opções de visualização dessa informação ainda se encontram por explorar. Para esta tese, foi desenvolvido um novo software computacional, o Micro-beam RBS Image Analyser (MORIA), que permite a criação do modelo da distribuição de um elemento da amostra num espaço 3D. MORIA utiliza a matriz da amostra, obtida por RBS, e a estimativa da perda de energia do projétil na amostra para calcular a profundidade da interação associada a cada evento, discriminada em canais de profundidade, tendo em conta o efeito da variação da secção eficaz de Rutherford e o aparato experimental.

A validação do modelo foi obtida através de várias análises de matrizes biológicas expostas a nanopartículas, usando iões ^{1}H e ^{4}He. Relativamente à visualização, existem vantagens no uso de iões ^{4}He, quanto a uma melhor resolução em profundidade para análises de superfície e sub-superficie, enquanto iões ^{1}H poderão ser usados para modelos mais globais, embora menos detalhados.

Palavras-chave: Software, RBS, Microssonda, 3D, Nanopartículas

Abstract

The development of nanoparticle applications have enabled the direct access to biological processes below the cellular scale. However, the full assessment of the biological effects of the proliferation of nanoparticles requires the development of improved imaging techniques. Rutherford Backscattering Spectrometry (RBS), an ion beam analysis technique based on the extraction of sample information from the energy of the back-scattered incident ion, after interacting with a target nucleus, is able to simultaneously identify the elemental matrix of an unknown sample and the depth profiling of those elements.

While there exists several computational code available for analysis of RBS spectra, the visualization options of such data are still under-developed. For this thesis, a new computational software was developed, the Micro-beam RBS Image Analyser (MORIA), that enables the presentation of the model of the distribution of a sample element in a 3D environment. MORIA uses the sample matrix, obtained through RBS, and the estimation of the energy loss of the projectile in the sample to calculate the depth of interaction associated to each event, sorted into depth channels, taking into account the effect of the variable Rutherford cross-section and the experimental setup.

The validation of the methodology was carried out through analysis of several biological samples exposed to nanoparticles, using ^{1}H and ^{4}He ions. For visualization purposes, there are advantages in the use of ^{4}He ions, concerning a better depth resolution for surface and sub-surface analysis, where as ^{1}H ions can be used for more global, but less detailed, models.

Keywords: Software, RBS, Microbeam, 3D, Nanoparticles

Contents

List of Tables

List of Figures

Nomenclature

A_{UL}	Atomic mass number of the element whose distribution in the sample space is to be modelled.
E_0	Initial kinetic energy of the incident particle.
E_1	Kinetic energy of the incident particle after scattering.
E_2	Kinetic energy of the nucleus after scattering.
E_{CM}	Center-of-mass energy.
E_{LL}	Surface energy of the element chosen to be the lower energy limit of the analysis.
E_{UL}	Surface energy of the element whose distribution in the sample space is to be modelled.
Er_i	Reduced energy in 1024 channels.
F_{A}	Anderson's Rutherford cross-section correction factor.
F_{LF}	L'Eculyer's Rutherford cross-section correction factor.
K	Kinematic factor.
K_{LL}	Kinematic factor of the element chosen to be the lower energy limit of the analysis.
K_{UL}	Kinematic factor of the element whose distribution in the sample space is to be modelled.
M_1	Mass of the incident particle.
M_2	Mass of the nucleus at rest.
N	Atomic density of the sample (atoms/cm^3).
Q	Measured number of incident particles.
Xr_i, Yr_i	Reduced coordinates in the $\Delta G \times \Delta G$ grid space.
$Y(t, \theta)$	Spectrum height of a given element at a given depth.
Z_1	Charge of the incident particle.
Z_2	Charge of the nucleus at rest.
Z_{UL}	Charge number of the element whose distribution in the sample space is to be modelled.

$[\epsilon]$ Stopping cross-section factor.

$[\epsilon]_T$ Total stopping power cross-section factor of the incident ion in the sample.

ΔG Grid dimension of the modelled distribution.

ΔS Scan size of the experimental run (μm).

Ω Solid Angle of the RBS detector.

$\bar{R}$ Average range of the incident particle in a given medium.

δE Energy resolution of the system.

δM_2 Mass resolution of the system.

δt Depth resolution of the system.

ϵ^k Stopping power of the incident ion in a single-elemental sample of element k.

ϵ_{in} Stopping power of the incident ion in the sample, evaluated at energy E_0, in the inward trajectory.

ϵ_{out} Stopping power of the incident ion in the sample, evaluated at energy $E_1 = K_{\text{UL}}E_0$, in the outward trajectory.

$\frac{dE}{dx}$ Stopping power of the incident particle in a given medium.

ϕ Atomic recoil angle in the laboratory frame.

ρ Density of the sample matrix.

ρ_k Density of element k in the sample matrix.

$\sigma_R, \frac{d\sigma}{d\Omega}$ Rutherford differential cross-section.

θ Scattering angle in the laboratory frame.

θ_{Max} Maximum scattering angle in the laboratory frame.

a_k Proportion (stoichiometry) of element k in the sample matrix.

e Electron charge.

k_{LL} Element chosen to be the lower energy limit of the analysis.

k_{UL} Element whose distribution in the sample space is to be modelled.

$n_{\text{ev}}^{\text{Max}}$ Maximum number of events in a single unit in the modelled distribution.

t^{Max} Maximum achievable depth by the analysis (nm).

t_{CH} Depth-channel calibration factor.

$t_{\text{CH}}^{\text{Max}}$ Maximum depth channel constructed by the analysis.

t_{E} Depth-energy calibration factor.

v_0 Initial velocity of the incident particle.

v_1 Velocity of the incident particle after scattering.

v_2 Velocity of the nucleus after scattering.

Chapter 1

Introduction

The emergence of nanotechnology as one of the most capable solutions to many global problems, remains one of the most fascinating facets of the evolution of engineering in the 21st century. Its accelerated progression brought a new paradigm to the scope in which the engineering of functional systems were achievable, addressing issues directly at the nanoscale (in the order of $1\text{-}100 \times 10^{-9}$m), something never-before imaginable. Currently, the application of nanoscale technology is being researched in a multitude of areas, ranging from electronics to chemistry, including space engineering and in multiple industries, such as in the food and textile production. Still, the most fascinating application of nanotechnology resides in the biology field.

The cellular biology field presents itself as a natural environment for the development of nanotechnology, due to the scale in which the innumerable cellular functions operate. Indeed, a typical radius of eukaryotic cell ranges from 10 to 100 μm, well above the nanometre limit. Thus, a precise study on the fundamental processes which occur in this setting, as well as deficiencies, can be done resorting to nanotechnology, such as the case of nanoparticles. Nanoparticles (NP) are defined as particulate dispersions or solid particles, with a size in the range of 10 to 100 nm, with tremendous applications in cellular biology, such as drug delivery [Mohanraj and Chen, 2006], therapy techniques [Hu et al., 2013] or anti-bacterial techniques [Han et al., 2009]. Due to their versatility, these particles are also used in other areas. In the Material and Textile industry, copper (Cu) nanoparticles are used in order to increase the tensile strength and the dyeability to different dyes of fibers, as well as to provide anti-bacterial protection to the fabric [Sedighi et al., 2014]. Hence, it becomes evident not only the ever-rising proliferation of these particles in the everyday life, but also the increasing contact to which living beings are subjected to and the potential for considerable environmental pollution.

The biological toxicity of nanoparticles is currently one of the primary concerns undermining the technology's expansion. Due to their intrinsic properties, such as their size and composition [Chang et al., 2012], nanoparticles can easily penetrate the cellular environment and induce high levels of citotoxicity and direct damage to the cell's DNA. The combination of these negative effects may lead to the cell's *apoptosis* (programmed cellular death), and the possible widespread nature of this phenomena is a major source of concern by the scientific and political community, regarding environmental pollution and

biological interaction with NP. Ongoing international research on the biological effects of NP is being carried out, specifically on the quantization, transport, and depth profile of NP in cells, and with that goal in mind high resolution imaging techniques are fundamental.

1.1 State-of-the-art

1.1.1 Imaging Techniques

The general goal of imaging techniques is to gain a fundamental understanding of the inner structure of matter, which requires the ability to perform the analysis across all length and time scales. As such, inumerous techniques were developed accordingly to the necessities of the analysis, and certainly a profound discussion of the methodology of each is beyond the scope of this introduction. Thus, due to their similarity with the methodology presented in this thesis, only electron imaging techniques will be discussed.

One of the most notable and widespread applications of particle imaging is undoubtedly electron microscopy (EM), which has become an important methodology to determine the morphology, crystal and defect structure, elemental composition and electronic properties of materials. Since its development in 1931 by Ernst Ruska [Knoll and Ruska, 1932], EM has become a key methodology in the material analysis field, whose main advantage over conventional microscopy concerns the creation of a much higher-resolution probe, due to the decreased electron wavelength in comparison with that of visible light. It uses a focussed electron beam, which, during its interaction with the unknown sample matrix, generates various signals: inelastically or elastically scattered electrons, Auger Electrons (AE) and X-rays, amongst others. One of the main disadvantages of Electron microscopes is the necessity of a vacuum environment, both to enable electron production and transmission to the sample, in a effort to minimize unintended scattering that would hinder the quality of the analysis. As such, samples must be stable in vacuum state, prepared in solid state or in liquid emulsion. Yet, for imaging purposes the greatest difficulty in a complete sample analysis arises from the short range of electrons in a biological sample, as seen in Figure 1.1a, and as such the quality of analysis of the sub-surface layers of a sample is considerably degraded.

The usual electron wavelength used in EM, depending to its energy, ranges between 0.4 and 4 pm and, as such, analysis and detection of individual atoms should be possible. However, experimental resolution is still 20$\times$ worst than the theoretical limits, due to aberrations in EM lenses from non-null gradients of field strength, which alters the focusing of the electrons passing through the lenses as a function of their distance to the axis, resulting in a spread of focal distances (spherical aberration). However, recent developments [Muller et al., 2008] in aberration-corrected probe-forming optics can push EM to resolutions in the order of 50-100 pm.

Several modes of application of EM were developed in order to address the particular aspects of each analysis. For analysis of thin samples, Transmission Electron Microscopy (TEM) is widely used. TEM is based on the analysis of the electrons, formed in a wide and parallel beam, transmitted through the

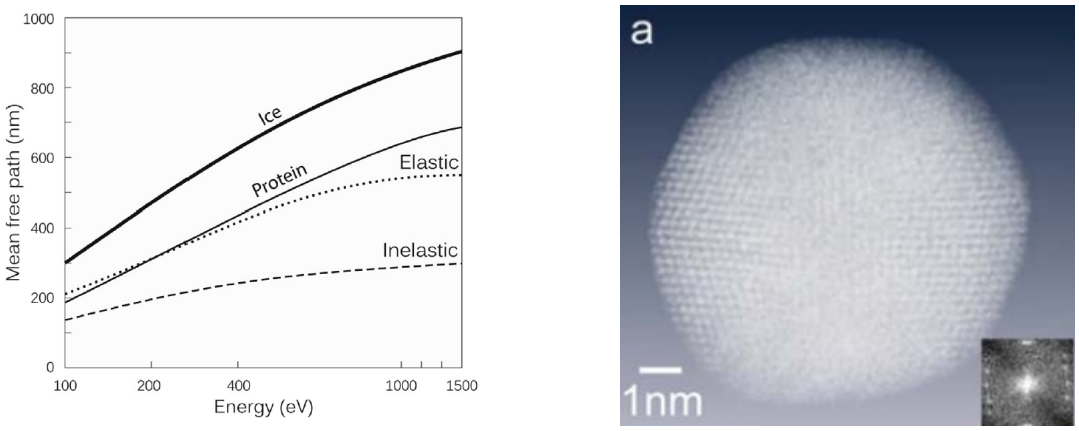

(a) (b)

Figure 1.1: (a) Mean free path for ice and protein material and the fraction of unscattered, single and multiple scattered electrons in ice for 400 keV electrons; (b) 3D volume renderings of a nanoparticle, using electron tomography. Adapted from [Scott et al., 2012].

sample, thus forming the high resolution image. Scanning Transmission Electron Microscopy (STEM) is a variation of the previous technique, in which the electron beam is focussed in a spot, which is moved across the surface of the sample. The same raster mechanism can also be used in conventional EM for the analysis of surface regions of thick samples.

Electron microscopy can also be used for 3D reconstruction, with atomic level resolution, and mapping of individual atoms in a structure. One emerging technique, Electron Tomography (ET), is based on the 3D spatial reconstruction of a series of projection images, attained by a physical tilt of the sample, which are subsequently correlated accordingly to the tilting angle. The main disadvantage of the method arises from the difficulty in precisely tilting the sample in order to construct the image. In order to achieve atomic level resolutions in ET images, the sample must consist in a perfectly crystalline object, sized in the order of nanometres. However, recent developments [Scott et al., 2012] have been able to reconstruct the interior of a 10-nm gold particle, achieving sub-nanometre resolution, as seen in Figure 1.1b. The technique was also used for the evaluation of the changes in positions of metal atoms over time, using time-resolved images [Van Aert et al., 2011]. For a more complete review of sample preparation, instrumental and computational methodology, along with validation tools, concerning this technique, please refer to [Fernandez, 2012].

Several other methodologies in EM exist, as well as inumerous applications of X-rays, and even magnetic fields, in order to probe the inner structure of a generic unknown sample. However, few are able to combine nanometre probe-formation with precise quantification of the elemental composition of an unknown matrix and the ability to examine the sub-surface layers of a thick sample, retrieving the depth-dependent profile of those elements, as ion beam techniques.

1.1.2 Ion Beam Analysis (IBA)

One of the first evidences of the existence of ion beams was brought up by Eugen Goldstein [Goldstein, 1898] who, in 1886, observed the existence of canal rays (*Kanalstrahlen*), using a discharge Crooks

tube. Goldstein had unknowingly made the first observation of packets of positive charge and the effects of the application of a high electric potential to a gas. Later, in 1899, Wilhelm Wien observed the deflection of the canal rays by strong electric and magnetic fields, constructing a device that could separate the rays, as a function of their charge-to-mass ratio (Q/m). This device was further improved by J.J. Thompson, thus creating the precursor to the mass spectrograph. This marked the first contribution of the knowledge of ion beams to the material analysis field, and the start of the ever-increasing contribution of Nuclear Physics to other scientific areas.

The effective application of ion beams to sample analysis began in the 1960s using the, by then, *mature* knowledge of ion properties, mostly discovered in the beginning of the twentieth century. The study of these properties, such as Rutherford Scattering [Geiger and Marsden, 1913], Channeling [Stark, 1912], and ion induced X-ray emission [Chadwick, 1912], proved to be fundamental not only in the interpretation of the analysis results, but also in the construction of the many experimental apparatuses. The first demonstration of ion induced activation analysis was preformed by Seaborg and Livingood in 1938 [Seaborg and Livingood, 1938], a precursor to Rutherford scattering analysis, reported by Rubin. The same author, in 1957, [Rubin et al., 1957] demonstrated the use of ion-ion and ion-gamma reactions for sample analysis, reported in "Chemical Analysis of Surfaces by Nuclear Methods", paving the way for the generalised use of ion beams in the material analysis.

The underlying principles behind many of the different analytical techniques that use ion beams are the same. Initially, a beam of ions, with energy in the order of MeV, is aimed at the target, which will then penetrate the sample, losing energy along their trajectories, at a known rate, through collisions with nuclei and electrons. Due to these interaction, there is a probability, ruled by the respective interaction cross-section, of emission of an output regarding the sample structure, which can then be detected, collected as a spectra and analysed. This information can give precise details on the sample's properties, such as atomic structure, matrix composition or elemental depth distribution. Indeed, it is the type of collected information that distinguishes the different analytical techniques, which is taken in account in the choice of experimental set-up and in the analysis procedure. A list of the most common MeV ion beam analytical techniques is presented in Table 1.1.

Note that many of the techniques can be applied simultaneously, installing their specific instrumentation in the same sample chamber, thus offering a better depiction of the sample's characteristics. Indeed, one of the most commonly used techniques as a material analysis tool is RBS (Rutherford Back-Scattering), due to its ability to simultaneously give information regarding the sample's elemental structure and the depth profile of its composition, two fundamental properties to fully describe a material. Thus, a more profound incursion on the technique, is needed to understand their potential as an insight tool in biological analysis and NP identification, and is presented in Chapter 2.

1.1.3 Nuclear Microprobe Instrumentation

One of the advantages of using ion beam techniques for material analysis is the common experimental apparatus that many of them share, only needing specific electronics at the sample chamber level. Thus,

Table 1.1: Commonly used Ion Beam techniques

Technique	Applications	Elements Detected	Depth Probed (μm)	Depth Resolution (nm)	Depth Profiling
RBS	Thin film composition and thickness	B - U	1 - 2	20 - 100	Yes
PIXE	Element identification Impurity analysis	Al - U	Up to 10	poor	No
NRA	Profiling of light elements in a heavy matrix	B, C, Li, N, O, F	1 - 5	50 - 100	Yes
Channeling	Lattice location of impurity in a crystal	B - U	1 - 2	20 - 100	Yes

the discussion on the accelerator and beam line equipment is common for many ion beam methods, including RBS and PIXE. The first essential component of any microprobe facility is the accelerator, responsible for boosting the ions until a determined kinetic energy. For a functional micropobe, this unit should provide a stable beam current and a low beam energy spread, less than 100 eV per MeV, in order to obtain minimal probe resolution. The most common used accelerator are electrostatic accelerators, such as Van de Graaff accelerators and Tandem accelerators, which are able to boost protons and light ions in the range of 1-3 MeV and to produce currents in the order of 1 μA, sufficient for all analysis techniques.

The most widely used electrostatic accelerator is the Van de Graaff accelerator, first demonstrated by Robert J Van de Graaff in 1931, which was able to produce a 1 MV potential difference between its terminals. The main component of the accelerator is the high voltage generator, a continuous conveyor belt that carries electrostatic charges up to a hollow terminal. The DC potential is maintained by a charge continuously flowing back into the ground. Positive ions are extracted from a RF oscillator ionized gas, present inside the terminal, which are subsequently accelerated to ground potential along the accelerator tube. An evolution of the single-ended accelerators are tandems. In these equipment, acceleration is done in two stages: first an incident negative ion beam is accelerated to the center of the tube, at a positive potential, where a stripper channel (usually a thin carbon foil) is used to strip the electrons from the ions. Subsequently, the new positive ion beam is once again accelerated over the same potential difference V. This mechanism allows the production of ions with $(n+1)V$ kinetic energy, where n is the ion's positive charge state, obtained after the stripper channel. A further advantage of the tandem accelerator is that the ion source is not inside the terminal, thus simplifying its handling, and that this unit can be much more compact due to needing a lower potential, when compared with a single-ended accelerator, for producing ions of the same energy. However, the presence of a stripper channel

degrades the brightness of the final beam and increases the energy spread, due to straggling, which can result in sub-optimal probe resolutions. Still, tandem accelerators are capable of achieving good resolutions, as seen in the Oxford nuclear micropobe [Grime and Watt, 1993] that produces currents in the order of 100 pA of MeV ^{1}H ions focused into 330 nm.

After its acceleration, the beam must be transported into the microprobe beam line, which is commonly done resorting to a bending magnet. This component can be a simple dipole field, or double-focusing 90º spectrometer magnet, and is also responsible for reducing the momentum spread of the beam entering the beam line. The next components in the beam line are the object and aperture collimators, responsible, respectively, for defining the beam area to be demagnified and limiting the divergence of the beam that enters the probe-forming lens system, while reducing the beam current. These units can consist of either slits or diaphragms, with a range of openings possible, from 300 μm to fractions of micron, which can be important for low-beam current techniques, such as proton beam writing. A considerable problem for the object collimators is overheating, which can cut-off the beam in small slit openings, due to thermal expansion of the slits, and can deteriorate the surface of the collimators, inducing random scattering [Fischer, 1988] and thus reducing the resolution of the probe. This can be resolved using a monitor Faraday cup located upstream of the object collimator, with a small opening to admit the beam into the collimator, which can reduce the beam current to a few nanoamps. Regarding the aperture collimator, its size is chosen accordingly to a number of factors, such as the brightness of the ion beam, the scattering cross-section of the interaction to be analysed and the size of the desired probe. For a typical beam brightness, an aperture size from 4 mm to tens of microns should be used [Breese et al., 1996].

The beam then enters the probe-forming lens system, usually consisting of two, or more, precision quadropole lenses, responsible for the demagnification of the beam, thus forming the probe. In order to minimize undesirable magnetic field components, responsible for the existence of chromatic aberrations, mechanical tolerances in its production should be less than 25 μm [Breese et al., 1996]. Although the design of the lens system must take into account various factors, such as the performance of the accelerator and the dimensions of the beam line, the goal of this component is common to most setups: achieve the strongest demagnification possible, in order to ensure the highest resolution probe. Obviously, this is also a function of the alignment of the lenses and their focus, yet this problem can be overcome by careful mechanical alignment and small adjustments in the lens field [Legge et al., 1979]. In Table 1.2 is presented a list of several microprobe experimental setups, as well as their parameters.

After being focused, the probe enters the sample chamber and interacts with the target. The design of the sample chamber must take into account not only the numerous, and interchangeable, particle and radiation detectors, but also the wide range of characteristics of the different samples. A cylinder configuration, with fixed position vacancies for the detectors and an optical microscopes, used to provide visual information on the focusing of the beam and on relevant areas on the sample, mounted on a rotating turret, is most used in micropobe systems. This configuration improves the versatility of the chamber, as it allows the effortless positioning of the detectors most relevant for a given measurement at their optimal positions.

Table 1.2: List of Nuclear Microprobe systems, containing the parameters regarding accelerator and ion source types, normal proton beam brightness B_n and lateral resolution. Values taken from [Pelicon et al., 2014], [Shariff et al., 2005] and [Mous et al., 1997].

Facility	Accelerator	Ion source	E (MeV)	B_n (A m^{-2} rad^{-2} eV^{-1})	Lateral resolution (μm)
CTN	Single-ended 3.1MV	RF (H^+)	2	0.8	1.5×1.5
Lund	Single-ended NEC 3UH	RF (H^+)	2.55	7.0	0.2×0.5
Oxford	Tandem NEC 5SDH-2	RF (H^+)	3	0.6	1×1
Singapore	Single-ended HVEC AN2500	RF (H^+)	2	30	0.02×0.03
Ljubljana	Tandem HVEE 2MV	Duoplasmatron (H^+)	2	1.8	0.8×0.8
Gradignan	Single-ended HVEE 3.5MV	RF (H^+)	2.25	26	$<$0.3

It is at the detector level that the differences in instrumentation between the different analytical techniques appear. For PIXE, a semiconductor Si(Li) detector is mostly used, due to their superior energy resolution, of 160 eV or better, when compared to scintillators or proportional counters, and energy dispersive nature. An intrinsic Ge detector can also be used, but its increased energy resolution and efficiency in the high energy X-ray range makes it more sensitive to backgrounds arising from particle induced γ emission in the sample. Some of the main disadvantages of Si(Li) semiconductor detectors are the background noise, emerging from the pre-amplification of the reduced signal produced by the electron-hole creation process, and the thermal noise, due to leakage current in the reverse biased diode at room temperature. Still, this type of detector remains the best option for PIXE analysis, until the standardization of improved alternatives, such as Silicon Drift Detectors (SDD) which combine high energy resolution, with high count rates and the ability to operate at room temperature or with moderate cooling, achievable through Peltier cooling [Lechner et al., 2003]. Other complementary analysis, in some particular PIXE studies, can be carried out using semiconductor based microcalorimeters [Silver et al., 1996] or superconductor tunnel junction cooled detectors [Frank et al., 1998].

Commonly in RBS, a surface barrier detector is used as a particle detector. More elaborate solutions for RBS experiments include time-of-flight (TOF) detectors, which determine the energy of the ions trough their velocity, by measuring the time of transversing a known distance [Knapp et al., 1996, Takayama et al., 2003]. The associated chain of electronics is shared by both types of detectors: preamplifier, responsible for generating a pulse with height proportional to the energy of the detected signal, spectroscopic amplifier, responsible for shaping and further amplifying the signal, and a multichannel analyser (MCA), responsible for the digitalization of the signal in order to be analysed. For the extraction of information through spectral analysis, several computational simulation codes have been created, specific

for the RBS or PIXE analysis. The microbeam facility at CTN uses an Oxford Microbeam system which contains a 8-channel ADC interface, thus allowing the simultaneous use of up to 8 detectors in the sample chamber, coupled to an ADC trough a multiplexer, in which each event is sorted into 4096 energy channel spectra and whose position, given by the position of the beam at the moment of detection, is sorted into 256 x 256 pixel elemental maps. The data analysis is carried out in a Oxford Microbeam proprietary software OMDAQ [Grime and Dawson, 1995], which presents full details of the experimental conditions, sample, detectors, beam parameters amongst others, and enables PIXE and RBS data analysis by including a library of X-ray energies to allow identification of peaks in PIXE spectra and simulation and fit of RBS spectra. A summary of the available simulation codes for each technique is presented in [Agency, 2000].

It is also important to note that the entire beam line must be in vacuum, in order to minimize both the degradation of the energy of the beam as well as the straggling effect, which produces a beam halo responsible for the deterioration of the spatial resolution of the probe. With a vacuum of 10^{-5} Pa, the proportion of $^1H_2$ molecular ions that was broken up over a distance of 8.6 m was around 0.3% [Bench, 1991]. Thus a vacuum of under 10^{-4} Pa is advisable in microbeam measurements. This limit is achieved in most experimental setups by the combination of two vacuum pumps: an initial rotary vane pump, reducing the pressure to 10^{-1} Pa, and a turbomolecular or ion pump, to reduce the pressure even further to 10^{-6}-10^{-7} Pa. While ion pumps have the advantage of producing limited vibration, a characteristic fundamental in achieving high-resolution probes, turbomolecular pumps are still widely used due to their fast starting mechanisms and easy operation.

1.1.4 Applications of IB to Biological Studies

Despite the importance of synthetic material analysis, ion beam research on biological samples have been attaining importance, not only due to improvements on the imaging resolution obtained by the experimental setups, but also due to the increased conscience of the influence of nanoscale phenomena, in both biological and biomedical fields. Thus, the microprobe solution seems natural to address the need for sub-micron resolutions and precise quantitative results. Once more, the simultaneous employment of PIXE and RBS techniques in sample analysis is able to give a precise stoichiometric view of the sample's matrix but also give a depth profile of the matrix elements.

The employment of these techniques have been crucial for various studies. Research on Ion-induced fluorescence imaging of endossomes [Norarat et al., 2013], used a combination of proton induced fluorescence (PIF) and direct Scanning Transmission Ion Microscopy (STIM) for sub-cellular structural imaging, with resolutions under 150 nm for PIF and under 50 nm for proton STIM, thus being able to improve fluorescence imaging beyond optical diffraction limits, a goal fundamental for cellular studies. It is also reported the utilization of PIXE and RBS on the estimation of the mass of a given element on a cellular level, with sensitivity in the order of 10^{-12} g [Ogrinc et al., 2013], and on the spatial distribution of metals in a simple organism [Mendes Godinho et al., 2013]. The multitude of studies using ion beams prove the versatility of the method, and their sophistication has reached a point where studies on direct

imaging of nanoparticles are possible.

Studies using nuclear imaging techniques on the toxicity of titanium dioxide (TiO_2) NPs, present in sunscreen cosmetic additives, solar cells and water treatment agents, have proven the alteration of the being's physiology, due to their accumulation in the organism. Another study by [Godinho et al., 2014] showed the effect of the exposure to metal overload on whole cells of diatom *Coscinodiscus eccentricus*, examining consequences to cellular toxicity, tolerance mechanisms, and metal fate in the environment, using nuclear microprobe techniques. More recently, it has been reported [Chen et al., 2013a] that microprobe analysis applied to the identification and quantization of gold NP was able to achieve a 20 nm spatial resolution and obtain direct evidence of the transport mechanism involved in the cellular entry of NP. Using a combination of RBS and STIM, the group was able to identify the NP, but also to ascertain their depth in the cellular environment with sub-micron resolution, being able to differentiate between NP at the surface of the cell and NP inside the cell. This technique could allow the determination of the effectiveness of the drug delivery, using a modified gold NP, in terms of distribution and dose, but also enable further studies on the toxicity of NP, a research topic fundamental for a safe widespread use of nanotechnology. In this work, a 3D map of the distribution of metals in cells, obtained from ion beam analysis, is presented and its implications on the toxicity of nanoparticles is discussed.

Chapter 2

Rutherford Backscattering Spectrometry (RBS)

A complete description of an unknown sample is the utmost intention of any material analyst. To this goal, a nuclear microbeam facility is often used, due to its ability to accommodate several different methods of information extraction within the same experimental apparatus. In a microbeam analysis, the sample's structure and properties are determined from the interactions of the beam's ions and the different atoms that compose the unknown sample. As mentioned in Chapter 1, in Rutherford Backscattering Spectrometry (RBS) sample information is extracted from the energy of the back-scattered incident ion, after interacting with a target nucleus, which is recorded with an energy sensitive detector, such as a solid state detector. From the energy distribution of the different elements that compose the unknown matrix, the sample's structure can be inferred. In this chapter, the technique is presented, with considerations regarding the kinematics of elastic collisions and the importance of the kinematic factor (Chapter 2.1), the Rutherford Cross-section (Chapter 2.2.1) and energy-dependent deviations to it (Chapter 2.2.2), the ion energy loss mechanisms (Chapter 2.3), including the different regimes of electronic energy loss (Chapter 2.3.1) and the phenomena of ion range (Chapter 2.3.2). Finally, some considerations regarding the procedures in RBS analysis are made in Chapter 2.4.

2.1 The Kinematic Factor K

The fundamental basis of RBS is the detection and analysis of the projectile ions which are back-scattered, after interacting with the atomic nuclei which compose the sample's matrix. This process can be thought as a two-body elastic collision between isolated particles and thus an incursion in the kinematics of such process is needed, which, along with the energy transfer between the bodies, can be fully determined resorting to the conservation of energy and conservation of momentum, valid assumptions in an elastic interaction.

The geometry of the elastic collision process is presented in Figure 2.1, along with the notation used in this dissertation. When the incident ion, of mass M_1, charge Z_1 velocity v_0 and energy $E_0 = 1/2 M_1 v_0^2$,

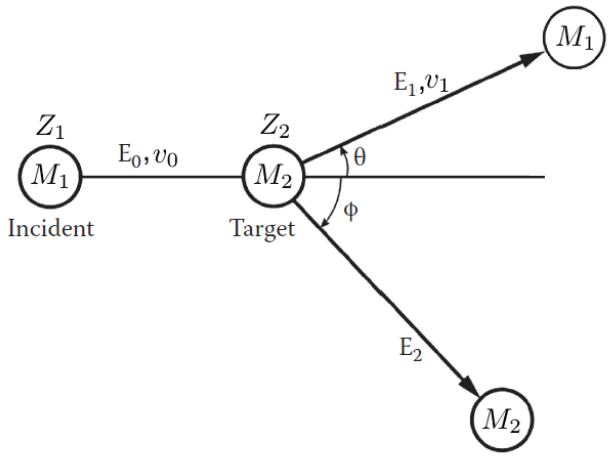

Figure 2.1: Kinematics of the elastic collision between a projectile particle of mass M_1, charge Z_1, and kinetic energy $E_0 = 1/2 M_1 v_0^2$ and a nucleus at rest of mass M_2 and charge Z_2. Adapted from [Nastasi et al., 2014].

interacts with an target atom at rest, of mass M_2 and charge Z_2, the ion is scattered through an angle θ, with an atomic recoil angle of ϕ. Depending on the angle of scattering, and recoil, after the energy and velocity of the ion are given by E_1 and v_1, respectively, and can be determined by employing the conservation of kinetic energy (equation 2.1) and the conservation of longitudinal (equation 2.2) and transverse (equation 2.3) momentum, expressed by:

$$\frac{1}{2}M_1 v_0^2 = \frac{1}{2}M_1 v_1^2 + \frac{1}{2}M_2 v_2^2 \tag{2.1}$$

$$M_1 v_0 = M_1 v_1 \cos\theta + M_2 v_2 \cos\phi \tag{2.2}$$

$$0 = M_1 v_1 \sin\theta - M_2 v_2 \sin\phi \tag{2.3}$$

Adding equations 2.2 and 2.3 and substituting in equation 2.1, it is possible to obtain the ratio of ion velocity after the interaction:

$$\frac{v_1}{v_0} = \frac{M_1}{M_1 + M_2}\cos\theta \pm \left[\left(\frac{M_1}{M_1 + M_2}\right)^2 \cos^2\theta + \frac{M_2 - M_1}{M_1 + M_2}\right]^{1/2} \tag{2.4}$$

Regarding equation 2.4, for projectile masses greater than the target's mass ($M_1 > M_2$), the term in square brackets can vanish for $\theta = \theta_{\text{Max}}$, where the maximum angle of scattering θ_{Max} obeys:

$$\cos^2\theta_{\text{Max}} = 1 - \frac{M_2^2}{M_1^2} \tag{2.5}$$

Thus, $\theta_{\text{Max}} \in [0, \pi/2]$ for $M_1 > M_2$. As such, backscattering spectrometry is unable to detect in the sample elements with lower mass than that of the species of ion used, since a projectile colliding with a target of equal, or lower, mass cannot be backscattered. In order to address this problem, light elements such as ^{4}He and ^{1}H are often used for the ion beam. In extreme cases, forward spectrometry can also

be employed for increased sensitivity to light elements. On the other hand, for $M_1 < M_2$, and taking the positive root of equation 2.4, the energy ratio after the interaction can be given by:

$$\frac{E_1}{E_0} = \left[\frac{(M_2^2 - M_1^2 \sin^2\theta)^{1/2} + M_1 \cos\theta}{M_1 + M_2}\right]^2 \tag{2.6}$$

Rewriting equation 2.6, it is now possible to define the kinematic factor K_{target} as the ratio of projectile energies:

$$K_{\text{target}} = \frac{E_1}{E_0} = \left[\frac{[1 - (M_1/M_2)^2 \sin^2\theta]^{1/2} + M_1/M_2 \cos\theta}{1 + (M_1/M_2)}\right]^2 \tag{2.7}$$

Where the subscript is used to indicate the intrinsic dependence of this factor on the target element. Hence, for a known ion mass M_1, the energy loss of the incident ion, after elastically colliding with the target atom, becomes a function only of the scattering angle θ and of the target's mass M_2. As such, the kinematic factor is the fundamental parameter of RBS analysis since, for a fixed scattering angle θ, given by the detector's angle, it allows a precise identification of the unknown sample element. The value of K_{target} as a function of M_2 for a scattering angle $\theta = 60$ and as a function of θ for Carbon ($M_2 = 12$, $Z_2 = 6$), for proton ^{1}H and helium ^{4}He beams, is presented in Figures 2.2a and 2.2b respectively.

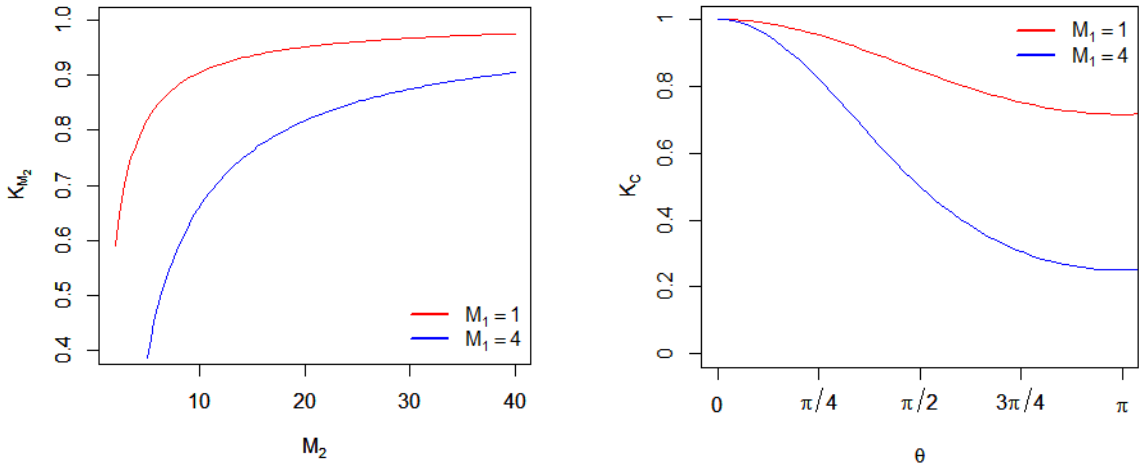

(a) K_{target} as a function of M_2, with $\theta = 60^{\text{o}}$.

(b) K_{target} as a function of θ, with $M_2 = 12$.

Figure 2.2: K_{target} as a function of M_2 (a), and as a function of θ (b), for a proton ($M_1 = 1$), and helium ion ($M_1 = 4$) projectile.

As seen in Figures 2.2a and 2.2b, the kinematic factor varies considerably as a function of θ and M_2. The ion energy loss, due to the elastic collision, is much more significant for scattering angles $\theta \sim \pi$, as should be expected since this limit corresponds to a head-on-collision with the target atom. Also expected, as seen in Figure 2.2a, is the increase energy loss relation with heavier projectiles. However, the sample's matrix regularly contains more than one type of atom, and thus arises the question of the identification of both elements and their separation in the RBS spectrum. For fixed θ, the energy separation between two elements ΔE_1 is given by:

$$\Delta E_1 = E_0 \left(\frac{dK}{dM_2}\right) \Delta M_2 \tag{2.8}$$

derived directly from the kinematic factor (equation 2.7), with ΔM_2 the mass difference between the two elements. The increase in energy separation with increasing beam energy E_0 is presented in Figure 2.3.

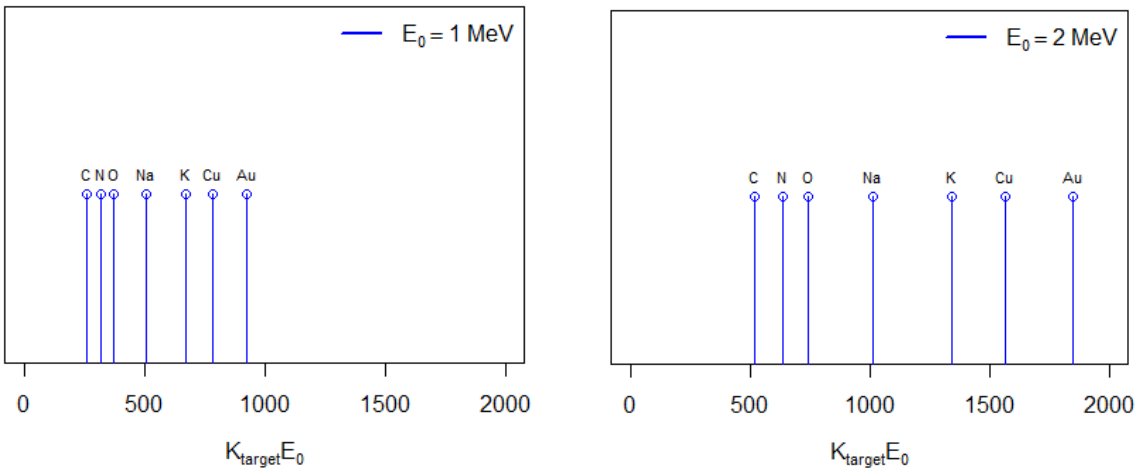

Figure 2.3: $K_{\text{target}}E_0$ surface-energy for various elements, for a Helium ion projectile ($M_2 = 4$), scattered with $\theta = 160^{\text{o}}$, with $E_0 = 1.0$ MeV (a) and $E_0 = 2.0$ MeV (b).

The mass resolution of the system δM_2 can be obtained by setting ΔE_1 to the minimum energy separation that can be resolved experimentally:

$$\delta M_2 = \frac{\delta E}{E_0 \left(\frac{dK}{dM_2}\right)} \tag{2.9}$$

The mass resolution varies considerably with the depth at which the interaction occurred: at the sample surface, δM_2 is mainly determined by the detector energy resolution, while at deeper layers the dominant component of δM_2 is energy straggling (which is discussed in Appendix A). Once again, the mass resolution can be increased through the usage of a heavier projectile. However, the increased mass on the projectile may lead to decreased sensibility to lighter elements, as presented in equation 2.5, and decreased detector resolution.

2.2 Scattering Cross-section

The interaction of the innumerate ions of the beam with the atoms of the sample's matrix is a statistical process. As such, the degree of energy transfer between this two components and the scattering angle are fundamental attributes of the interaction, which can be described by the differential cross-section. This function quantifies the probability of transferring energy E, from the interval E to $E + dE$, through the stopping cross-section, or the probability of scattering the projectile by an angle θ_c, from the range θ_c and $\theta_c + d\theta_c$, through the scattering cross-section, which will be discussed in this section for the Rutherford case.

2.2.1 Rutherford Cross-section

Rutherford scattering refers to the elastic scattering of charge particles by the Coulomb interaction, with the projectile described by mass and atomic number M_1 and Z_1 and the target nucleus is described by mass and atomic number M_2 and Z_2. The inter-atomic potential for Coulomb interaction is given by:

$$V(r) = \frac{Z_1 Z_2 e^2}{r} \tag{2.10}$$

in c.g.s. units, with r the distance between the two nuclei. The Coulomb interaction gives rise to the Coulomb angular differential scattering cross section, also known as the Rutherford differential cross section which, in the laboratory frame of reference, is given by [Nastasi et al., 2014]:

$$\sigma_R = \frac{d\sigma(\theta)}{d\Omega} = \left(\frac{Z_1 Z_2 e^2}{4E}\right)^2 \frac{4}{\sin^4\theta} \frac{\{[1-((M_1/M_2)\sin\theta)^2]^{1/2} + \cos\theta\}^2}{[1-((M_1/M_2)\sin\theta)^2]^{1/2}} \quad (mb/sr) \tag{2.11}$$

with θ the scattering angle and E the projectile's kinetic energy. Thus, the scattering angle θ takes a predominant role in the value of the Rutherford cross section. The value of σ_R as a function of θ, for an interaction of a helium ion ^{4}He ($Z_1 = 2; M_1 = 4$) with an Carbon atom ($Z_2 = 6; M_2 = 12$), a common element in biological matrix, is presented in Figure 2.4.

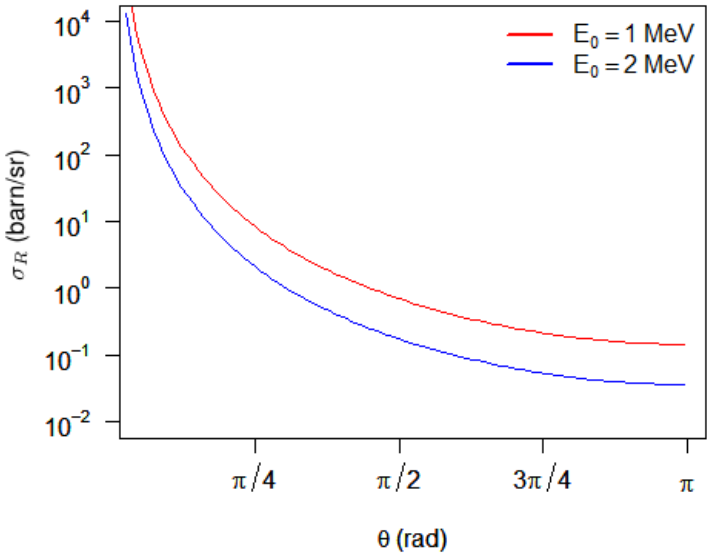

Figure 2.4: Value of the Rutherford differential cross section as a function of the scattering angle θ, for a carbon atom ($Z_2 = 6; M_2 = 12$), with a projectile helium ion ($Z_1 = 2; M_1 = 4$) with $E_0 = 1.0$ MeV (red) and $E_0 = 2.0$ MeV (blue).

It is visible from its angular dependence, presented in Figure 2.4, that the largest cross sections are for events of small-angle scattering. Taking $E_0 = 2.0$ MeV and a scattering angle of $\theta = 5°$, in the case of the same interaction of Figure 2.4, the value of the scattering cross-section is $\sigma_R(\theta = 5°) \approx 1.3 \times 10^4$ mb/sr, almost 10^6 times the magnitude of the cross-section for $\theta = 175°$ ($\sigma_R(\theta = 175°) = 0.03$). In fact, the small value of the cross-section for backscattered events, which may lead to long acquisition times experimentally, is certainly one of the disadvantages of the RBS technique. However this situation can be improved by an increase in the current reaching the sample, at a cost of a decrease in the beam's

spatial resolution, through the opening of the aperture slits.

2.2.2 Non-Rutherford Cross-section

In order to assume that the interaction between the incident ion and the sample's atom is purely Rutherford, and thus the scattering cross-section is purely Rutherford, the velocity of the ion must be sufficiently large for it to penetrate the inner-most atomic electron orbitals. As such, the interaction could be interpreted as the repulsion between two nucleus of positive charge.

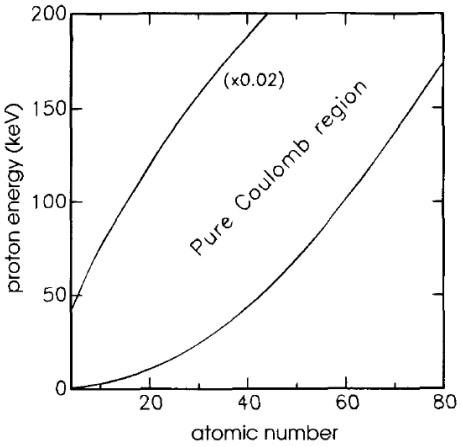

Figure 2.5: Representation of the range of energies in which the cross-section can be treated as pure Rutherford. Taken from [Breese et al., 1996].

However, experimental studies have shown to exist a considerable deviation from the Rutherford cross-section at both high and low-energy limits, as shown in Figure 2.5 for a proton beam. The low energy deviation is caused by partial screening of the nucleus charge by the inner electrons, which introduces a screening function χ in the Coulomb potential:

$$V(r) = \frac{Z_1 Z_2 e^2}{r}\chi \tag{2.12}$$

With $\chi = 1$ for the unscreened Coulomb potential case. Many different screening functions exist, yet all characterize the spatial variation of the potential as a function of a defined screening radius, usually the Thomas-Fermi screening radius $a_{\text{T-F}}$, given in equation 2.13

$$a_{\text{T-F}} = \frac{0.885\, a_0}{\left(Z_1^{1/2} + Z_2^{1/2}\right)^{2/3}} \quad (\text{Å}) \tag{2.13}$$

where $a_0 = 0.53$ Å is the Bohr radius and $a_{\text{T-F}}$ usually takes values between 0.1 and 0.2 Å. It becomes important to quantify this low-energy limit not only in terms of atomic distance but also in terms of the incident ion's energy. For the unscreened Coulomb potential to be valid, the energy E of the ion must allow it to approach a radius r_d greater than the radius of the K electron shell, given approximately by a_0/Z_2. So, for any approach radius:

$$r_d = \frac{Z_1 Z_2 e^2}{E} \tag{2.14}$$

Taking r_d the radius of the K electron shell, a lower limit for the energy of the incident beam E_{min}, for a pure Coulomb interaction, can be deduced:

$$E_{\text{min}} > Z_1 Z_2^2 \frac{e^2}{a_0} \tag{2.15}$$

For a helium ion interacting through a pure Coulomb potential with a Carbon atom ($M_2 = 12$, $Z_2 = 6$), the value of the Thomas-Fermi screening radius is $a_{\text{T-F}} = 0.19$ Å, which translates into a minimum beam energy of $E_{\text{min}} = 5.44$ keV.

As expected, the screening effect on the Coulomb potential at low energies also affects the value of the scattering cross-section. This screening is taken into account through a correction factor F, such that the screened Rutherford cross-section σ_{SR}:

$$\sigma_{SR} = F\sigma_R \tag{2.16}$$

Experimental results indicate that the screening correction can be given, with some precision, by the L'Ecuyer factor [L'Ecuyer et al., 1979]:

$$F_{\text{L'E}} = 1 - \frac{0.049 Z_1 Z_2^{4/3}}{E_{\text{CM}}} \tag{2.17}$$

where E_{CM} is the center of mass energy (keV), given by:

$$E_{\text{CM}} = M_2 \frac{E_0}{M_1 + M_2} \tag{2.18}$$

with E_0 the energy of the incident beam (keV). The L'Ecuyer factor (2.17) is a first order correction, that does not take into account the scattering angle θ. In order to acknowledge the angular dependence of the screening in the Rutherford cross-section, the Anderson factor F_{A} is usually used [Andersen et al., 1980]:

$$F_{\text{A}} = \frac{\left(1 + \frac{1}{2}\frac{V_1}{E_{\text{CM}}}\right)^2}{\left(1 + \frac{V_1}{E_{\text{CM}}} + \left(\frac{V_1}{2E_{\text{CM}}\sin(\theta_{\text{CM}}/2)}\right)^2\right)^2} \tag{2.19}$$

where θ_{CM} is the angle of scattering in the center-of-mass frame and the increase in kinetic energy V_1 (keV) is given by:

$$V_1 = 0.04873 Z_1 Z_2 \left(Z_1^{2/3} + Z_2^{2/3}\right)^{1/2} \tag{2.20}$$

The angular dependence of the Anderson factor, for an interaction between an He^{2+} ion and a cooper atom ($Z_2 = 29$, $M_2 = 63.5$,), as well as the angular independent correction L'Ecuyer factor $F_{\text{L'E}}$, is shown in Figure 2.6.

As can be seen in Figure 2.6, for small angles the angular independent $F_{\text{L'E}}$ underestimates the value of the correction of the Rutherford cross-section, and the Anderson factor F_{A} should be used. However, for $\theta > 90^{\text{o}}$ both factors are quite similar and, with increasing energy, their values approach unity.

The high-energy deviation to the classical Rutherford scattering is created due to the existence of short-

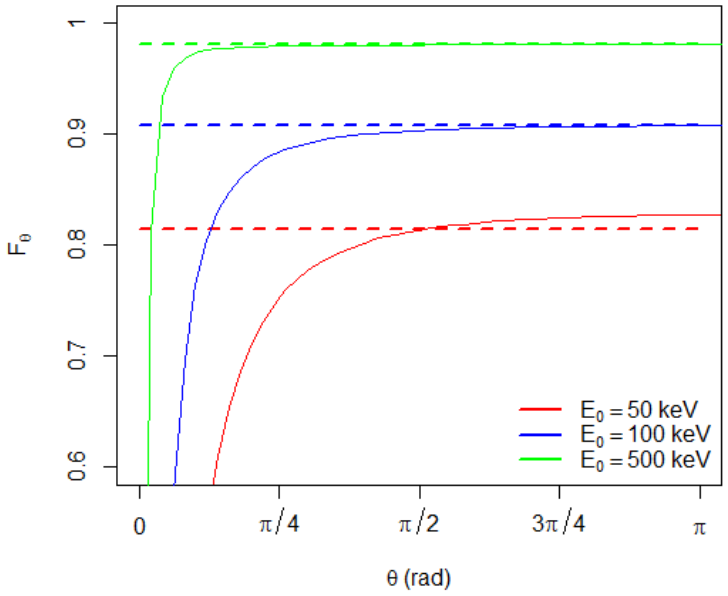

Figure 2.6: Value of the Anderson (full line) and the L'Ecuyer correction factor (dashed line) of the Rutherford differential cross-section of the interaction between a helium ion projectile ($Z_1 = 2; M_1 = 4$) and a copper atom ($Z_2 = 29; M_2 = 63.5$), with $E_0 = 50keV$ (red), $E_0 = 100keV$ (blue) and $E_0 = 500keV$ (green).

range nuclear forces. According to experimental results conducted by Bozoian [Bozoian et al., 1990][Bozoian, 1991], the energy $E_{\text{HE-D}}$, in the laboratory frame, at which the deviations from the classical Rutherford cross-section are greater than 4% is approximately given by [Bozoian, 1993]:

$$E_{\text{HE-D}} = \frac{M_1 + M_2}{M_2}\frac{Z_2}{10}, \text{ for } Z_1 = 1 \tag{2.21}$$

$$E_{\text{HE-D}} = \frac{M_1 + M_2}{M_2}\frac{Z_1 Z_2}{8}, \text{ for } Z_1 > 1 \tag{2.22}$$

The laboratory energy of departure $E_{\text{HE-D}}$, as a function of the target's atomic number Z_2, is presented in Figure 2.7, for a proton and an helium ion projectile.

For a helium ion scattering off a Carbon atom ($Z_2 = 6; M_2 = 12$), the high-energy limit is $E_{\text{CM}} = 2$ MeV, which corresponds to a beam energy of $E_0 \approx 5.3$ MeV, well above the usual beam energies of 1 to 2 MeV used in RBS analysis, a property shared by all but the lightest of elements, where the beam energy was calculated accordingly to equation 2.18. As such, the influence of the high-energy departures of the Rutherford cross-section, for common RBS analysis, will be minor.

Note, that currently there exists no general theory to calculate the high-energy departures to the Rutherford cross-section, and equations 2.21 and 2.22 are to be taken as approximations, with deviations up to 20% documented [Oberkofler et al., 2011]. As such, experimental values should regularly be used in cross-section studies,taking the necessary precautions regarding the influence of the experimental scattering angle in the value, available through several computational programs and databases, such as NRABASE [Agency, 1997], SIMNRA [Mayer, 1999] and SRIM [Ziegler et al., 2008].

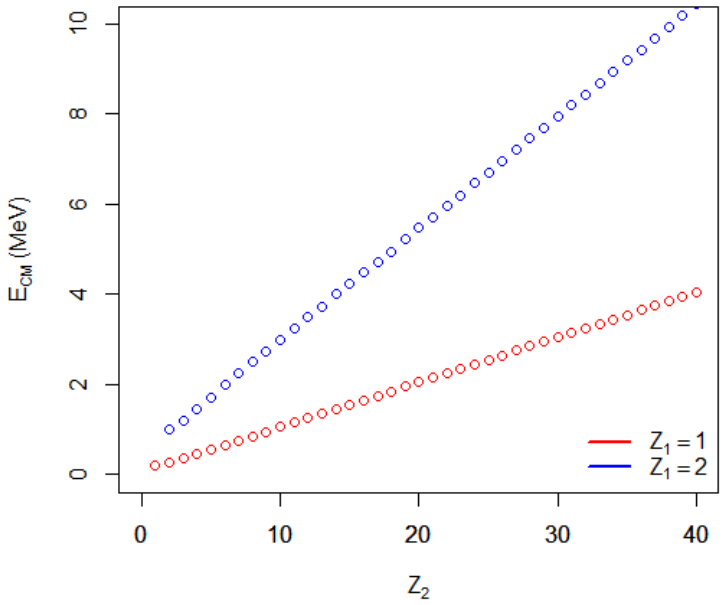

Figure 2.7: Value of the center of mass energy to which the cross-section deviates by 4% from the Rutherford value, for proton (red) and helium ion (blue) projectiles, as a function of the target's Z_2.

2.3 Ion Energy loss

In order to fully understand the potential of using light MeV ion beams to describe the elemental properties of biological samples, an incursion into the mechanisms of ion energy loss in matter is needed. When an energetic ion traverses a material, it loses energy at a rate dE/dx, usually of a couple of hundred electro-Volt per nanometre, which depends on the type of ion projectile (more precisely on M_1 and Z_1) and the elemental matrix of the sample. This rate is also known as Stopping Power. The energy loss process occurs through successive electronic collisions, in which the projectile's kinetic energy is lost through the excitation and ejection of atomic electrons, and nuclear collisions, where the energy is transferred to kinetic energy to the entire target atom, causing the ion to slow down and, finally, come to rest at some depth in the material. The relationship between these components can be expressed by:

$$\frac{dE}{dx} = \left.\frac{dE}{dx}\right|_{\mathrm{e}} + \left.\frac{dE}{dx}\right|_{\mathrm{n}} \tag{2.23}$$

where $\left.\frac{dE}{dx}\right|_{\mathrm{e}}$ refers to the electronic stopping power component and $\left.\frac{dE}{dx}\right|_{\mathrm{n}}$ to the nuclear stopping power. Electronic collisions impart small energy losses and small angle deflections to the ion projectile. On the other hand, nuclear collisions impart large, discrete, energy losses and large angle deflections to the ion projectile. In effect, while being responsible for the backscattered events detected in RBS analysis, nuclear collisions occur quite infrequently: for a copper atom, with mass number $A_{\mathrm{Cu}} = 64$, the radius of its nucleus is approximately $r_{\mathrm{Cu}} \approx 6 \times 10^{-5}$ Å, given by [Weizsäcker, 1935]:

$$r \sim r_0 A^{1/3} \tag{2.24}$$

where $r_0 = 1.25 \times 10^{-5}$ Å. Comparing this value with its lattice constant $r_{\mathrm{Cu_{lat}}} = 3.61$ Å, it is visible that

the size of a nucleus is approximately five orders of magnitude smaller than the distance between two atoms. Thus, due to the nucleus small size, electronic collisions are much more frequent than nuclear collisions. Moreover, the relative importance of these components varies rapidly with the projectile's velocity v, proportional to $\sqrt{E_0}$. The evolution of the electronic and nuclear energy loss rates with increasing E_0, for an proton projectile in a copper sample is presented in Figure 2.8.

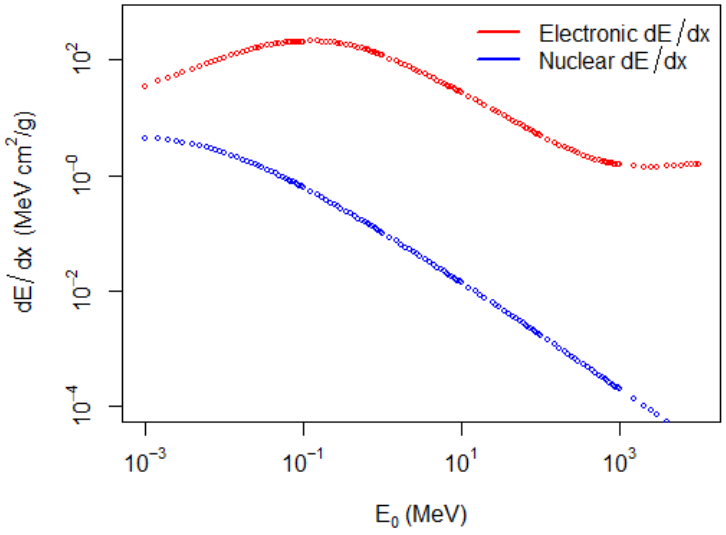

Figure 2.8: Value of the electronic (red) and nuclear (blue) energy loss rates of a proton projectile ($M_1 = 1$, $Z_1 = 1$) in copper ($M_2 = 63.5$, $Z_2 = 29$), as a function of E_0. Values taken from [Berger, 1992].

In this conditions, the electronic energy loss for a 1.5 MeV ^{1}H accounts for 99.92% of the total energy loss, in contrast with the 0.08% derived from nuclear interactions. As such, for typical ion beam applications, electronic collisions will be the mechanism responsible for most of the projectile's energy loss.

2.3.1 Electronic Energy Loss Regimes

For convenience, the process of ion energy loss due to electronic collisions if often divided into low and high-energy regimes. An estimate of the energy that separates these two regimes is given by the Bohr velocity v_0 of an electron in the innermost orbit of the hydrogen atom, $v_0 = e^2/\hbar = 2.2 \times 10^6$m/s, which corresponds to the velocity of a 25 keV ^{1}H ion or a 100 keV ^{4}He ion. As such, much of the energy loss of the projectile species in the energy range relevant to RBS analysis occurs in the high-energy regime. In the lower-energy regime ($v \approx 0.1v_0$ to $v \approx Z_1^{2/3}v_0$), the incident ion is not fully striped of its electrons, with an effective charge smaller than $Z_1 e$, and tends to neutralise its charge by electron capture. The mechanism of ion energy loss in this range was first described by Lindhard [Lindhard and Scharff, 1961] and Firsov [Firsov, 1958] and it was shown that the electronic stopping cross-section σ_e is given by:

$$\sigma_\mathrm{e} = \xi_e 8\pi \frac{Z_1 Z_2}{\left(Z_1^{2/3} + Z_2^{2/3}\right)^{3/2}} a_0 \hbar v \tag{2.25}$$

As such, in these conditions, the electronic energy loss is approximately proportional to $E_1^{1/2}$, increasing

with increasing energy until reaching its maximum rate, occurring at the ion's Fermi-Thomas velocity v_{TF}:

$$v_{\mathsf{TF}} = v_0 Z_1^{2/3} \tag{2.26}$$

This maximum occurs at about 25 keV for H^+ ions and 250 keV for He^{2+} ions. On the other hand, in the high energy regime the ion projectile is completely stripped of its electrons and behaves as a positive charge $Z_1 e$. The rate of ion electronic energy loss in this regime can be characterized in terms of close, high momentum transfer collisions with electrons, when the ion is within the electronic orbitals, and distant, low momentum transfer collisions when the ion is outside the electron shells. This behaviour is described by the Bethe formula [Bethe and Ashkin, 1953]:

$$\left.\frac{dE}{dx}\right|_{\mathsf{B\text{-}B}} = \frac{4\pi Z_1^2 e^4 n_e}{m_e v_1^2} \ln \frac{2 m_e v_1^2}{I} \tag{2.27}$$

where $I \approx 10 Z_2$ (eV) represents the average excitation energy of an electron, m_e is the electron mass and n_e is the number of electrons per unit volume. Thus, in this regime, the rate of ion electronic energy loss decreases with increasing energy, due to the decrease in probability of interaction with an atomic electron with increasing ion velocity through the orbital cloud. Also, according to equation 2.27, the electronic energy loss is proportional to Z_1^2 for the same velocity v_1. As such, a 1 MeV H^+ ion has roughly a quarter of the rate of energy loss of a 4 MeV He^{2+}, where the kinetic energy of the ion is given by $T_1 = M_1 v_1^2/2$. It is also important to note that the description presented in equation 2.27 neglects the effects of variations in electron binding and shell structure of the atoms, which can be observed experimentally in small deviations in the value of I. Corrections to the formula have been made regarding the existence of strongly-bound inner shell electrons and relativistic effects. However, equation 2.27 can still be used, as a first approximation, to estimate the value of $\left.\frac{dE}{dx}\right|_{\mathsf{e}}$, in the high energy regime.

2.3.2 Ion Range

The considerable difference in orders of magnitude between the electronic energy loss rate and the nuclear energy loss rate reveals that the mechanism responsible for the ion energy loss is the innumerous collisions with the atomic electrons, until coming to rest at a certain depth in the sample material. As such, the range of the light MeV ions is also governed by the electronic energy loss mechanism. While not being a paramount property to consider in the planning of NRA, ERDA or electron imaging analysis, since the signals used in these techniques originate close to the surface of the sample, ion range is a fundamental consideration in RBS analysis. The energy loss rate increases with increasing depth, as expected from the behaviour expressed in Figure 2.8, until reaching a maximum, near the final range of the ion. The electronic and nuclear energy loss components are discretized in Figures 2.9a and 2.9b. Note, the existence of a low baseline energy loss that extends for most of the depth achieved in the sample, before the appearance of a sudden increase in energy loss, the Bragg Peak, whose position will be a function of E_1 and Z_1. The ability to control the position of the majority of the energy loss

of incident ions is the underlying principle behind many applications of ion beams in the industry, such Proton Beam Writing (PBW) [Watt et al., 2007] and Hadron Therapy [Amaldi and Kraft, 2005], which requires a precise knowledge of the range of the projectile.

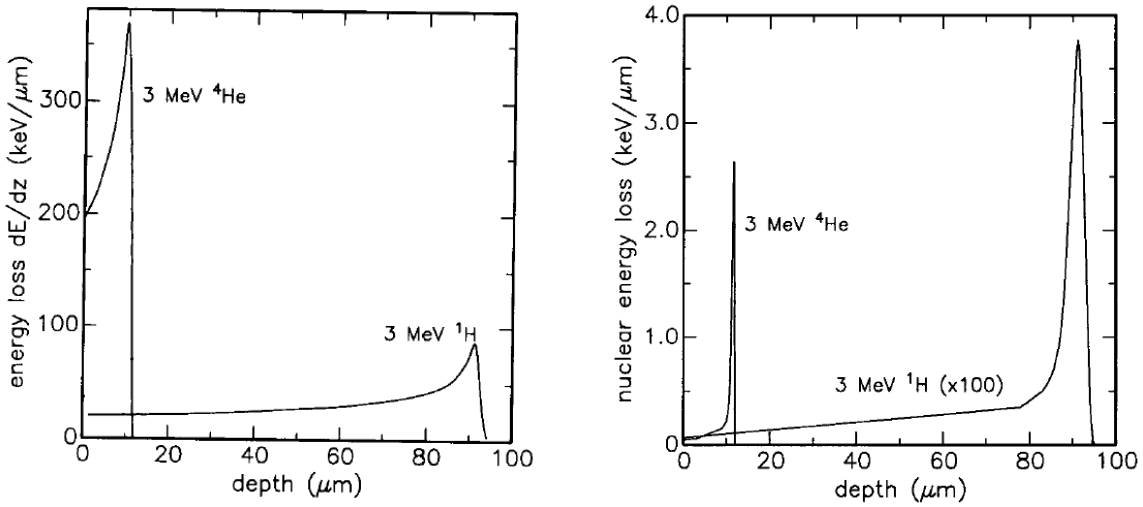

Figure 2.9: Average rate of electronic (a) and nuclear (b) energy loss, for 3 MeV proton ($M_1 = 1$, $Z_1 = 1$) and helium ($M_1 = 4$, $Z_1 = 2$) projectile, in an amorphous silicon ($M_1 = 28$, $Z_1 = 14$). Taken from [Breese et al., 1996].

The average range $\bar{R}$ of an incident ion beam in a given sample, along the beam's direction, can be evaluated as:

$$\bar{R} = \int_0^{E_1} \frac{1}{\left(\frac{dE}{dx}\right)} dE \tag{2.28}$$

As expected, and seen in Figures 2.9a and 2.9b, for the same initial energy a ^{4}He is able to penetrate the sample significantly less than a ^{1}H ion, due to its considerably larger energy loss rate. Thus, the choice of the incident species is a crucial parameter in some ion beam analysis techniques, such as STIM, which require the ion beam to completely transverse the sample in order to detect and evaluate it. As such, proton beams are usually used, due to their increased range capabilities in comparison with ^{4}He beams. Also in RBS, a previous study of the range of the ions in a given sample is fundamental to ensure that the technique is able to probe the necessary depth in the target, sometimes being needed a fine-tuning in the energy of the beam or a change in the projectile species. On the other hand, low energy ions cannot probe even sub-surface layers of a sample and, as such, are deposited in its surface. This is the principle of the ion implantation technique [Hamm and Hamm, 2012]. Equation 2.28 can only give an estimative of the range of the ion beam, due to statistical variations in the number of collisions with atomic electrons that the incident ions sustain. This variation in range of the beam is named straggling, which is discussed in depth in Appendix A.

2.4 Procedures in RBS Analysis

Having discussed the underlying principles of the interaction between light-MeV ions and the atoms of a given sample, it is now possible to understand the basic functioning of backscattering spectrometry, which has been used extensively for simultaneous determination of a target's stoichiometry and of the depth distribution of the target elements, with depth resolutions below the micrometer scale (10-100 nm) and adequate detection limits for most common samples, ranging from a few parts per million for heavy elements to a few percent for lighter elements. The application of the technique is done in an simple, quick way, with acquisition times in the order of minutes (depending on the volume of data needed), with no significant destructive effects imparted to most types of samples. The results do not require the use of any external standards, are unaffected by chemical bounding in the target and are easily understandable for the analyst. As such, RBS has become a standard procedure in micro-beam analysis worldwide. In this section, the mechanisms of RBS analysis will be discussed, particularly regarding depth profiling (Chapter 2.4.1) and sample's stoichiometry identification (Chapter 2.4.2) capabilities.

2.4.1 Depth Profiling

Undoubtedly, the most interesting capability of RBS analysis resides in its ability to probe the inner structure of a given sample, not only on a surface level but also as a function of its depth. This capability is intrinsically related to the physical principles of the interaction of ions with atoms, namely the importance of the kinematic factor, the interaction cross-section and the energy-loss process of ions in matter, presented in Chapters 2.1, 2.2 and 2.3. More precisely, it is the loss of energy by the projectile while crossing the medium, characterized by its dE/dx, that enables the extraction of depth information from the sample.

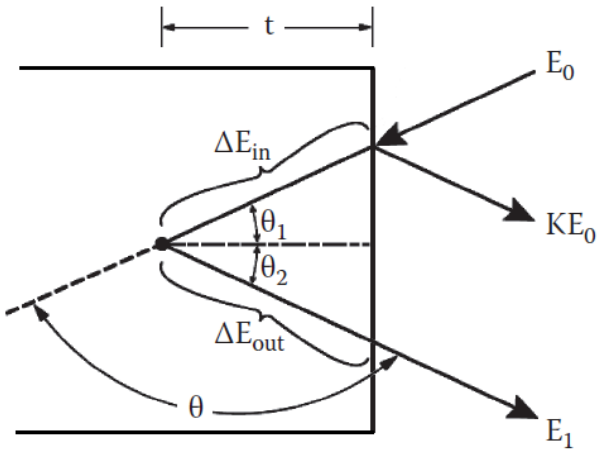

Figure 2.10: Kinematics of the the energy loss mechanism of a beam ion, until its interaction with the nucleus of an element of the sample, at a depth t. Adapted from [Wang, 2009].

The energy-loss process of ion projectiles occurs in three different stages: first, the ions continuously lose energy through interactions with the electrons of the atoms as they traverse the sample, until elastically colliding with the nucleus of a given element, losing a fraction K_{Target} of its energy, after which the

ions, once again, successively lose energy through electronic interactions, before emerging off the sample. For single-element samples, the energy difference at the detector ΔE, between an ion scattered at the sample surface and an ion scattered at a depth t, can be given by:

$$\Delta E = [E_f]t \tag{2.29}$$

where $[E_f]$ is named the energy loss factor, given by:

$$[E_f] = \left[K_{\text{Target}} \left(\frac{dE}{dx} \right)_{\text{in}} \frac{1}{\cos\theta_1} + \left(\frac{dE}{dx} \right)_{\text{out}} \frac{1}{\cos\theta_2} \right] \tag{2.30}$$

where θ_1 and θ_2 are the angles defined in Figure 2.10 and the stopping powers are those of the ion before and after the interaction with the nucleus. Usually, the results of RBS analysis are expressed in terms of areal density (atoms per unit area) and as such the energy difference ΔE can be also defined by:

$$\Delta E = N[\epsilon]t \tag{2.31}$$

where N is the atomic density (atoms/cm^3) and $[\epsilon]$ is named the stopping cross section factor, given by:

$$[\epsilon] = \left(K_{\text{Target}}\, \epsilon_{\text{in}} \frac{1}{\cos\theta_1} + \epsilon_{\text{out}} \frac{1}{\cos\theta_2} \right) \tag{2.32}$$

where ϵ is the stopping cross-section defined as:

$$\epsilon = \frac{1}{N} \frac{dE}{dx} \tag{2.33}$$

For multi-elemental samples, the question of the way to take into account the contribution of the different elements to the global energy loss mechanism arises. Indeed, as previously discussed, this mechanism consists on a sequence of random and independent interactions with atomic electrons. Thus, the stopping cross-section $\epsilon^{A_m B_n}$ of a multi-elemental sample of composition $A_m B_n$ can be determined as:

$$\epsilon^{A_m B_n} = m\epsilon^A + n\epsilon^B \tag{2.34}$$

where ϵ^A and ϵ^B are the stopping cross sections of the elements A and B. This relation is usually called Bragg's Law. The depth-energy relation for samples with multiple elements is in all quite similar to equation 2.31: for a compound sample $A_m B_n$, N becomes the molecular density N^{AB} (molecules/cm^3) and K and ϵ_{out} from each element are used in the stopping cross section factor. For element A, the depth-energy relations are given by:

$$\Delta E_A = [\epsilon_{\text{in}}^{AB}] N^{AB} t \tag{2.35}$$

$$[\epsilon]_A^{AB} = \left(K_A\, \epsilon_{\text{in}}^{AB} \frac{1}{\cos\theta_1} + \epsilon_{\text{out}}^{AB} \frac{1}{\cos\theta_2} \right) \tag{2.36}$$

with similar relations for element B. Similar to the mass resolution, given by equation 2.9, it is possible to define depth resolution δt, the minimum detectable difference in depth, related to the minimum energy

difference detectable by the experimental apparatus δE, such that:

$$\delta t = \frac{\delta E}{[\epsilon]} \tag{2.37}$$

As discussed in Chapter 2.1, common sources of energy spread include the detector resolution, straggling and the intrinsic spread in the beam energy. As such, depth resolution degrades with increasing depth, due to the contribution of energy straggling. In order to increase δt, $[\epsilon]$ can be improved by using heavier ions, increasing ϵ, or by tilting the sample, increasing θ_1 and/or θ_2 and thus increasing the path length necessary to reach a certain depth, incrementing the energy lost by the particle. Both options have disadvantages, since the former may reduce the detector's resolution and the latter may introduce energy broadening if the sample's surface is not reasonably flat.

Finally, the question of how to evaluate the stopping cross sections arises. For thin films ($t \leq 100$ nm), using commonly ion species for the beam, the relative change in the value of ϵ along the projectile trajectory is small. In other words, the relative change of the projectile energy is small, and the evaluation can be carried out using the "surface energy approximation", in which ϵ is evaluated at the energy after a elastic collision with a target nucleus at the sample surface, KE_0:

$$[\epsilon_0] = \left[K_{\text{Target}}\, \epsilon(E = E_0) \frac{1}{\cos\theta_1} + \epsilon(E = KE_0) \frac{1}{\cos\theta_2} \right] \tag{2.38}$$

However, for $t > 100$ nm, the change in ion energy along its path in the sample becomes significant, and a better approximation would be to evaluate ϵ at a mean energy $\bar{E}$, between the energy at the beginning and the end of the sample. This is named the "mean-energy approximation", given by:

$$[\bar{\epsilon}] = \left[K_{\text{Target}} \epsilon(E = \overline{E_{in}}) \frac{1}{\cos\theta_1} + \epsilon(E = \overline{E_{out}}) \frac{1}{\cos\theta_2} \right] \tag{2.39}$$

For the inward trajectory, the mean energy can be estimated as $\overline{E_{\text{in}}} = 1/2(E_t + E_0)$, where E_t is the energy at the depth t where the interaction with the target nucleus occurs. Similarly, after scattering, the mean energy for the outward track is given by $\overline{E_{\text{out}}} = 1/2(E_1 + KE_t)$. E_t can be determined through the measurement of ΔE, given by equation 2.31. However, a quick estimate of this value can be done assuming the symmetrical division of ΔE along the full path of the ion in the sample, such that:

$$\overline{E_{in}} = E_0 - \frac{1}{4}\Delta E \tag{2.40}$$

$$\overline{E_{out}} = E_1 + \frac{1}{4}\Delta E \tag{2.41}$$

2.4.2 Sample's Composition Determination

The RBS technique also enables the determination, with considerable precision, of the stoichiometry of the sample's elemental matrix. Considering a uniform beam of projectiles of normal incidence on an uniform sample's surface, the spectrum height (yield) of backscattered ions detected after interacting

with a layer of atoms of thickness Δt, uniformly distributed, is given by:

$$Y(t,\theta) = \frac{\sigma_R(E_1(t),\theta)\Omega Q N \Delta t}{\cos\theta_1 \mathsf{DTR}} \tag{2.42}$$

where $\sigma_R(E_1(t),\theta)$ is the scattering cross section at angle θ evaluated at ion energy $E_1(t)$, Ω is the detector solid angle, Q is the measured number of incident particles and DTR is the Dead Time Ratio of the experimental apparatus. Using beam energies typically in the order of few MeV, the scattering cross section can be assumed to be the Rutherford cross section, given by equation 2.11. As such, the yield of a given element will be proportional to E_1^{-2}, which is reflected in an increase in signal height deeper in the sample. For a more in-depth discussion on the deviations to the Rutherford cross section please refer to Chapter 2.2.2.

As such, previous knowledge of $\sigma_R(E_1(t),\theta)$, Ω, and determination of Q and Y during the experimental run allows the determination of the areal density of an element in a multi-elemental sample. Given a sample matrix A_mB_n, the total number of counts from element A, and element B, is A_A and A_B, respectively, given by:

$$A_A = \frac{\sigma_{R_A}(E_1(t),\theta)\Omega Q m N^{A_mB_n}\Delta t}{\cos\theta_1 \mathsf{DTR}} \tag{2.43}$$

$$A_B = \frac{\sigma_{R_B}(E_1(t),\theta)\Omega Q n N^{A_mB_n}\Delta t}{\cos\theta_1 \mathsf{DTR}} \tag{2.44}$$

Thus the ratio of the atomic densities of A and B can be determined by the ratio of the above two equations:

$$\frac{m}{n} = \frac{N_A}{N_B} = \frac{A_A}{A_B}\frac{\sigma_{R_B}(E_1(t),\theta)}{\sigma_{R_A}(E_1(t),\theta)} \tag{2.45}$$

Equation 2.45 is based on the assumption that the full peak of a particular element in the spectrum can be resolved and the ratio of peak areas can be precisely determined, which is often not possible. As such, the ratio of surface heights can be used for composition analysis. The backscattering yield at the surface H_i for elements A and B are given, respectively, by:

$$H_A = \frac{\sigma_{R_A}(E_0,\theta)\Omega Q m N^{A_mB_n}\tau_A}{\cos\theta_1 \mathsf{DTR}} \tag{2.46}$$

$$H_B = \frac{\sigma_{R_B}(E_0,\theta)\Omega Q n N^{A_mB_n}\tau_B}{\cos\theta_1 \mathsf{DTR}} \tag{2.47}$$

where τ_A and τ_B are the thickness of the layers containing elements A and B, respectively, related to the energy width of a channel, the energy resolution, of the detecting system, which at the surface is given by:

$$\delta E = \tau_A N^{A_mB_n}[\epsilon]_A^{A_mB_n} = \tau_B N^{A_mB_n}[\epsilon]_B^{A_mB_n} \tag{2.48}$$

Combining equations 2.46, 2.47 and 2.48, gives:

$$H_A = \frac{\sigma_{R_A}(E_0,\theta)\Omega Q m \delta E}{[\epsilon]_A^{A_mB_n}\cos\theta_1 \mathsf{DTR}} \tag{2.49}$$

$$H_B = \frac{\sigma_{R_B}(E_0, \theta)\Omega Q n \delta E}{[\epsilon]_B^{A_m B_n} \cos\theta_1 \mathsf{DTR}} \tag{2.50}$$

Finally, the ratio of atomic densities for elements A and B can be written as:

$$\frac{m}{n} = \frac{N_A}{N_B} = \frac{H_A \sigma_{R_B}(E_0)[\epsilon]_A^{A_m B_n}}{H_B \sigma_{R_A}(E_0)[\epsilon]_B^{A_m B_n}} \tag{2.51}$$

This approach can be easily extended for sample matrices with more than two elements. Thus, with knowledge of the underlying physical mechanisms behind Rutherford back-scattering spectrometry, the technique allows not only the determination of the composition of an unknown sample but also the extraction of depth information regarding the elemental distribution of that sample. Several examples of computational software exist that are able to analyse, with precision, a given sample using the output of the microbeam setup for the technique. Still, the visualisation of the analysis results does not take fully advantage of the depth capabilities of RBS, more precisely regarding the distribution of elements in a fully 3D-space. In order to tackle this deficiency, a new computational software is needed.

Chapter 3

The MORIA Software

The development of improved experimental devices for RBS has been closely associated with the development of new computational software that not only enables the extraction of experimental data, but also allows the efficient process of such data, making use of the unique theoretical framework of this technique, along with several others, in ion beam analysis. Still, the visualization options of RBS data are not completely explored, especially concerning the depth information capabilities of the technique. As such, in this Chapter a new computational software is presented (Chapter 3.1), along with its data handling processes (Chapter 3.2).

3.1 Overview

The MORIA (**M**icro-beam **R**bs **I**mage **A**nalyser) program is a C++ coded software, available for Windows operative systems, that enables the presentation of a model of the distribution of a given sample element, in a fully 3D environment, and the interaction with the model in real-time. MORIA combines an automated input file processing, with an user-friendly graphical interface, allowing the possibility of setting up the different aspects of the simulation, and a fast, and efficient 3D renderer.

The MORIA's GUI was designed in wxWidgets [Smart et al.], a C++ developed GUI toolkit, freely available for personal and commercial use. Its main advantage is its use of the native platform SDK and of the system provided widgets. As such, the appearance of the program is a function of the system in which the code was compiled, and compatibility between different systems is guaranteed almost automatically, with little to none code difference. The main disadvantage of this behaviour is the lack of customization on the appearance of the interface of the program, along with the possibility of the existence of platform-specific bugs, due to the code's universality. The Figure 3.1 presents the main view of the interface of the program, along with the different areas of interest.

In the Model Setup Panel, area (1) in Figure 3.1, the description of the sample, regarding thickness, elemental matrix, as well as the chosen element to be used in the model, is made through user input. It is composed of five different sub-panels, as seen in Figure 3.2, that the user can freely select: the introduction sub-panel (a), the analysis description sub-panel (b), the calibration sub-panel (c), the sample

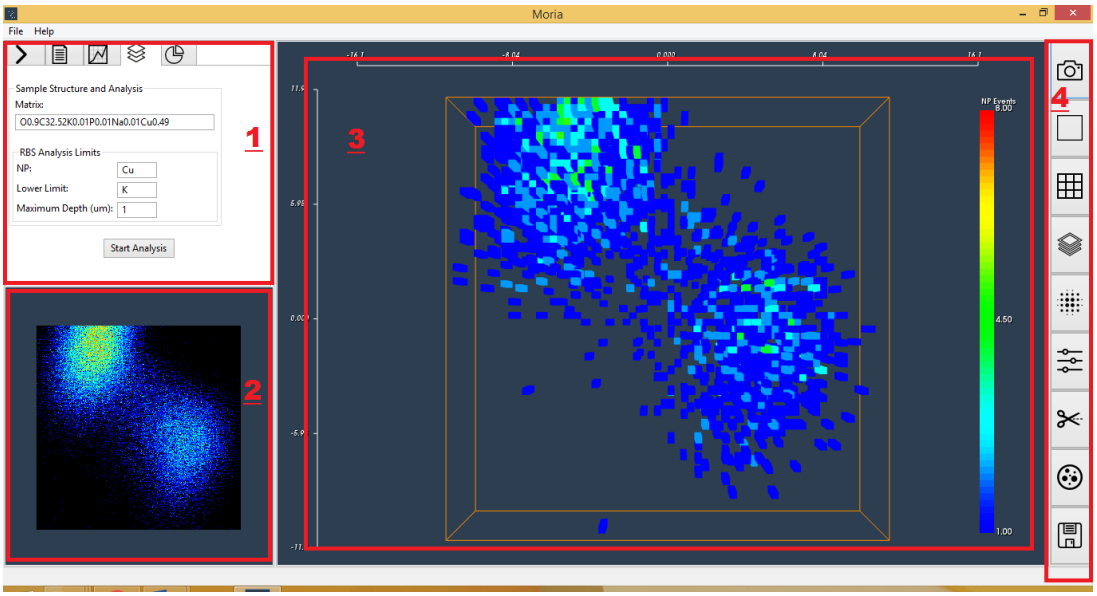

Figure 3.1: Main Interface of MORIA, with the different areas of interest: the Model Setup Panel (1), the Sample Map panel (2), the Model Visualization panel (3) and the Visualization options panel (4).

description sub-panel (d) and the model results sub-panel (d).

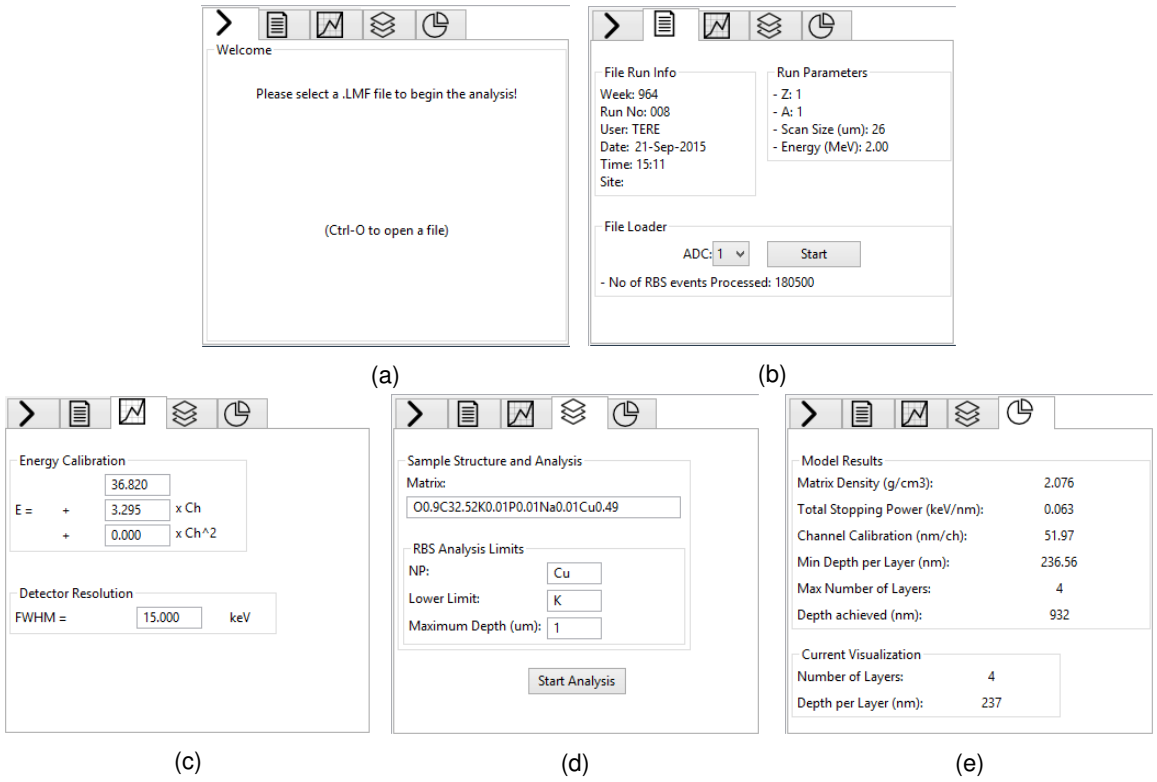

Figure 3.2: Substructure of the Model Setup Panel, composed of five different sub-panels: (a) introduction sub-panel; (b) analysis description sub-panel; (c) calibration sub-panel; (d) sample description sub-panel; (e) model results sub-panel.

The introduction sub-panel (Figure 3.2a) is the initial sub-panel presented to the user when opening the program, before the selection of the input file to be analysed. In the analysis description sub-panel (Figure 3.2b), the information regarding the experimental parameters of the input file is presented. It

is also in this sub-panel that the reading of the data in the file starts, after the selection of the ADC correspondent to the RBS detector in the microbeam setup. The calibration sub-panel (Figure 3.2c) is responsible for the presentation of the energy calibration of the ADC along with the value of energy resolution of the detector, whose values can be directly altered by the user. The sample description sub-panel (Figure 3.2d), the user inserts the sample's elemental matrix, as well as the chosen element to be mapped, the inferior energy limit of analysis and the maximum depth to be reached. Finally, in the model results sub-panel (Figure 3.2e) the description of the created 3D model is presented.

The visualization engine, used in both the Sample Map panel (2) and the Model Visualization panel (3), is provided by VTK [Schroeder et al., 2015], an open-source, cross-platform, C++ toolkit, freely available for personal and commercial use, built for 3D modelling, image processing, volume rendering, scientific visualization, and information visualization, with numerous applications in the Biophysics and Radiology field [Feng and Wang, 2012] [Dong et al., 2012]. The platform-universality of the toolkit, along with its low system requirements, are the main advantages of VTK. The implementation of VTK in the wxWidgets environment is done through wxVTK [Wxvtk.sourceforge.net, 2003], a C++ wxWidgets class which enables the rendering and interaction between the two toolkits, such that the visualization engine behaves as another usual wxWidgets component. For a more complete description of the usage of VTK in MORIA, please refer to Chapter 3.2.3. Finally, the visualization options panel includes several functions for real-time manipulation of the model, such as altering the resolution and the number of depth channels , which are presented in depth in Appendix B.

3.2 MORIA processes

In this section, the underlying structure of processes in MORIA is described in detail. The program's operation can be divided into three sequential segments: File input and reading, discussed in Chapter 3.2.1, data processing and model creation, examined in Chapter 3.2.2, and data visualization discussed in Chapter 3.2.3.

3.2.1 File Input

In this section, the procedures of the selection of the input file and the mechanisms of file reading are discussed. As stated in Chapter 1.1.3, the nuclear microprobe facility at CTN uses an Oxford Instrumentation Setup for its data acquisition system. The experimental equipment comes with an complementary analysis software, OMDAQ. OMDAQ receives information in real-time from the interface module, which contains circuitry such that up to 8 detectors, coupled to an Analogue-to-Digital converter (ADC) through a multiplexer, can be used simultaneously in the sample chamber, with real-time collection of data regarding the beam's X and Y position, energy detected and timing information, which allows multiple information extraction of the sample, through various IBA techniques.

After processing in OMDAQ, the information is stored through three different types of data files: Spectrum, Map and Listmode files. The Spectrum file (with file extension ._), contains 1-D spectrum infor-

mation for each specific ADC, stored in a block of N DWORD (32-bit unsigned integer) channel values. The Map file type (with file extension .2D), contains 2-D map information regarding specific spectrum energy ranges, selected by the user, stored in N$\times$N pixel binary values. In both cases, the information can also be compressed, using the compression scheme presented by [Zolnai and Szilgyi, 1986], in order to reduce the file size. Finally, the Listmode (LM) file type (with file extension .LMF) serves as a collection of event-by-event data, stored in N blocks of information, written by order of detection. Each block contains the ADC channel corresponding to the detector where the signal originated, the energy of the event and the beam's X and Y position for each event detected. As such, LM files can be used as a method for reproducing the analysis, serving as a global storage of the information extracted from the sample through various IBA techniques, and the ability to associate energy values with positions in the sample's 2D-plane is crucial for RBS analysis and, by extension, to MORIA.

Common to the three file categories is the existence of several header blocks at the beginning of the file, responsible for the recording of various types of experimental and formatting information. The internal composition of the header block is described in Table 3.1:

Table 3.1: Description of the components of the header block in a LM file

Structure	Size (Bytes)	Function
`IdStruct`	18	File and header version identification
`dataSTRUCT`	472	Sample and experimental conditions description
`ADCINFO`$[8]$	220	Single radiation detector description

where the suffix $[8]$ refers to the existence of 8 `ADCINFO` structures, one for each detector in the experimental setup. Events in LM files are stored in three different formats accordingly to the `lmfVersion` parameter, which can be found in the `IdStruct` component of the header block, described in Table 3.2.

Table 3.2: Formats of data storage in LM files

lmfVersion	Format			Bytes per event
0	(WORD Energy) 00AAAEEE EEEEEEEE	(BYTE X-beam) XXXXXXXX	(BYTE Y-beam) YYYYYYYY	4
1	(WORD Energy) 0AAAEEEE EEEEEEEE	(BYTE X-beam) XXXXXXXX	(BYTE Y-beam) YYYYYYYY	4
2	(WORD Energy) 0AAAEEEE EEEEEEEE	(WORD X-beam) 0000XXXX XXXXXXXX	(WORD Y-beam) 0000YYYY YYYYYYYY	6

where A is a bit in the ADC number, E is a bit in the energy and X and Y are bits in the X, and Y, position of the beam, respectively. Please note that each (E,X,Y) triplet event is preceded by unique 5 DWORDS (5×4 bytes), referring to the time of the event in the data block. If there are fewer events in the block than the maximum capacity, the end of the block is padded out with the code 0xFFFF.

In order to enable the analysis of OMDAQ files in an external application, the free OMDAQ Software Development Kit (SDK) was used, which provides functions to read and extract information from any OMDAQ file. The SDK is composed of several files, such as a dynamic link library file `DataIO.DLL` and a header file `DataIO.H`, which contains the definitions of all the OMDAQ procedures and structures. Also, a secondary library file `DataIO.LIB` had to be created from `DataIO.DLL`, which contains a list of the exported functions and data elements from the dynamic link library. This file was created using the IMPLIB software [Digitalmars.com, 2016], yet some difficulties arose due to incorrect naming of the functions in the original `.DLL` file, but a simple renaming of such functions sufficed to overcome them. Having discussed the structure of LM files and the OMDAQ SDK, it is now possible to understand the mechanism of file reading in MORIA, which is illustrated in Figure 3.3.

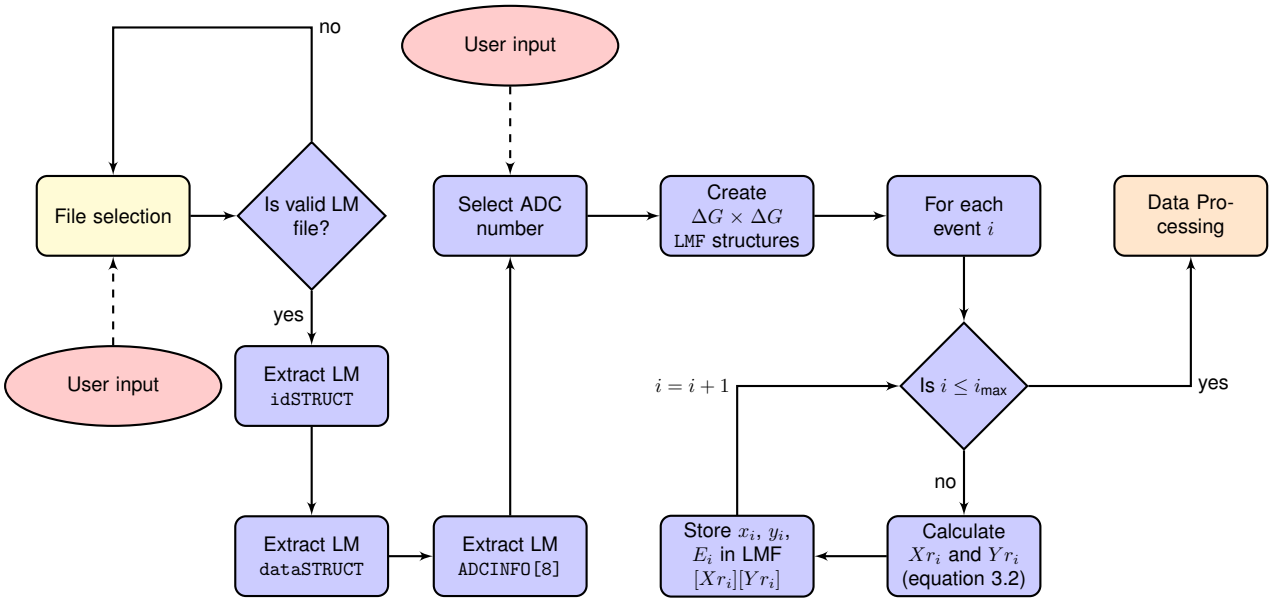

Figure 3.3: Flowchart of the file input and reading mechanism in MORIA.

The file reading mechanism in MORIA serves three consecutive goals: the identification of a valid LM file, the extraction of information regarding the experimental run from the file and the selection of RBS events accordingly to their (X,Y) coordinates. After the selection of the input file, the program verifies if the file is indeed a LM file through the function `DAQFileType()`. If the file is not an valid LM file, then the program outputs an error dialog, and the process can be reinitialised. On the other hand, if the user selected file is a valid LM file the program initiates the extraction of information from the header structures of the file, more precisely from the `idSTRUCT` `dataSTRUCT` and `ADCINFO` structures, using the functions `_QuickReadIdData()`, `_QuickReadRunData()` and `_QuickReadAdcData()`, respectively, which return boolean values. Thus, it is possible to store some of the relevant quantities for future data processing, discussed in depth in Chapter 3.2.2, directly from the LM file, such as the projectile's charge (Z_1), atomic mass (A_1) and energy (E_0), as well other experimental constrains such as the sample's scan size (ΔS), the detector angle (θ) in the laboratory system, defined in Figure 2.10, the detector

resolution (δE), and the energy calibration of the system, given by equation 3.1.

$$E_i = C_0 + C_1 \times \text{Channel}_i + C_2 \times \text{Channel}_i^2 \tag{3.1}$$

Other descriptive information, including the week and run number, username and location of the experimental operator, date and time of the run is also stored for presentation purposes. A unique subfolder, named after the file name, is also created in the Results folder, present in the MORIA's installation path, in order to organize future analysis files. As previously discussed, the LM file consists on a sequence of N blocks of events, whose arrangement is only a function of the time of detection, independently of the ADC number. As such, at this point, it becomes necessary for the user to select the ADC number correspondent to the RBS detector. After this selection, the substantive reading process of the file, regarding the event blocks, can be initiated.

Given an event i in a given event block, the process aims to simultaneously extract the event information regarding its energy (E_i) and sort the event accordingly to its position in the 2D plane, given by the coordinates of the beam at the time of the event (x_i and y_i). However, due to the usual low number of events in RBS analysis, a sorting taking into account the full range of beam positions (256×256) would result in a sub-par visualization. As such, the events are stored in an optimal grid dimension of $\Delta G = 64$, combining into a $\Delta G \times \Delta G$ vector of structures, `LMF`, whose initialization, for a given pair of reduced coordinates Xr_i and Yr_i, is given by:

```
struct LMF[Xr_i][Yr_i] {
                std::vector<int> X;
                std::vector<int> Y;
                std::vector<float> E;
                std::vector<float> T;
                std::vector<int> T_CH;
        };
```

Figure 3.4: Pseudo-code of the initialization of a single instance of the data storage structure in MORIA.

where X is the storage vector of the values of x_i, Y is the storage vector of the values of y_i and E is the storage vectors of the values of energy E_i. The reduced coordinates Xr_i and Yr_i are given by:

$$Xr_i = \left\lfloor x_i \times \frac{256}{\Delta G} \right\rfloor \ , \ Yr_i = \left\lfloor Y_i \times \frac{256}{\Delta G} \right\rfloor \tag{3.2}$$

where the floor operator $\lfloor x \rfloor$ refers to the largest integer not greater than x. By default, the energy of each event is stored as a value in a 12-bit range, i.e a value in 4096 channels. However, the calibration stored in the LM file is only valid for 1024 channels. As such, the default value of energy must also be compressed, given by:

$$Er_i = \left\lfloor \frac{E_i}{4} \right\rfloor \tag{3.3}$$

Also note that, T and T_{CH} are the storage vectors of the corresponding depth of the event in nanometres,

and in depth channels respectively, whose use and importance will be discussed in Chapter 3.2.2. Thus, the program iterates on the number of events in the event blocks, storing the values (E_i, x_i, y_i) in the corresponding `LMF` structure, such that:

for each event i **do**:

$Xr_i \leftarrow \lfloor \frac{x_i}{4} \rfloor$ **and** $Yr_i \leftarrow \lfloor \frac{Y_i}{4} \rfloor$

$Er_i \leftarrow \lfloor \frac{E_i}{4} \rfloor$

LMF $[Xr_i][Yr_i].X \leftarrow x_i$

LMF $[Xr_i][Yr_i].Y \leftarrow y_i$

LMF $[Xr_i][Yr_i].E \leftarrow Er_i$

Figure 3.5: Pseudo-code of the event sorting algorithm in MORIA.

After processing all RBS events in the file, or by manual interruption of the process by the user, the extraction of the information from the file is ended and the processing of the data can begin.

3.2.2 Data Processing

In this Chapter, the mechanism of data processing, previously extracted from the LM input file, regarding the creation of the 3D model will be discussed. As discussed in Chapter 2, the main advantage of RBS is the extraction of information from the sample concerning the depth profile of the elements in its matrix, through a careful study of the energy loss of the projectile in that matrix. Thus, the data processing mechanism encompasses five different stages: the selection of the sample and model properties, the determination of the associated stopping power and the subsequent energy/depth calibration, the sorting of the events according to their depth, the creation of the 3D channels and finally the improvement of the model through corrections. The flowchart for this procedure is presented in Figure 3.6:
After the LM file reading process is finished, it becomes necessary to describe the sample to be analysed as well as the model to be created. More precisely, the user must insert the sample's matrix (with correct stoichiometry) as well as the analysis limits, such as the element to be modelled, the element that corresponds to the lower energy limit to be analysed and the maximum depth t_{M} that the analysis should reach. The sample's elemental matrix is given as a sequence of elements k and their correspondent proportion a_k in the matrix, with:

$$\sum_{k}^{N_k} a_k = 1 \tag{3.4}$$

where N_k is the number of elements in the matrix. The user input regarding the sample matrix is stored in a bi-dimensional vector, where the name is stored as a lower-case string and the stoichiometry of each element is stored in as a double, with previous normalization of the values if equation 3.4 was not respected by the user input. The element to be modelled k_{UL} is also stored in the program and the values of its charge Z_{UL} and atomic mass A_{UL} are automatically assigned from the existent database

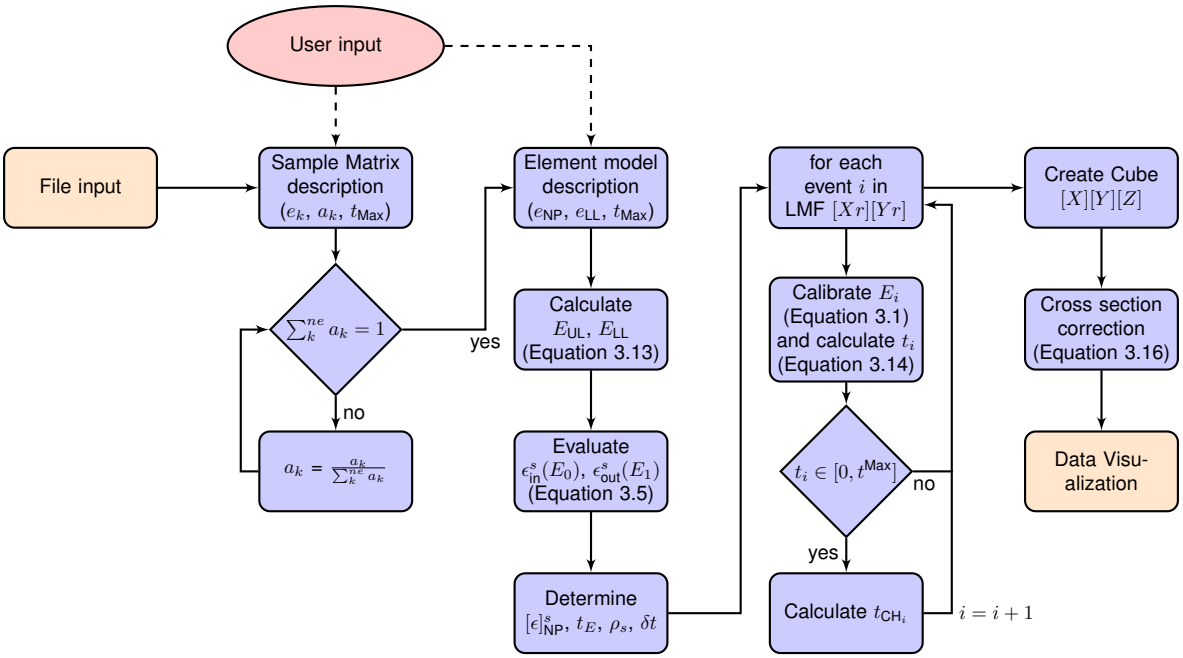

Figure 3.6: Flowchart of the data processing mechanism in MORIA.

in the program. Through the elemental matrix, the energy loss of the projectile in the sample ϵ, in the inward and outward path, can be evaluated by the pondered combination of the energy loss due to each element, in accordance to Bragg's Law (equation 2.34), taking into account its proportion in the matrix:

$$\epsilon = \sum_{k}^{N_k} a_k \epsilon^k \tag{3.5}$$

where ϵ^k refers to the the specific stopping power (keV cm^2/g) of each element. The evaluation of each ϵ^k is done using the elemental stopping-power databases from SRIM [Ziegler et al., 2008], which are available in text files in the program's installation folder. The discrete values are interpolated using a simple cubic spline interpolation function [Kluge, 2016], and ϵ^k is evaluated using the "surface-energy approximation", given in equation 2.38. Thus, the stopping power is evaluated at two different energies: at the initial beam energy E_0 and at the energy E_1 immediately after the interaction with the nucleus of k_{UL}, given by:

$$E_1 = K_{UL} E_0 \tag{3.6}$$

where the kinematic factor K_{UL} is given by equation 2.7, which is presented again here for clarity, with the necessary modifications:

$$K_{UL} = \left[\frac{[1 - (A_1/A_{UL})^2 \sin^2\theta]^{1/2} + A_1/A_{UL} \cos\theta}{1 + (A_1/A_{UL})} \right]^2 \tag{3.7}$$

Thus, two different stopping power values emerge: ϵ_{in}, evaluated at E_0, and ϵ_{out}, evaluated at E_1. Finally, the stopping cross section factor $[\epsilon]_T$ for the sample can be constructed, similar to equation 2.36:

$$[\epsilon]_T = \left(K_{UL}\, \epsilon_{in} \frac{1}{\cos\theta_1} + \epsilon_{out} \frac{1}{\cos\theta_2} \right) \tag{3.8}$$

where $\theta_1 = 0$, $\theta_2 = \theta$ for the CTN's microbeam setup, as given in Figure 2.10. From this factor, the depth-energy calibration factor t_{E} (keV/nm) can be determined, given by equation 3.9

$$t_{\mathsf{E}} = \rho \times [\epsilon]_T \tag{3.9}$$

where ρ is the matrix density, given by the pondered sum of the densities of elements k, such that:

$$\rho = \sum_{k}^{N_k} a_k \times \rho_k \tag{3.10}$$

From this factor, a correspondent depth-channel calibration factor t_{CH} can also be constructed, taking into account the energy calibration of the system, given in equation 3.1, such that:

$$t_{\mathsf{CH}} = \frac{C_1}{t_{\mathsf{E}}} \tag{3.11}$$

Another important experimental variable to consider is the depth resolution δt obtainable by the experimental setup. Indeed, using the calibration factor t_{E}, it is possible to obtain a direct correspondence between the depth resolution and the energy resolution of the detector, given by:

$$\delta t = \frac{\delta E}{t_{\mathsf{E}}} \tag{3.12}$$

Thus, the minimum number of depth channels available to the analysis is limited by the energy loss of the projectile in the sample. The values of the calibration factors, along with the density of the sample and the depth resolution, can be observed in the model results sub-panel, visible in Figure 3.2e.

With the value of the depth calibration factor determined, the sorting of the events stored in `LMF` can be initiated. Since the analysis is only for a user-selected element, the program determines the upper E_{UL} and lower E_{LL} energy limits for the event sorting, through the surface energy of k_{UL} and the surface energy of the element chosen by the user to be the lower energy limit k_{LL}, given by:

$$E_{\mathsf{UL}} = K_{\mathsf{UL}} E_0 \ , \ E_{\mathsf{LL}} = K_{\mathsf{LL}} E_0 \tag{3.13}$$

where K_{LL} refers to the kinematic factor for the element k_{LL}. Thus, the absolute depth t_i of each event i, stored in the bi-dimensional structure $\texttt{LMF}[Xr][Yr].T$, is determined by:

$$t_i = |E_i - E_{\mathsf{UL}}| \times t_{\mathsf{E}} \tag{3.14}$$

As such it becomes necessary to previous calibrate the energy events stored in $\texttt{LMF}[Xr][Yr].E$, using the energy calibration defined in 3.1. Afterwards, if the energy of the event is within the limits of analysis given in equation 3.13, and, if the depth is lower than t_{M} , the event is stored in the vector T. Due to the existence of a non-null depth resolution δt, the event is also sorted into depth channels t_{CH_i}, of width Δt equal to the depth resolution by default ($\Delta t = \delta t$), which will form the basis of the visualization

procedure, discussed in Chapter 3.2.3. Thus:

$$t_{\mathrm{CH}_i} = \left\lfloor \frac{t_i}{\Delta t} \right\rfloor \tag{3.15}$$

and the value is stored in the vector T_{CH}. Iterating over all events in a given $\mathtt{LMF}[Xr][Yr]$, and iterating over the range of possible values of Xr and Yr, the depth sorting mechanism is finished. The pseudo-code of this mechanism is presented in Figure 3.7.

```
for Xr, Yr ∈ [0, ΔG[
  for each event i
  calibrate LMF [Xr][Yr].E(i)
    if  LMF [Xr][Yr].E(i) ∈ [E_LL, E_UL]
      calculate t_i ← |E(i) − E_UL| × t_E
      if t_i ≤ t_M:
        t_CH_i ← ⌊t_i / Δt⌋
        LMF [Xr][Yr].T ← t_i
        LMF [Xr][Yr].T_CH ← t_CH_i
```

Figure 3.7: Pseudo-code of the depth sorting algorithm in MORIA.

Through this mechanism, the values of the maximum achievable depth t^{Max} and the maximum depth channel constructed $t_{\mathrm{CH}}^{\mathrm{Max}}$, which obviously also corresponds to the number of channels created $N_{\mathrm{CH}} = t_{\mathrm{CH}}^{\mathrm{Max}}$, are also determined and presented in the model results sub-panel, visible in Figure 3.2e.

After the depth sorting, the $\Delta G \times \Delta G$ $\mathtt{LMF}$ structure holds all the information about the sample needed to construct the model and will be the basis for any subsequent analysis. Thus, a more manageable 3D vector $\mathtt{Cube}[X][Y][Z]$ can be created from the $\mathtt{LMF}$ structure, with $X = Xr$, $Y = Yr$ and $Z \in [0, t_{\mathrm{CH}}^{\mathrm{Max}}]$, which contains only the number of events at a given position in the X-Y-Z plane. The creation of the 3D vector can be accomplished using the pseudo-code given in Figure 3.8.

This algorithm also allows the determination of the maximum number of events ($n_{\mathrm{ev}}^{\mathrm{Max}}$) that exist in a single entry, from all the units in the complete $\mathtt{Cube}$ 3D-vector. Finally, to have a better correspondence between the number of events in each depth channel of $\mathtt{Cube}$ and the concentration of k_{UL} atoms in the sample, the values of $\mathtt{Cube}[X][Y][Z]$ must be corrected to take into account the effect of the variable Rutherford cross-section. As discussed in Chapter 2.2, the Rutherford cross-section increases significantly with decreasing projectile energies and, as such, the number of events for lower depth channels may be overestimated. However, as discussed in Chapter 2.2.2, a simple multiplicative factor of the ratios of cross-sections at a given depth, in comparison with the cross section at the sample's surface, would not suffice since for lower energies the value of cross-section deviates considerably from

```
for Xr , Yr ∈ [0, ΔG[
  for each event i with associated depth channel t_CH_i
        for Z_CH ∈ [0, t_CH^Max]
              if LMF [Xr][Yr] . T_CH(i) = Z
                ++Cube[Xr][Yr][Z]
```

Figure 3.8: Pseudo-code of the Cube 3D vector creation in MORIA.

the Rutherford formula. As such, the introduction of the L'Eculyer correction factor $F_{\text{L'E}}$, given by equation 2.17, is required. The choice of this factor over the Anderson factor F_{A} is due to the fact that in the limit of large angles, as is the case for RBS analysis, the Anderson factor tends to the L'Eculyer factor, which is significantly simpler. Hence, the number of events in each depth channel of `Cube` are corrected accordingly to:

$$\texttt{Cube}[X][Y][Z] = \frac{F_{\text{L'E}}^{E=E_0}\sigma_R^{t=0}}{F_{\text{L'E}}^{E=\Delta E_i}\sigma_R^{t=\delta t\times Z}} \times \texttt{Cube}[X][Y][Z] \tag{3.16}$$

where $\sigma_R^{t=0}$, $\sigma_R^{t=\delta t\times Z}$ are calculated using equation 2.11 and $F_{\text{L'E}}^{E=E_0}$, $F_{\text{L'E}}^{E=\Delta E_i}$ are calculated using equation 2.17, respectively evaluated at energy E_0 and ΔE_i, which takes into account the energy loss of the projectile up to the interaction depth, i.e.:

$$\Delta E_i = E_0 - t_i \times t_E; \tag{3.17}$$

The pseudo-code responsible for the implementation of the cross-section correction is presented in Figure 3.9.

```
calculate σ_{t=0} = F_L'E^{E=E_0} × σ_R^{t=0}
for Xr , Yr ∈ [0, ΔG[ and for Z ∈ [0, t_CH^Max]
   calculate σ_{t=δt×Z} = F_L'E^{E=ΔE_i} σ_R^{t=δt×Z}
   Cube[Xr][Yr][Z] = ⌊ Cube[Xr][Yr][Z] × σ_{t=0} / σ_{t=δt×Z} ⌋ ;
```

Figure 3.9: Pseudo-code of the Cube 3D cross-section correction in MORIA.

With this correction, the processing of the input data is complete and the visualization of the model in a 3D space can be done.

3.2.3 Data Visualization

As presented in Chapter 3.1, the rendering engine VTK is responsible for the display of the 3D model created in the previous Chapter. In order to understand this rendering it is necessary a previous understand the purpose of VTK and the basic functioning of the engine, before the discussion of the implementation of VTK in MORIA.

Generally, the role of VTK, or any visualization system, is to take scientific data and ultimately transform them into forms comprehensible by the human sensory apparatus, such as images. With that goal in mind, VTK provides the ability to create data flow pipelines that are capable of ingesting, processing, representing and rendering data. Thus, the central structure of VTK is a pipeline of data, from a source of information to an image rendered on the screen, consisting of three basic classes of objects, with several different subclasses: `vtkDataObject`, which concern objects to represent data, `vtkAlgorithm`, which involve objects capable of processing, transforming, filtering or mapping data objects from one form into another, and `vtkExecutive`, which are responsible for the actual execution and rendering of the data. A typical VTK pipeline is presented in Figure 3.10.

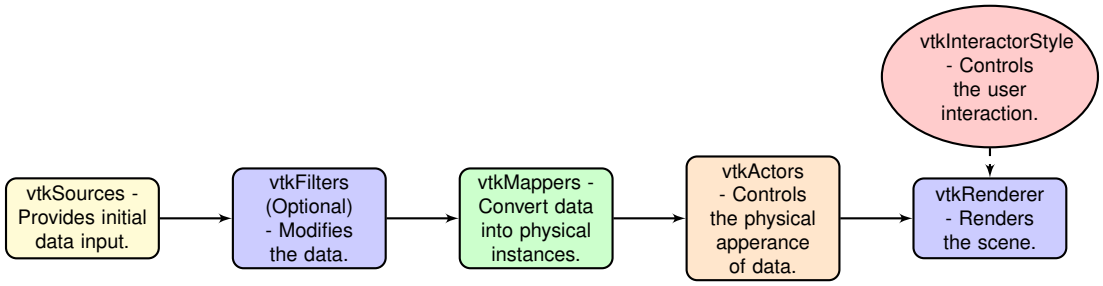

Figure 3.10: Usual pipeline of VTK rendering procedure.

A `vtkDataObject` can be considered simply the source of the data that flows through the pipeline. There exists two different classes of Data Objects: Readers and Independent Sources. Reader objects are data objects capable of reading data from external files, given the input filename and some parameters to characterize the data. Due to the versitility of VTK, there exists about 20 to 30 readers available in the library, used accordingly with the programmer's necessities, from readers capable to extract information from image files to others capable of analysing any type of structured numeric data. More importantly for the MORIA program is the existence of independent source objects, which are capable of generating data independently, given input parameters from the user, in several forms: geometrical objects, math functions, generating points, textures, movies, 3-D text, amongst others. These parameters can be used to personalise the default independent source objects, such as a sphere's radius or the edge length of a cube, in order to represent some variable.

`vtkAlgorithm` components are responsible for receiving data from other objects. There exists two different classes of `vtkAlgorithm` objects accordingly to their purpose: `vtkFilter` and `vtkMapper`. `vtkFilter` objects receive data from other components and are able to modify it, before delivering it as an output to be used by other components. Once again, there exists a myriad of different filters to be used accordingly to the needs of the programmer, such as extracting some portion of a large data set,

sub-sampling data sets to decrease resolution, interpolate data sets to a increase resolution, merge multiple inputs into a combined output, amongst others. While being an optional component of the pipeline, vtkFilters are often used for the processing of raw vtkDataObject, and the use of multiple objects of this group is quite frequent. On the other hand, vtkMapper objects are essential in any VTK pipeline, due to their purpose of mapping the data to any category of physical instance, ready to be rendered by the rendering engine. Conceptually, vtkMapper components are responsible for the bridge between the data processing component of VTK, composed of the vtkDataObject and vtkFilter objects, and the rendering component, composed of the vtkExecutive objects.

The vtkExecutive category is composed of several different classes, corresponding to the components that make up a 3D scene, such as the vtkActor, vtkRenderer, vtkRenderWindow and vtkCamera object classes. The vtkActor object classes allows the adjustment and control of the appearance properties of the physical manifestations of the data, presented in the screen. These properties include opacity, glow, color mapping, amongst others. The class vtkRenderer and vtkRenderWindow objects represent the end point of the pipeline. While there may exist several paralell pipelines resulting in various actors, usually there exists only one vtkRenderer, responsible for the simultaneous rendering of multiple vtkActors, in a single rendering window, controlled through a vtkRenderWindow object. Other auxiliary classes, such as the vtkCamera class which can change the default viewport of the rendering space, can also be used to further personalize the rendering component of VTK.

Finally, it is also important to mention the event handling capabilities of VTK, since interaction with data is a fundamental aspect of any visualization goal. At the most basic level, the interaction can be thought as the existence of a VTK widget in a rendering scene, consisting of a vtkProp subclass, such as a vtkActor object, and a subclass of vtkInteractorObserver, which will be responsible for observing user interaction in the render window (i.e., mouse and keyboard events) and processing it. An important subclass of vtkInteractorObserver is vtkInteractorStyle which is responsible for the implementation of the the majority of motion control routines, enabling even the creation of user custom routines. This subclass is fundamental since it defines the event driven interface to support vtkRenderWindowInteractor, which will be of the uttermost importance for the coexistence of VTK in wxWidgets.

Having discussed the general functioning of a common VTK pipeline, it is now possible to discuss the implementation of VTK in MORIA. As presented in Figure 3.1, there exists two different panels that resort to the VTK rendering engine: the Sample Map panel (2) and the Model Visualization panel (3). Common to them is the non-existence of a specific vtkRenderWindow initialization, which would create an isolated VTK window. Thus, for each panel the rendering area is enabled through a virtual window, created by an instance of the wxVTKRenderWindowInteractor object, a subclass object of wxVTK, which permits the embedding of the window in a wxWidgets panel. In the Sample Map panel, the rendering window contains two different renderers vtkRendererMapLoaderBG, for a background layer, and vtkRendererMapLoaderLine, for the identification of the surface-2D position of a given channel which will be further discussed in Chapter B.0.3.5. The Sample Map panel pipeline, regarding the vtkRendererMapLoaderBG renderer, is presented in Figure 3.11.

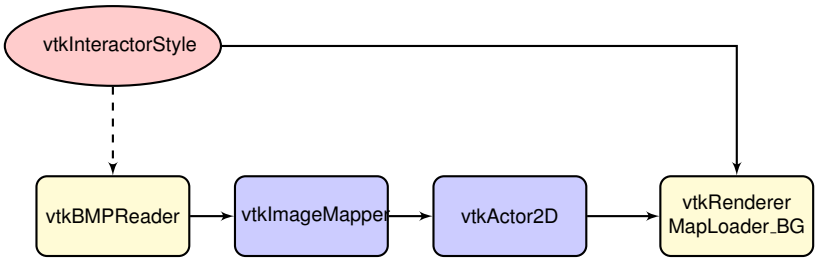

Figure 3.11: Flowchart of the vtkRendererMapLoaderBG pipeline.

The goal of the `vtkRendererMapLoaderBG` renderer is to present a user selected map file of the sample to be analysed, which can be created in OMDAQ, in order to serve as a comparison object to the model presented in the Visualization panel. Thus, the data source `vtkDataObject` to be used must be an image reader `vtkBMPReader`, which is able to reads Windows BMP files such as the MAP files created in OMDAQ. At the start of the program, the selected image to be read is the MORIA logo, available in the ”graphics” sub-folder of the installation folder. Due to the simplicity of the output, with no analysis to the image necessary, of the `vtkAlgorithm` category, it is only needed an instance `vtkImageMapper` which provides 2D image display support. The image data is mapped unto an instance of `vtkActor2D`, which is rendered in the `vtkRendererMapLoaderBG` object. On this panel, a custom `vtkInteractorStyle` was also created, in order to enable the selection of a MAP file by using the left mouse button on the panel. After the selection of the file, the logo `vtkActor2D` is removed from the renderer and new instances of `vtkBMPReader`, `vtkImageMapper` are created, with a new instance of `vtkActor2D` being added to the renderer. To update the renderer with the new actor, the renderer member function `Render()` is called. This procedure can be repeated for any number of MAP files.

The Model panel is responsible for the actual visualization aspect of MORIA, presenting the elemental model and enabling the user interaction with it in real-time. Once again, the rendering space, named `VTK_RenderWindow` , defined by the `wxVTKRenderWindowInteractor` object named `VTK_RenderWinInt`, is occupied by two non-simultaneously active renderers: `VTK3D_Renderer`, responsible for the 3D rendering of the model, and `VTK2D_Renderer`, responsible for the rendering of the model in 2D layers.

3.2.3.1 3D Rendering

The pipeline for `VTK3D_Renderer` is presented in Figure 3.12.

The model of a given element in MORIA is composed of a 3D vector of `vtkCubeSource` source data objects in number equal to the number of non-null entries in $\texttt{Cube}[X][Y][Z]$. Thus, $\texttt{Cube}[X][Y][Z]$ entries with no events are not represented in the model. In order to correctly represent the sample, the X_{Cube} and Y_{Cube} coordinates (surface plane) of each `vtkCubeSource` object are to be taken accordingly with the scan size of the experimental run, such that:

$$X_{\text{Cube}} = Y_{\text{Cube}} = \frac{\Delta S}{\Delta G} \tag{3.18}$$

However, since ΔS is usually in the order of tens of micrometers, and the maximum depth obtainable

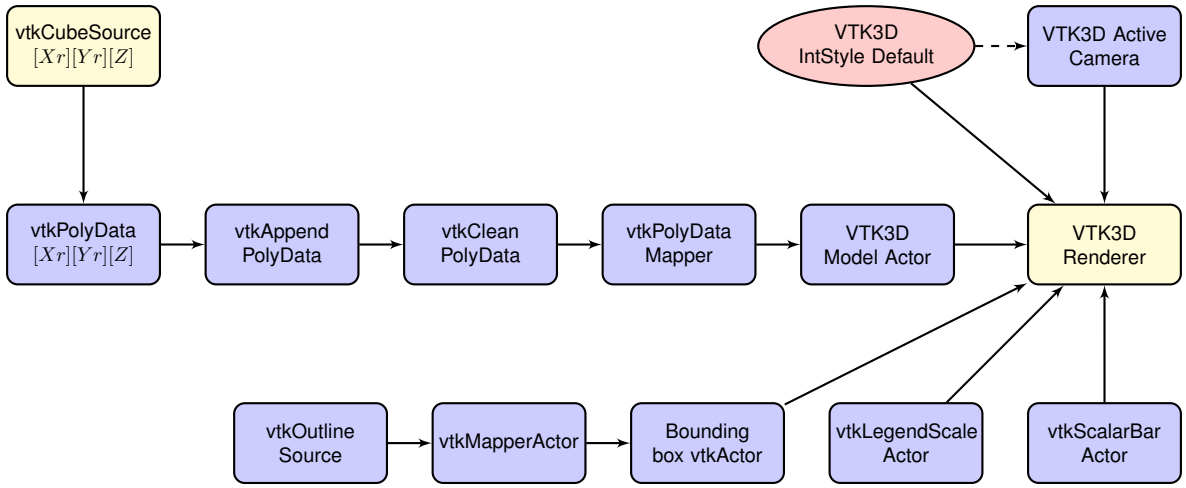

Figure 3.12: Flowchart of the VTK3D Renderer pipeline.

is usually on the order of one micrometer, for common RBS beam energies, using the correct depth value for the Z_{Cube} dimension, which is given by default by the depth resolution δt, would result in a sub-optimal visualization. Thus, for this dimension a multiplicative factor of 10 is applied to correct this problem, such that:

$$Z_{\text{Cube}} = \delta t \times 10; \tag{3.19}$$

Still, the problem of representing the information regarding the number of events in each entry of $\texttt{Cube}[X][Y][Z_{CH}]$ remains. In order to tackle this problem, a rainbow color mapping function was used, which maps the number of events to the color of the cube. However, the `vtkCubeSource` objects does not contain any color parameter. So, each `vtkCubeSource` source object is mapped unto a `vtkPolyData` object, hereby named *unit*, which presents a geometric structure consisting of vertices, lines, polygons, and/or triangle strips and, more importantly, is able to attribute scalar values to its points and surfaces. Hence, given an entry in the 3D-vector $\texttt{Cube}[X][Y][Z]$, with n_{ev} events, the [R,G,B] code of the associated $\texttt{vtkPolyData}[X_{\text{Cube}}][Y_{\text{Cube}}][Z_{\text{Cube}}]$ surfaces is given by the pseudo-code in Figure 3.13, adapted from [Telea, 2014].

for $Xr\,,\ Yr\ \in [0, \Delta G[$ **and** $Z \in [0, t_{\text{CH}}^{\text{Max}}]$

map $n_i' = \text{Cube}[X][Y][Z] \in [1, n_{\text{ev}}^{\text{Max}}] \rightarrow [0, 1]$

calculate $\delta = 4.4 \times n_i' - n_i'$

[R] $=$ max $(0, (3 - |\delta - 4| - |\delta - 5|)/2)$;

[G] $=$ max $(0, (4 - |\delta - 2| - |\delta - 4|)/2)$;

[B] $=$ max $(0, (3 - |\delta - 1| - |\delta - 2|)/2)$;

Figure 3.13: Pseudo-code of rainbow color mapping function.

The rainbow color mapping function is already implemented in the subclass `vtkLookupTable` which

maps scalar values, in this case the number of events n_{ev} stored in each entry of the 3D-vector `Cube` $[X][Y][Z_{CH}]$, into RGB color specification, and can be used to color all the surfaces in each `vtkPolyData` object.

Taking the example of a typical analysis, with $\Delta G = 64$ and $t_{\text{CH}}^{\text{Max}} \approx 10$, it would require the simultaneous initialization and rendering of over 40960 separate `vtkPolyData` models, each with physical properties and the ability be interacted with. This problem would be exponentially aggravated for higher resolution models, rendering the visualization module incompatible with a common computational setup. In order to resolve this situation a `vtkAppendPolyData` filter was used, which is able to append one of more polygonal datasets into a single polygonal dataset, thus associating the full set of `vtkPolyData` *units* into a single `vtkPolyData` model, at the cost of losing the ability to interact individually with each *unit*. However, computational times for rendering the single model are greatly decreased when compared with the time required to render the multiple individual models. The technique used to overcome the lack of interaction with the individual *units* will be further discussed in Chapter B.0.3.5. In order to remove duplicate points and degenerate cells in the `vtkAppendPolyData` output model, resulting from the attachment of the individual cells, a `vtkCleanPolyData` filter was subsequently used in the visualization pipeline. Afterwards, the program uses the standard chain of objects for the visualization, consisting of a `vtkPolyDataMapper`, a subclass object of `vtkMapper`, and a `vtkActor` object, named `VTK3D_Model_Actor`, which is added to `VTK3D_Renderer`.

Two virtual `vtkCamera` objects are also added to the renderer: a real-time camera `VTK3D_Active_Camera`, whose position can be modified by the user in real-time through keyboard and mouse commands, and a stationary camera `VTK3D_Default_Camera`, which is responsible for storing the default position of the camera, useful for resetting the visualization through the *Reset* function, further discussed in Chapter B.0.3.1. A `vtkCamera` object can be defined by its coordinates, which gives its position in a 3D space, and its focal point, which indicates the direction where the camera is aimed at. The camera's default coordinates X_{Camera}, Y_{Camera} and Z_{Camera} are given by:

$$X_{\text{Camera}} = Y_{\text{Camera}} = \Delta S/2 \quad , \quad Z_{\text{Camera}} = -2 \times \Delta S - \Delta S/3 \tag{3.20}$$

In order to obtain a centred vertical view of the sample, the camera's focal point is given by the correspondent coordinates X_{FP}, Y_{FP} and Z_{FP}, such that:

$$X_{\text{FP}} = Y_{\text{FP}} = \Delta S/2 \quad , \quad Z_{\text{FP}} = 0 \tag{3.21}$$

Additionally, a few accessory objects, concerning the sample model, were also added to the renderer: a `vtkScalarBarActor`, which presents in a vertical bar the range of values of n_{ev} along with the correspondent color in the model, a `vtkLegendScaleActor`, which presents the scale of the model, and a `vtkOutlineSource` which, after mapping to a `vtkActor` using a `vtkMapper`, provides a box with the bounding edges of the model. Finally, all the elements present in the `VTK3D_Renderer` object are presented in the Sample Visualization panel, through the calling of the renderer member function `Render()`. The interaction with the model is customized through `vtk3D_IntStyle_Default`, a cus-

tom `vtkInteractorStyle` object, which enables the rotational and translational movement of the model through mouse and keyboard events as a Trackball.

While it is possible to translate and rotate the model in real-time, further analysing functions were created in order to facilitate the analysis and extract information from the sample, which will be discussed in Appendix B.

3.2.3.2 2D Rendering

In the 2D space, the model represents the sample's elemental distribution at a given depth, by default taken to be at the surface level. The pipeline for `VTK2D_Renderer` is presented in Figure 3.14.

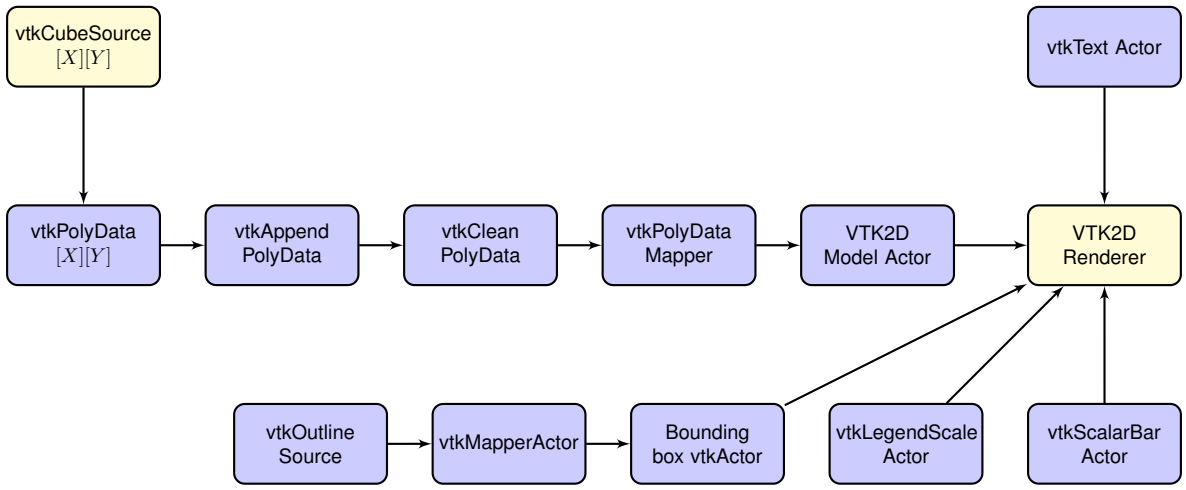

Figure 3.14: Flowchart of the VTK2D Renderer pipeline.

The process of rendering the model in 2D layers is quite similar to its 3D counterpart in regards to the visualization chain. The layer is composed of a 2D vector of $\Delta G \times \Delta G$ `vtkCubeSource` source data objects, whose dimensions are given by equation 3.18 and 3.19. Please note that the Z_{Cube} dimension is arbitrary in this case since, as will be discussed further ahead, the 2D rendering mode does not allow the movement of the model and the camera is fixed. The information regarding the number of events in each cube is once more presented through a rainbow color scheme, and thus each source object is mapped unto a `vtkPolyData` object, which is able to associate scalar values to its structure, which are subsequently translated into color values through the same `vtkLookupTable` used in 3D rendering. This mapping is made only for a specific Z depth channel, by default $Z = 0$. Thus, the model is able to represent only one layer of the sample.

Once again, in order to reduce computational times, the multiple `vtkPolyData` objects are appended into a single `vtkPolyData` using the `vtkAppendPolyData` filter. From this point on, the pipeline is identical to the 3D rendering one: the `vtkAppendPolyData` output model is mapped, through a `vtkPolyDataMapper`, into a `vtkActor`, named `VTK2D_Model_Actor`, which is added to the `VTK2D_Renderer`. Once more, the elemental model is complemented with several accessory objects, such as a `vtkScalarBarActor`, a `vtkLegendScaleActor` and a bounding box of the model. Additionally, the value of the depth corresponding to that layer is also presented on screen, through the use of a `vtkTextActor`. Since the default

position and focus point of the default `vtkCamera` allows for the desired overhead view of the sample, no custom `vtkCamera` object was created. Also, by default the `wxVTKRenderWindowInteractor` rendering space does not allow interaction with the model and, as such, no `vtkInteractorStyle` object was created. This mode of visualization is not activated by default, since the rendering space is occupied by the `VTK3D_Renderer` object, but can be obtain through the use of the *3D/2D* alternating function, discussed in Appendix B.0.3.2.

Chapter 4

Applications of MORIA to Biological Samples

As presented in Chapter 1, ion beam analysis is undoubtedly one of the most complete solutions in the Material and Biological analysis field, due to its versatility and the precision of its results. Indeed, RBS in particular offers the simultaneous possibility to not only identify the sample's unknown matrix, but also the retrieval of information regarding the distribution of those matrix elements as a function of its depth. While the applications of RBS analysis to the identification of unknown biological matrices are well known, several of which are presented in Chapter 1, in this Chapter three different applications of MORIA are presented, regarding the creation of 3D models of the depth distribution of nanoparticles in biological samples: Cu oxide nanoparticles in *Saccharomyces cerevisiae* (Chapter 4.1), Cu oxide nanoparticles in *Nematodes* (Chapter 4.2) and Au nanoparticles in *HeLa* cells (Chapter 4.3).

4.1 *Saccharomyces cerevisiae*

Saccharomyces cerevisiae remain one of the most studied and modelled organisms in Biological research and, as such, are a suitable candidate for nanoparticle toxicity studies, due to their short generation time, which allows their swift production. In this section, the analysis of samples of this organism contaminated with cooper oxide nanoparticles (CuO-NP), using both ^{1}H and ^{4}He ion beams, are presented. The nominal size of the nanoparticles used was under 20 nm.

4.1.1 Description

The *Saccharomyces cerevisiae* is an *eukaryotic* microbe belonging to the *Fungi* kingdom and the *Ascomycota* phylum. Isolated in 1938 by Emil Mrak [Mortimer and Johnston, 1986], the organism is well known for its critical role in fermentation processes, such as the processes of fermentation of sugar into alcohol, and as a leavening agent in the baking process.
Since its isolation, *S. cerevisiae* has been considered a "model organism" for biological research, due to

simultaneous being an unicellular and eukaryotic organism, along with its fast growth rate, taking only 100 minutes to double a yeast population [Herskowitz, 1988]. *Saccharomyces cerevisiae* exists in two different forms [Landry et al., 2006]: a more common diploid form, ellipsoid-shaped with a diameter of $5-15\,\mu$m and a width of approximately $1\,\mu$m, or a haploid form, spherical with a diameter of $4\,\mu$m [Sherman, 2002].

As an eukaryotic organism, *S. cerevisiae* contains several membrane-bound organelles, such as a nucleus, which contains its chromosomes, and mitochondria, responsible for the cellular respiration process. Recent studies have shown that the volume of the nucleus increases with the *S. cerevisiae* growth, on average being $7\,\%$ of the cell's volume [Jorgensen et al., 2007]. Another essential constituent of *S. cerevisiae* is the cellular wall, which is responsible for providing the shape of the organism while providing physical protection and osmotic support [Klis et al., 2002]. This structure is composed manly by mannoproteins $(35-40\%)$, β-Glucans $(60-65\%)$ and chitin $(<<1\%)$, and has a width of about $0.1-0.2\mu$m [Klis et al., 2014].

4.1.2 Sample description and analysis results

For the analysis, two different samples of *Saccharomyces cerevisiae* (SC_1) and (SC_2), exposed to 40 mg/L of concentration of CuO-NP, were analysed using the microbeam facility available at CTN. SC_1 refers to a $26\times26\,\mu m^2$ scan of the first sample, containing two different diploid-strained *S. cerevisiae* organisms, analysed using a ^{1}H beam, whose results are discussed in Chapter 4.1.2.1. SC_2 refers to a $26\times26\,\mu m^2$ scan of the second sample, containing a single diploid-strained *S. cerevisiae* organism, analysed using a helium ion beam, whose results are presented in Chapter 4.1.2.2.

4.1.2.1 SC_1 Sample

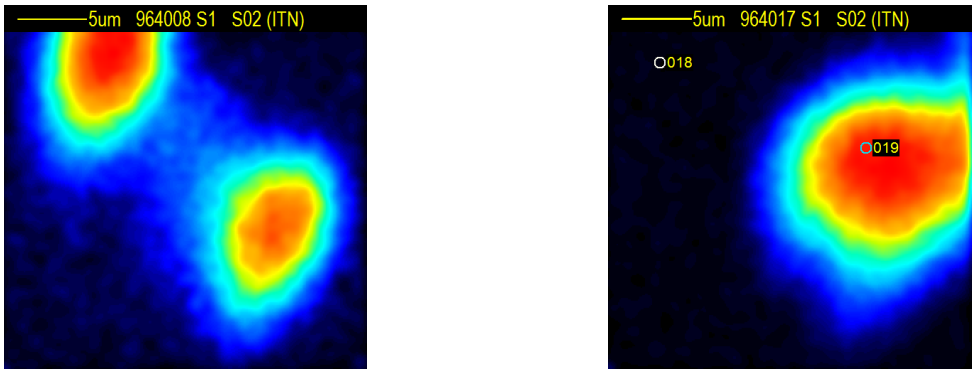

(a) (b)

Figure 4.1: (a) STIM image of the SC_1 sample; (b) STIM image of the SC_1 sample, showing the location of the selected points for analysis of the background (018), corresponding to the $SC_{1,B}$ spectrum, and the cell's matrix (019), corresponding to the $SC_{1,C}$ spectrum.

As visible in Figure 4.1a, the SC_1 sample is comprised of two individual diploid *Saccharomyces cerevisiae* organisms: one in the top-left most area of the scan ($SC_{1,1}$) and another in the bottom right

area of the scan ($SC_{1,2}$). The experimental parameters regarding the analysis of SC_1 are presented in Table 4.1.

Table 4.1: Experimental parameters of the SC_1 analysis

Experimental date	21/09/15	Acquisition time (s)	500
Beam species	Proton ($Z_1 = 1$, $M_1 = 1$)	Beam energy E_0 (MeV)	2.0
Beam current (pA)	100	Beam resolution (μm^2)	3×3
RBS detector angle θ_1 (º)	40	RBS detector FWHM (keV)	20
Scan size (μm^2)	26×26	LM file name (.LMF)	964008
Calibration factor C_0 (keV)	145.265	Calibration factor C_1 (keV/ch)	3.070

To construct the model of the distribution of the CuO-NPs in the sample, it becomes necessary to determine the composition of the cell's biological matrix. In order to identify the matrix, the RBS spectrum data regarding the complete 26×26 μm^2 scan area could be used, presented in Figure 4.2. However, the behaviour of this spectrum results from the convolution of the distribution of elements in the cell along with the distribution of elements in the polycarbonate backing, over which the sample is prepared. More precisely, the composition of a surface layer, which could be attributed to the cells, is distorted by information regarding the polycarbonate backing which, in areas where no cells are present, is also taken as being at the surface level. As such, in order to determine the unknown SC_1 biological matrix, the RBS spectrum ($SC_{1,C}$), provided by the spectrum file `964019R1`, of a single point in a *S. cerevisiae* organism was used. Also, the RBS spectrum ($SC_{1,B}$) of single point in an area where only the polycarbonate backing was evident was analysed in order to compare its matrix with its expected composition ($H_{14}C_{16}O_3$), provided by the spectrum file `964018R1`. The location of both points are presented in Figure 4.1b. Please note that the presence of the polycarbonate backing is common to the analysis presented in Chapters 4.1 and 4.2 and, as such, the methodology of analysis of the biological matrices will be identical.

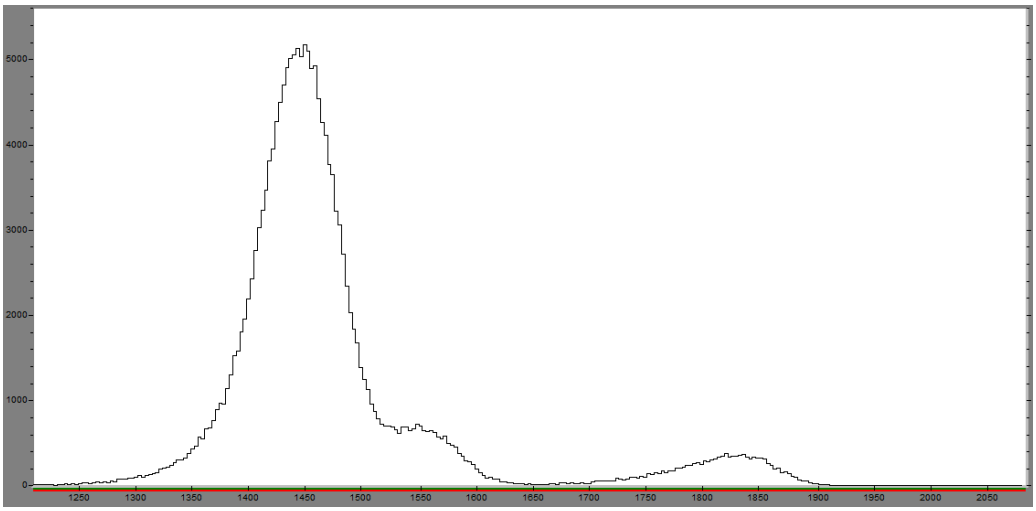

Figure 4.2: The complete scan SC_1 RBS spectrum, using 2.0 MeV ^{1}H ions.

Both spectra were analysed using the OMDAQ program, which enables the fit of experimental data to

simulated elemental spectra and, from the procedures outlined in Chapter 2.4.1, is able to identify its composition and stoichiometry of the sample. The fit of the simulated spectrum to the experimental data of $SC_{1,B}$ is presented in Figure 4.3, and the backing composition is presented in Table 4.2.

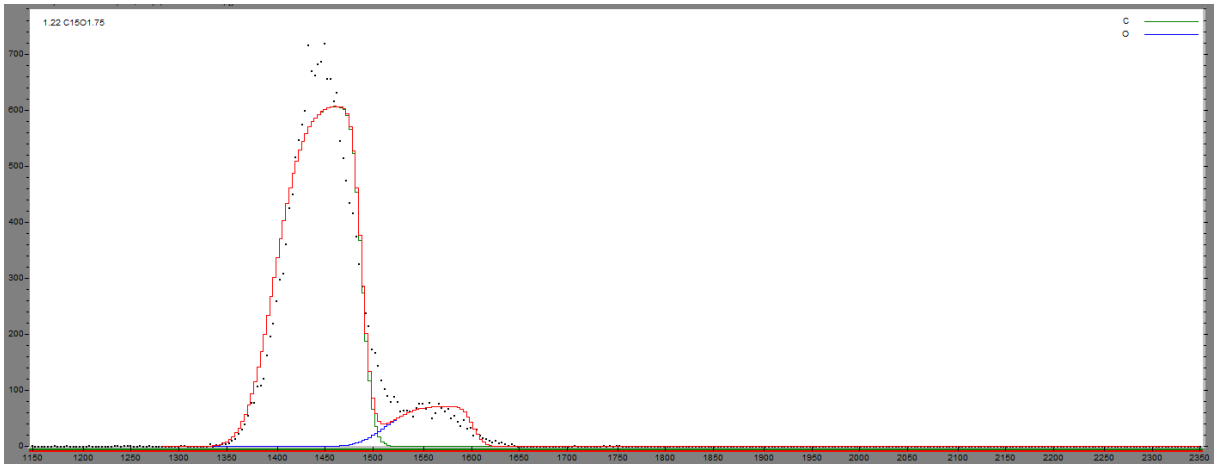

Figure 4.3: Fit of the experimental $SC_{1,B}$ RBS spectrum, using 2.0 MeV ^{1}H ions, obtained in OMDAQ.

Table 4.2: $SC_{1,B}$ RBS spectrum matrix (atomic fraction) and charge collected, regarding the polycarbonate backing.

Matrix	C(15)O(1.75)
Charge collected Q (μC)	0.05

As seen in Figure 4.3, the fit seems to be correctly adjusted to the experimental data, although the underestimation of the oxygen yield for sub-surface events seems to indicate the non-homogeneous distribution of this element in the layer, a fact further hinted by the slope of the surface barrier of C. The existence of biological material, rich in C, over the polycarbonate backing can also contribute to an underestimation of the O proportion in the matrix. Still, the layer's experimental composition ($C_{15}O_{1.75}$) is able to significantly approach the nominal composition of the polycarbonate backing ($H_{14}C_{16}O_3$), discarding the impossibility of identifying hydrogen by the technique, as discussed in Chapter 2. Finally, the fit to the experimental data of $SC_{1,C}$, used to determine the biological matrix of the *S. cerevisiae* organism, is presented in Figure 4.4, and the backing composition is presented in Table 4.3.

From Figure 4.4, it is visible that the fit of the simulated spectrum is able to account with a certain degree of accuracy for the different elements, and corresponding relative proportion, of the $SC_{1,C}$ matrix and, as such, the determined stoichiometry can be used for the creation of the model. However, it is important to note the discrepancies between the yield values of the simulated spectrum and the values of the experimental spectrum, namely regarding the Cu yield and the C yield. As previously discussed in Chapter 2.4.2, the mechanisms of creation of simulated spectra, and their subsequent fit to experimental data is based on the assumption that, for a given multi-elemental layer, the distribution of the elements along the layer is homogeneous, which is visible in Figure 4.4 by the constant plateau in the distributions of single elements that compose the complete simulated spectrum. However, often in biological samples, and notably in cases of nanoparticle contamination, the distribution of these elements are not

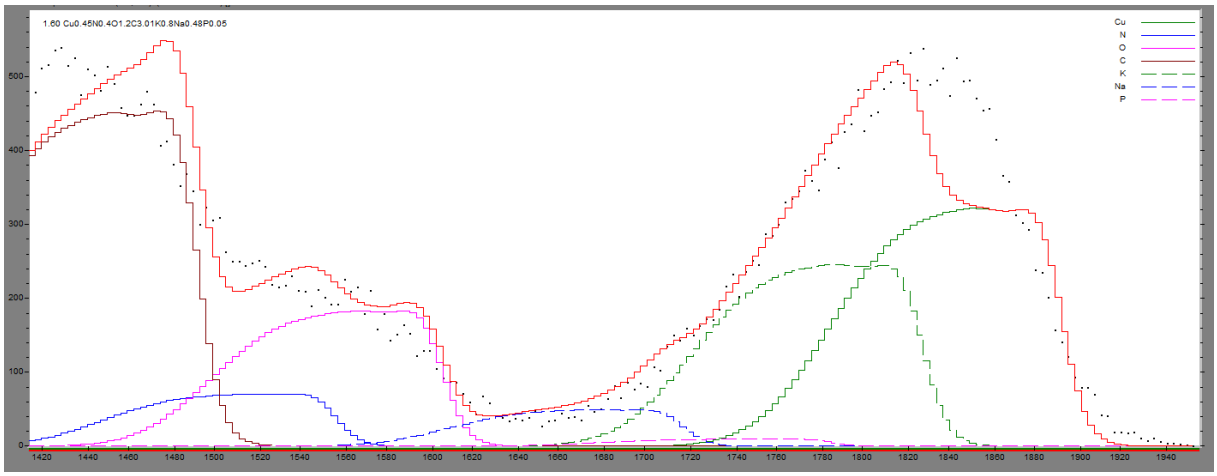

Figure 4.4: Fit of the experimental $SC_{1,C}$ RBS spectrum, using 2.0 MeV ^{1}H ions, obtained in OMDAQ.

homogeneous along the layer that simulates the biological body. Such is the case of the distribution of Cu in this sample, whose surface barrier is clearly underestimated. Still, due to its clear inhomogeneous distribution along the layer, which is visible in the sharp decrease of its yield after the very first surface channels, a compromise between a more realistic yield for the surface barrier, which would overestimate the proportion of Cu in the sample, and a more assertive underestimation of its yield was needed. This factor is further evidenced by the considerable slope in the Cu surface barrier which seems to indicate the inhomogeneity in the Cu distribution in the sample. The same reasoning can be applied for the discrepancies in the C yield, in which the simulated spectrum, analogously to the Cu distribution, suffers from an underestimation of the elemental yield at the surface-barrier and a considerable slope of the same surface barrier. In spite of these discrepancies, the attained matrix can be used to describe the energy loss of the incident ions in the *S. cerevisiae* cells present in the sample and to construct the 3D model of the distribution of Cu in the sample.

Thus, the elemental composition of the SC_1, taken from the $SC_{1,C}$ RBS spectrum analysis, with corresponding atomic fraction in brackets, along with its density ρ, determined accordingly to equation 3.10, is presented in Table 4.3.

Table 4.3: SC_1 RBS spectrum matrix (atomic fraction) and density, concerning the *S. cerevisiae* organisms.

Matrix	C(3.01)N(0.5)O(1.1)Cu(0.45)K(0.8)Na(0.48)P(0.11)
Sample width (μm)	1.60
Density (g/cm^3)	2.023

Before the creation of the distribution of the CuO-NP in MORIA, the question of the validity of the analysis arises. More precisely, the relevant issues are the accessibility of the deeper layers of the sample, while simultaneously conserving low straggling. In order to answer this question, a simulation in SRIM was made, concerning the passage of 30000 ^{1}H ions, with energy $E_0 = 2.0$ MeV, through the sample. The sample matrix is presented in Table 4.3 and the sample width is set at $\Delta t = 3.5\,\mu m$. This width represents the approximate double width of the $SC_{1,C}$ layer, corresponding to double of the average

width of a diploid *S. cerevisiae*, which is useful to take into account the maximum inward and outward trajectory of an ion, incident perpendicularly to the layer's surface. The simulation results concerning the depth achieved by the ions, and the transverse section of the beam, are presented in Figures 4.5a and 4.5b, respectively.

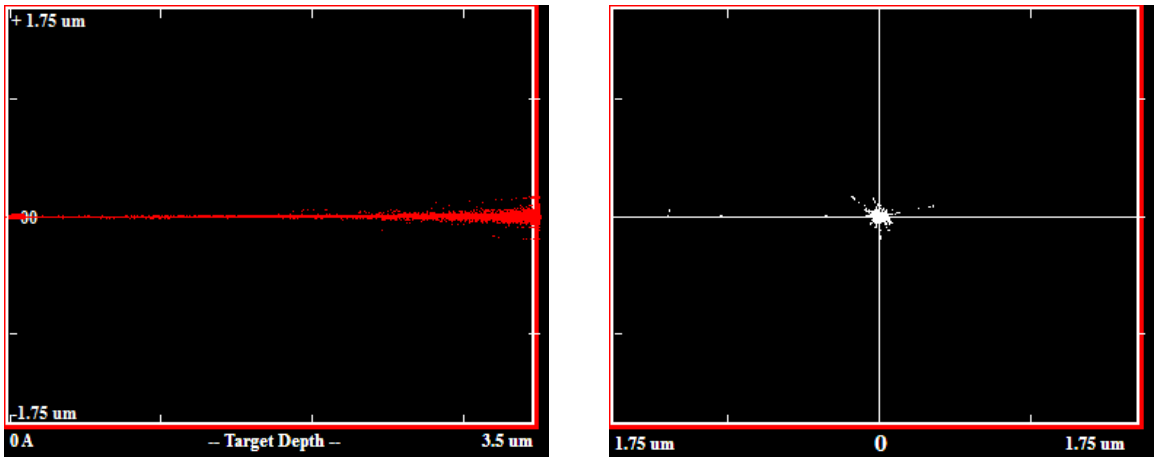

(a) (b)

Figure 4.5: (a) Simulation of the trajectory of a 2.0 MeV ^{1}H beam in the SC_1 sample matrix; (b) Simulation of the transverse section of a 2.0 MeV ^{1}H beam at at its maximum range in SC_1.

As seen in Figure 4.5a, the ions are able to transverse completely the sample's width and, accordingly to Figure 4.5b, with low straggling, accounting to an average lateral spread of $0.1\,\mu m$, considerably lower than the beam's intrinsic resolution of $3 \times 3\,\mu m^2$. As such, the effect of straggling over the results of MORIA's analysis can be considered not significant. The results of the model analysis of the SC_1 sample in MORIA is presented in Table 4.4

Table 4.4: Results of the SC_1 model analysis, obtained using MORIA

Model k_{UL}	Cu ($Z_{UL} = 29, A_{UL} = 63.6$)	t_E (keV/nm)	0.061
K_{UL}	0.946	t_{CH}^{Max}	4
E_{UL} (keV)	1892	t^{Max} (nm)	1011
k_{LL}	K ($Z_{LL} = 19, A_{LL} = 39.1$)	ΔG	64 × 64
K_{LL}	0.914	*Unit* dimensions (X_B, Y_B, Z_B) (μm)	$(0.45, 0.45, 0.33)$
E_{LL} (keV)	1828	*Unit* volume (μm^3)	0.067

The several renders of created model for the distribution of the CuNP in the SC_1 sample are presented in Figures 4.6a to 4.6d.

The initial model, presented in Figure 4.6a, gives rise to the idea that the CuO-NP are fully assimilated into the two diploid *S. cerevisiae* organisms, due to the spherical form of its depth distribution. It's also visible the fact that there exists more CuNP on the area in the vicinity of $SC_{1,1}$ than on the vicinity of

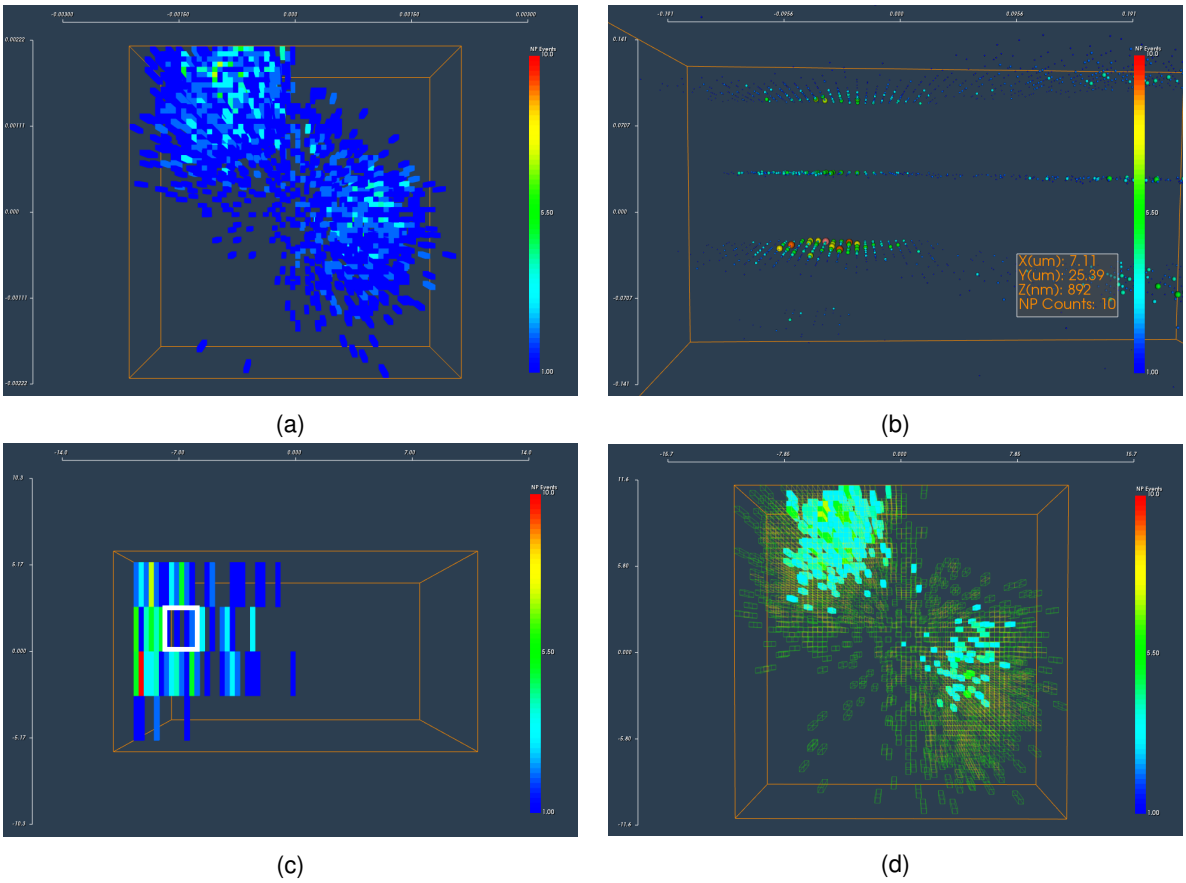

Figure 4.6: MORIA output of the $SC_{1,1}$ sample analysis: (a) 3D distribution of copper in the sample; (b) distribution of copper in the $SC_{1,1}$ cell, using the *Sphereview* visualization option; (c) cross-section cut of the distribution of copper in the $SC_{1,1}$ cell; (d) Surface model of the $SC_{1,1}$ cell, created using the *Surface Creator* function.

$SC_{1,2}$, a fact well established in the usual 2D representation of the scan presented in Figure 4.6a. More interesting is the position of the maximum number of events, presented in Figure 4.6a, which should correspond to the maximum concentration of CuO-NP in the scan, when taken into account the cross-section correction presented in Chapter 3.2.2. Indeed, the maximum number of events in the scan occurs at the coordinates ($7.11\,\mu$m, $25.39\,\mu$m, $0.82\,\mu$m), well inside the $SC_{1,1}$ cell, which indicates that a significant quantity of CuO-NP were in fact assimilated by the cell. This is further confirmed by the cross-section cut of $SC_{1,1}$, presented in Figure 4.6c, taken at the center of the cell, which shows the increase of number of events occurring at increasing depths. Also note that the distribution of CuO-NP in the cell is not uniform, with some areas containing significantly less number of events, which could indicate the presence of cellular organelles which are not as permeable to CuO-NP as the cellular wall. In Figure 4.6c, in white, is the contour of a possible organelle with high impermeability to CuO-NP, with 7 *units* of length. Assuming that the volume of the unknown component is also comprised of 7 *units* of length in the direction perpendicular to the render of Figure 4.6c, and taking the volume of a single individual *unit*, given in Table 4.4, the unknown component has a volume $V \approx 3.3\,\mu\text{m}^3$. The total volume of the $SC_{1,1}$ can be assumed to be the volume of a scalene ellipsoid ($V = 4\pi abc/3$), which with $a = b \approx 6.2/2 = 3.1\,\mu$m and $c \approx 1.5\,\mu$m, where the values where taken using the scale available

in the surface render of Figure 4.6d, thus giving $V_{\mathrm{SC}_{1,1}} \approx 60.35 \mu\mathrm{m}^3$. Since the volume of the nucleus of a *S. cerevisiae* cell is approximately 7% of the total volume of the cell, giving $V_{\mathrm{Nuc}} \approx 4.22\,\mu\mathrm{m}^3$, it seems to indicate that the unknown component can be attributed to the nucleus of the cell, and thus the impermeability of the nucleus to CuO-NP. However further research with longer acquisition times and a higher resolution beam, along with the usage of complementary imaging techniques are needed to fully ascertain the identification. Finally, the *Surface Creator* function, discussed in Chapter B.0.3.8, was used in order to account the number of events that are detected in both $\mathrm{SC}_{1,1}$ and $\mathrm{SC}_{1,2}$, in comparison with the number of events outside them, and the corresponding surface model is presented in Figure 4.6d. The surface's setup, presented as $k_{SC}(k_{SC_{LL}}, P_{k_{SC}})$, and the output of the function is presented in Table 4.5.

Table 4.5: SC_1 surface model results, concerning the *S. cerevisiae* organisms.

Surface Setup	Cl(Si,1)
CuO-NP on the surface ($\%$)	44.34
CuO-NP outside the surface ($\%$)	55.66

Surprisingly, the results of the *Surface Creator* function indicate that approximately half of the number of CuO-NP events are outside both *S. cerevisiae* organisms and, as such, the cells are not as permeable to CuO-NP as previously thought. On the other hand, this also may be the result of the distribution of elements that compose the surface matrix not being uniform inside the cells, which could result in not accounting for CuO-NP in volumes inside the cells where those elements aren't present. However, not only the model seems uniform, as visible in Figure 4.6d, but also the effect of not accounting for those CuO-NP inside the cell should be compensated for the volumes clearly outside the cell which are also part of the surface model, as visible in Figure 4.6d, which also include CuO-NP events. Thus, this may indicate that a small concentration of CuO-NP are distributed along the cells surface, unable to penetrate the cellular wall, which globally account for a high percentage of the total CuO-NP events.

4.1.2.2 SC_2 Sample

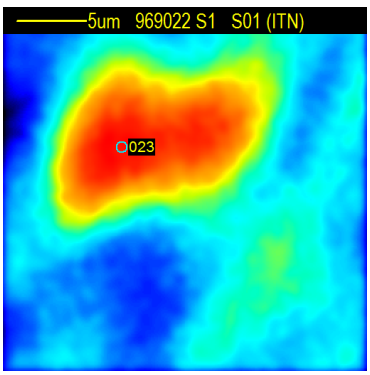

Figure 4.7: STIM image of the SC_2 sample, showing the location of the point (023), corresponding to the cell point.

The SC_2 sample, visible in Figure 4.7, is comprised of a single individual diploid *Saccharomyces cerevisiae* organisms, analysed using an helium ion beam. The experimental parameters regarding the analysis of SC_2 are presented in Table 4.6.

Table 4.6: Experimental parameters of the SC_2 analysis

Experimental date	29/10/15	Acquisition time (min)	30
Beam species	Helium ($Z_1 = 2$, $M_1 = 4$)	Beam energy E_0 (MeV)	2.0
Beam current (pA)	300	Beam resolution (μm^2)	3×3
RBS detector angle θ_1 (º)	40	RBS detector FWHM (keV)	20
Scan size (μm^2)	26×26	LM file name (.LMF)	969022
Calibration factor C_0 (keV)	79.798	Calibration factor C_1 (keV/ch)	1.889

Once again, in order to minimize the contribution of the polycarbonate backing in the sample matrix, the determination of the composition and stoichiometry of unknown biological matrix was done using the RBS spectrum concerning a single point in the cell ($SC_{2,C}$), provided by the spectrum file `969023R1`, in the OMDAQ program. The fit of the experimental data is presented in Figure 4.8.

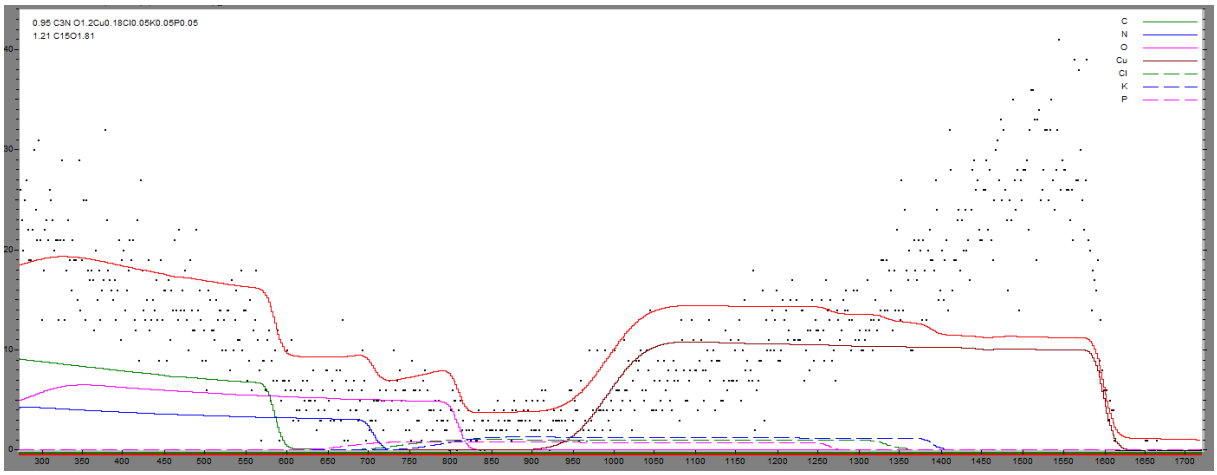

Figure 4.8: Fit of the experimental $SC_{2,C}$ RBS spectrum, using 2.0 MeV ^{4}He ions, obtained in OMDAQ.

While able to explain most of the behaviour of the RBS spectrum, the fit is not able to describe the Cu yield at the surface barrier level, and it is clearly visible the considerable diminishing Cu yield beyond the first surface channels. As in the $SC_{1,C}$ sample case, a compromise between a more severe underestimation of the Cu atomic fraction in the sample and its overestimation was required. Nonetheless, the fit of the simulated spectrum to the experimental data seems adequate and, as such, the elemental composition of the *organic* component of SC_2, with corresponding atomic fraction in brackets and density ρ, determined once again accordingly to equation 3.10, is presented in Table 4.7.

Although the validity of the usage of ^{1}H ion beams, with energy $E_1 = 2.0$ MeV, for the MORIA analysis is proved, the validity for helium ion beams remain. In order to respond to this question, a simulation concerning the passage of 30000 ^{4}He ions, with energy $E_0 = 2.0$ MeV, through the sample defined in Table 4.7, with width $\Delta t = 2\,\mu m$, was run in SRIM. The results of the simulation regarding the maximum

Table 4.7: SC_2 RBS spectrum matrix and density, concerning the *S. cerevisiae* organisms.

Matrix	C(3)O(1.2)N(1)Cu(0.18)Cl(0.05)K(0.05)P(0.05)
Sample width (μm)	0.95
Density (g/cm^3)	1.775

depth achieved by the ions, and the transverse section of the beam, are presented in Figures 4.9a and 4.9b, respectively.

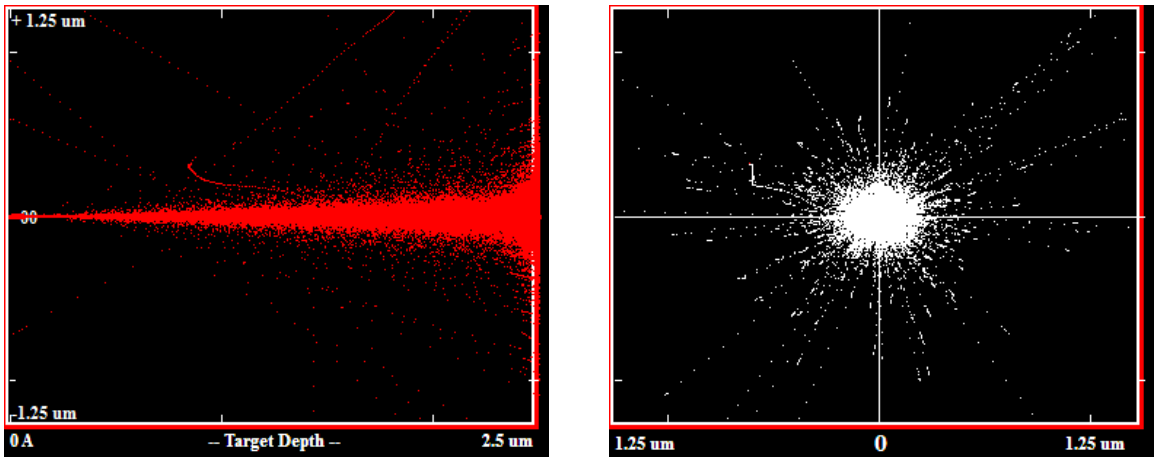

(a) (b)

Figure 4.9: (a) Simulation of the trajectory of a 2.0 MeV ^{4}He beam in the SC_2 sample matrix; (b) Simulation of the transverse section of a 2.0 MeV ^{4}He beam at its maximum range in SC_2.

As seen in Figure 4.9a, the ions are able to transverse completely the sample's width, as in the ^{1}H beam case. However, in comparison with the previous case, there appears to occur a significant increase in the lateral spread of the beam, up to $0.4\,\mu m$, as can be seen in Figure 4.9b. Still, the value is considerably lower than the beam's intrinsic resolution of $3 \times 3\,\mu m^2$ and thus the effects of straggling in the analysis of MORIA can be considered not significant also for helium ion beams with energy $E_0 = 2.0$ MeV. The results of the model analysis of the SC_2 sample in MORIA is presented in Table 4.8

Table 4.8: Results of the SC_2 model analysis, obtained using MORIA

Model k_{UL}	Cu ($Z_{UL} = 29, A_{UL} = 63.6$)	t_E (keV/nm)	0.590
K_{UL}	0.801	t_{CH}^{Max}	11
E_{UL} (keV)	1600	t^{Max} (nm)	340
k_{LL}	K ($Z_{LL} = 19, A_{LL} = 39.1$)	ΔG	64 $\times$ 64
K_{LL}	0.696	*Unit* dimensions (X_B, Y_B, Z_B) (μm)	$(0.45, 0.45, 0.11)$
E_{LL} (keV)	1392	*Unit* volume (μm^3)	0.022

Please note the decreased maximum depth achieved by the model in the helium case. The several renders of created model for the distribution of the CuO-NP in the SC_2 sample are presented in Figures 4.10a to 4.10d.

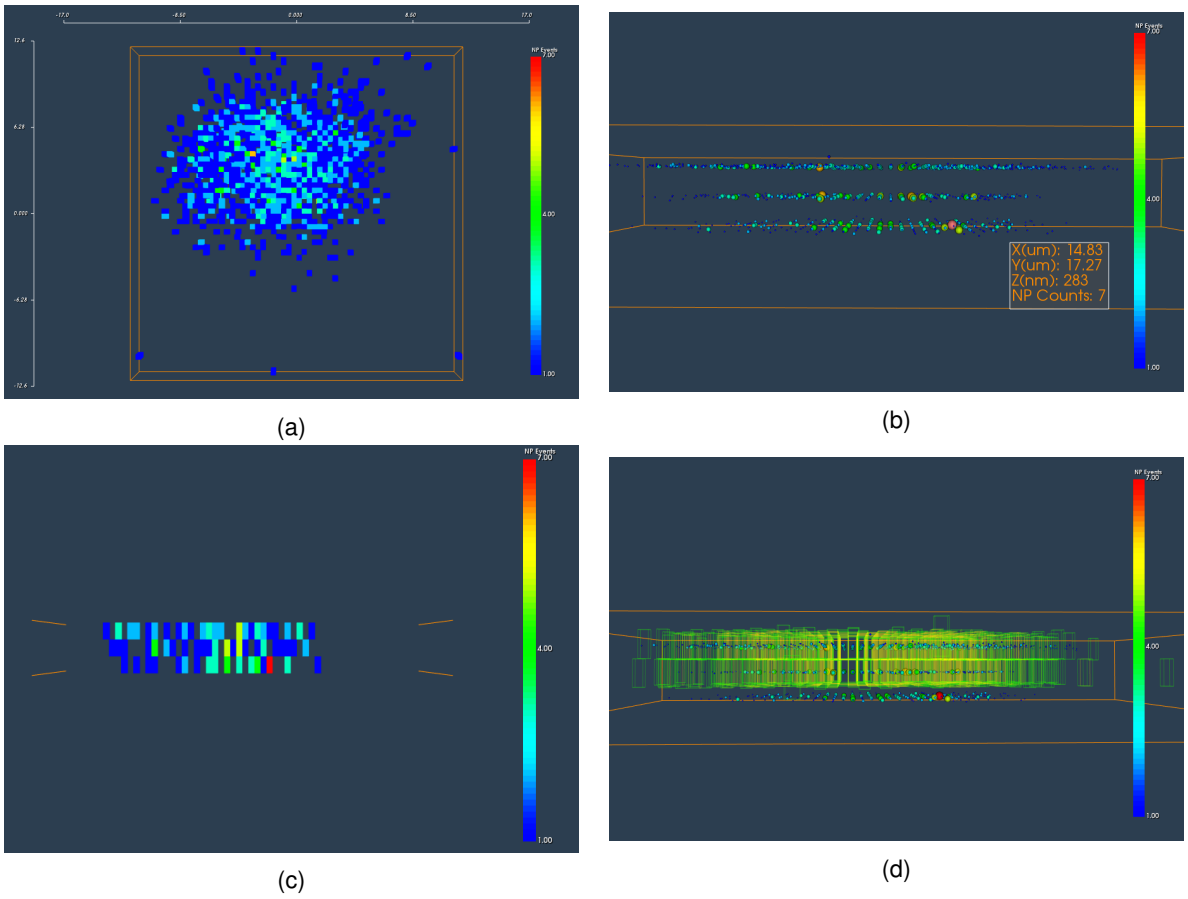

(a) (b) (c) (d)

Figure 4.10: MORIA output of the SC_2 sample analysis: (a) 3D distribution of Cu in the sample; (b) distribution of Cu in the SC_2 cell, using the *Sphereview* visualization option; (c) cross-section cut of the distribution of Cu in the SC_2 cell; (d) Surface model of the SC_2 cell, created using the *Surface Creator* function.

The first significant difference between the ^{1}H beam analysis and the helium ion beam analysis consists in the increased number of depth layers, by almost a factor of 10, due to the considerable increase in the energy loss rate of these particles in the sample. However, for visualization purposes this gain in depth layers does not constitute an advantage since, due to their small number, the increase dispersion of the events hinders the retrieval of information from the model. Still, increasing the maximum number of layers allows for a more comfortable personalized model, by changing their quantity using the function *Relayer*, discussed in Chapter B.0.3.4. As such, the model presented in Figure 4.10a contains only 3 layer channels, each with $\Delta t = 113$ nm. As such, the created model represents the CuO-NP distribution on the surface and sub-surface levels in the cell. Once again, this SC_2 cell seems to have assimilated a considerable amount of CuNP, although the more dispersed distribution seems to indicate a fewer concentration of this nanoparticles actually inside the cell, in comparison with the SC_1 case. This is further indicated by the distribution of the events in the sample which seem to be more homogeneous at the surface level, and with increased spread, in comparison with the SC_1 case, as seen in Figure 4.10b,

and by the cross-section cut of SC_2, visible in Figure 4.10c. More interesting is the clear non-uniformity of the NP spatial distribution in the sub-surface layers, seen in Figure 4.10c, which could give new insight into the issue of the NP entry mechanism in *S. cerevisiae*, currently unresolved [Thabet et al., 2014]. Finally, in this case, the surface model cannot be constructed, in order to access the number of Cu events laid on surface model *units*, to fully probe the deeper layers of the CuO-NP model, as seen in Figure 4.10d.

4.2 *Nematode*

In this section, a sample containing *nematodes* N_1, contaminated with CuO-NP, is analysed using an helium ion beam. The nematode is introduced in Chapter 4.2.1, and the the 3D model of the distribution of CuO-NP is presented in Chapter 4.2.2.

4.2.1 Description

The *nematodes*, also known as roundworms, constitute the phylum *Nematoda*, of the Animal kingdom, well known for their capability of inhabiting a very broad range of environments, their large multiplicity, with about 1 million different species estimated to exist [Lambshead, 1993], and their numerical dominance, accounting for 90% of all animals on the ocean floor [Danovaro et al., 2008] and 80% of all individual animals on earth, often with densities of over a million individuals per square meter [Lorenzen et al., 1994]. Accordingly to their species, nematodes can be parasitic, responsible for several human and plant diseases [Green, 1974], or free-living.

Figure 4.11: Example of a *Nematode* organism.

Usually, nematodes are approximately $5 - 100\,\mu m$ thick , and longer than $0.1\,mm$ [Weischer and Brown], although some parasitic species can reach a meter in length [Fox, 2001]. The anatomy of a nematode can be typically divided in three distinct components: i) the head, containing the mouth, the brain and sensory bristles which provide a sense of touch to the animal; ii) the body, containing four peripheral nerves along its length, responsible for motor control and sensory functions; iii) the intestine, responsible for the nutrient absorption. The animal contains sensory rays, for sensory functions, amongst other structures, which provide the direction of the movement for the animal. More important to the analysis is the muscleless intestine, which forms the main length of the body of the animal. After entering the body

of the nematode in the oral cavity and passing through the pharynx, the CuNP must be deposited along the intestine and, as such, this component must be the focus of the analysis.

4.2.2 Analysis results

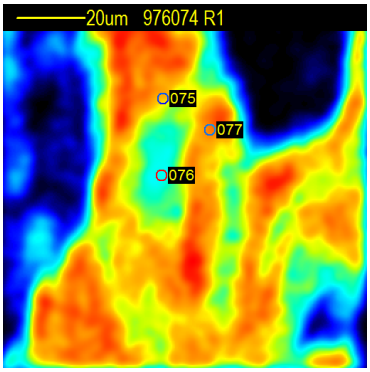

Figure 4.12: STIM image of the N_1 sample, showing the location of the biological point (077), used for the $N_{1,C}$ spectrum.

As presented in Figure 4.12, the N_1 sample contains a section of the body of a nematode. The experimental parameters regarding the analysis of N_1 are presented in Table 4.9.

Table 4.9: Experimental parameters of the N_1 analysis

Experimental date	18/12/15	Acquisition time (min)	30
Beam species	Helium ($Z_1 = 2$, $M_1 = 4$)	Beam energy E_0 (MeV)	2.0
Beam current (pA)	600	Beam resolution (μm^2)	3×3
RBS detector angle θ_1 (º)	40	RBS detector FWHM (keV)	20
Scan size (μm^2)	106×106	LM file name (.LMF)	976074
Calibration factor C_0 (keV)	28.673	Calibration factor C_1 (keV/ch)	3.047

As before, in order to identify the unknown N_1 matrix, regarding its composition and stoichiometry, the RBS spectrum of a biological point representative of the nematode, indicated in Figure 4.12 and provided by the spectrum file `976077R1`, was analysed using the OMDAQ program. The fit of the simulated spectrum to the experimental data is presented in Figure 4.17.

In this case, the fit is able to account for almost the full yield of C in the fit at the surface barrier level, notwithstanding its slope whose meaning was already discussed in previous analysis. Moreover, the underestimation of C yield committed by the simulated spectrum is not significative since the sample is clearly dominated by this element, and therefore, for the calculation of energy loss procedure, which takes the normalized atomic fraction values of the elements in the matrix, the multi-layered sample, in first-approximation, could be simplified to contain only C. Furthermore, the fit is able to describe the concentration of the remaining elements, including the concentration of copper in the sample. Thus, the determined elemental composition, and atomic fraction in brackets, of $N_{1,C}$, along with its density ρ, accordingly to equation 3.10, is presented in Table 4.10.

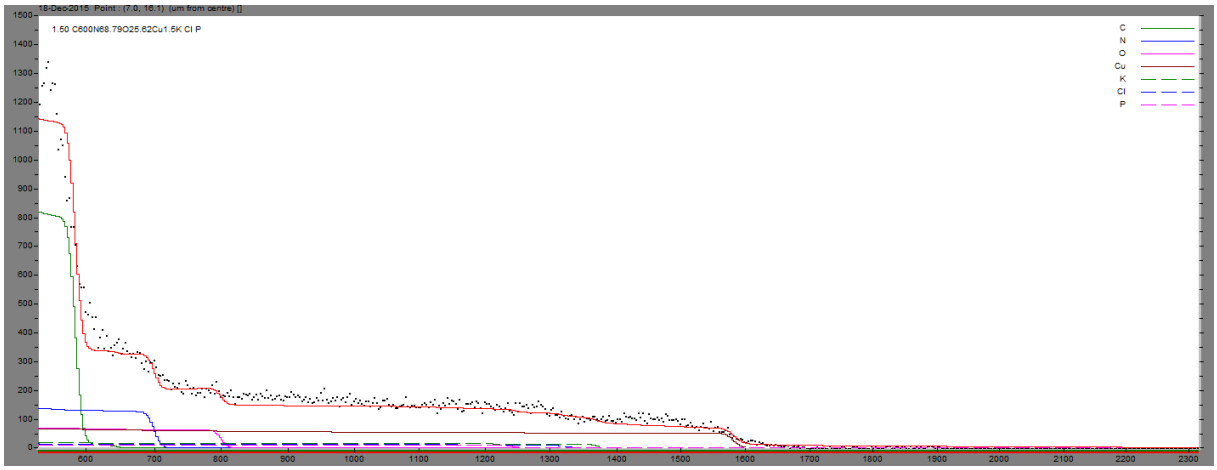

Figure 4.13: Fit of the experimental $N_{1,C}$ RBS spectrum, using 2.0 MeV ^{4}He ions, obtained in OMDAQ.

Table 4.10: $N_{1,C}$ RBS spectrum matrix and density, concerning a *nematode*.

Matrix	C(600)N(68.79)O(25.62)Cu(1.5)K(1)Cl(1)P(1)
Sample width (μm)	1.5
Density (g/cm^3)	1.864

Please note the low concentration of Cu in the sample, which may hinder specific localization in the animal. Once again, before the creation of the 3D model of the distribution of the CuO-NP in MORIA, a simulation in SRIM was made, concerning the passage of 30000 ^{4}He ions, with energy $E_0 = 2.0$ MeV, through a layer of the nematode matrix, is presented in Table 4.10. The width of the layer ($\Delta t = 3.5\,\mu m$) is to be taken as the maximum inward and outward trajectory of an ion, incident perpendicularly to the layer's surface, defined in 4.10. The simulation results concerning the depth achieved by the ions, and the transverse section of the beam, are presented in Figures 4.14a and 4.14b, respectively.

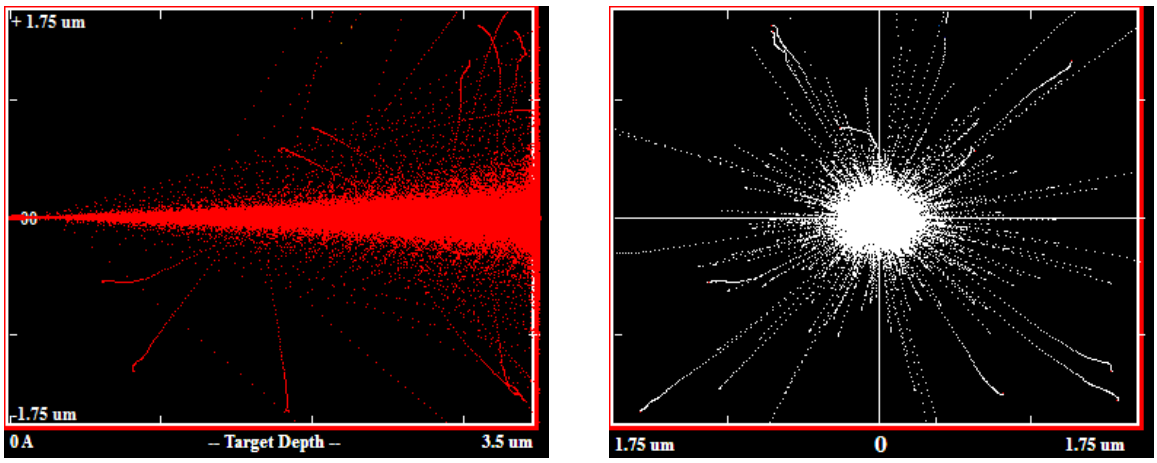

(a) (b)

Figure 4.14: (a) Simulation of the trajectory of a 2.0 MeV ^{4}He beam in the N_1 sample matrix; (b) Simulation of the transverse section of a 2.0 MeV ^{4}He beam at its maximum range in N_1.

Clearly seen in Figure 4.14a, the ^{4}He ions are able to transverse completely the sample's width, although

with values of lateral straggle increasingly significant, of about $0.3\,\mu m$. Still the lateral dispersion of the ions remains pale in comparison with the intrinsic beam lateral resolution of $3 \times 3\,\mu m^2$. Thus, the effects of straggling on the analysis of MORIA can be considered minimum, for that depth range. The results of the model analysis of the N_1 sample in MORIA are presented in Table 4.11.

Table 4.11: Results of the N_1 model analysis, obtained using MORIA

Model k_{UL}	Cu ($Z_{\text{UL}} = 29, A_{\text{UL}} = 63.6$)	t_{E} (keV/nm)	0.634
K_{UL}	0.801	$t_{\text{CH}}^{\text{Max}}$	10
E_{UL} (keV)	1600	t^{Max} (nm)	316
k_{LL}	K ($Z_{\text{LL}} = 19, A_{\text{LL}} = 39.1$)	ΔG	64 × 64
K_{LL}	0.696	*Unit* dimensions (X_B, Y_B, Z_B) (μm)	$(1.65, 1.65, 0.11)$
E_{LL} (keV)	1392	*Unit* volume (μm^3)	0.30

The several renders of created model for the distribution of the CuNP in the N_1 sample are presented in Figures 4.15a to 4.15d.

The initial model, with the default number of layers (10), was not able to provide any information regarding the sample since, due to the low number of events in each cell, no significant pattern would appear. As such, the number of layers was decreased to 3, using the *Relayer* function, and the main model of the distribution of CuO-NP in a nematode is presented in Figure 4.15a. As expected from the low concentration of Cu in the sample matrix, presented in Table 4.10, the low number of events are not able to completely cover the intestine of the nematode, which along with the considerable number of CuNP events distributed randomly outside the body of the animal and the fact of the beam can only probe the surface layers of the sample, contribute to a difficult model to analyse. This low number of CuNP events in the body of the animal can be attributed to a low intake of the nematode to this type of nanoparticles or to a high expelling rate of CuNP off its body. The first hypothesis seems to be preferred since, as seen in Figure 4.15c, the majority of events occur in the most superficial layer of the sample, and thus were not assimilated by the nematode. Figure 4.15b presents the initial model, in which only *units* with $\delta_e = 0.2$, using the function *Sensitivity* whose functioning is discussed in Chapter B.0.3.6. Applying the *Surface Creator* function, discussed in Chapter B.0.3.8, to this updated model, the structure of the body of the animal appears, in concordance with Figure 4.12, and the corresponding surface model is presented in Figure 4.15d. The surface's matrix, and the results concerning the number of events inside and outside the created surface is presented in Table 4.12.

As can be seen in Figure 4.15d, the created volume includes not only the supposed body of the animal, but also organic waste present in the vicinity of the body, which increases the value of CuO-NP that could be associated with the nematode. On the other hand, visible in Figure 4.15a is the existence of gaps in the surface assigned to the body of the animal and, as such, the value of CuO-NP inside the

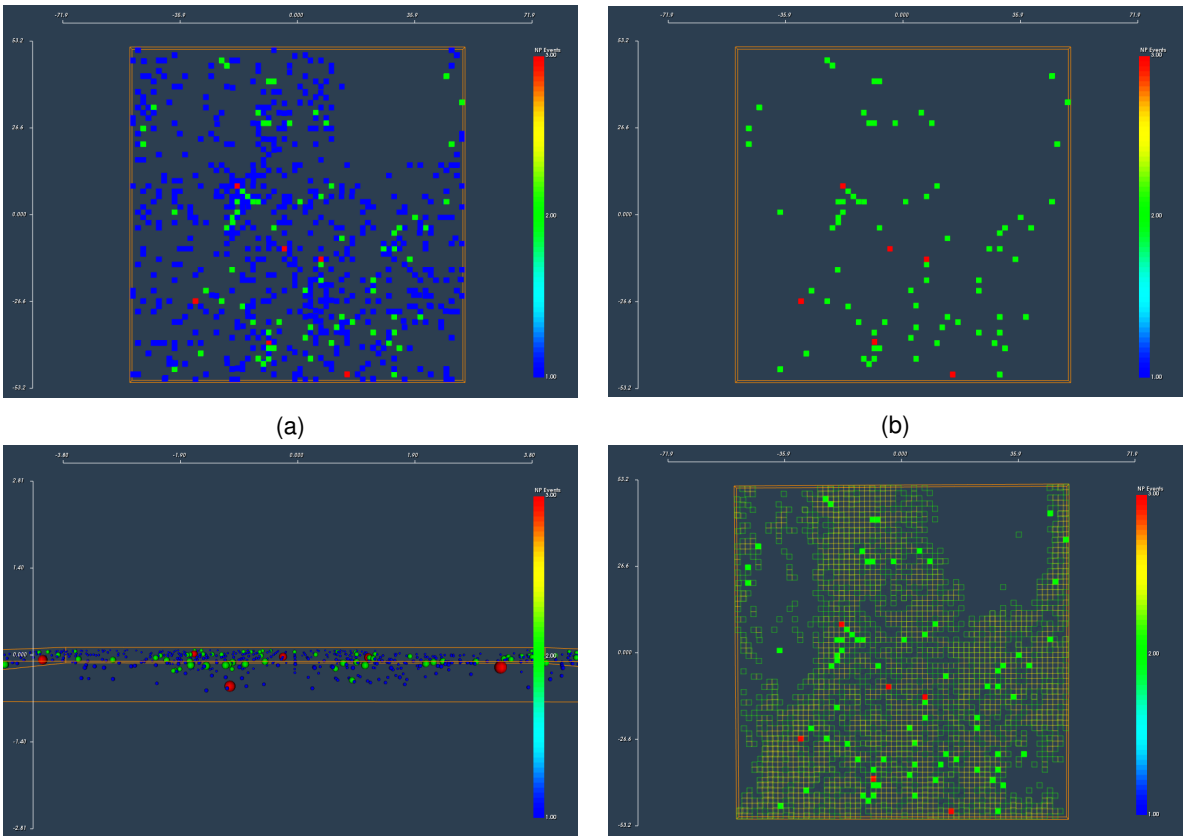

(a) (b)

(c) (d)

Figure 4.15: MORIA output of the N_1 sample analysis: (a) 3D distribution of Cu in the sample; (b) 3D distribution of Cu in the sample, with $\delta_e = 20\%$; (c) transversal view of the distribution of Cu in the sample, using the *Sphereview* option; (d) Surface model of the nematode cell, created using the *Surface Creator* function.

Table 4.12: N_1 *Surface Creator* output, concerning the nematode sample.

Surface Setup	Cl(P,1)P(Na,1)
CuNP on the surface (%)	53.28
CuNP outside the surface (%)	46.72

surface may be underestimated. As such, further investigation with improved surface selection methods are required to fully address this issue.

4.3 *HeLa* cell

In this section, the 3D model distribution of Gold nanoparticles (AuNP) in a sample of HeLa cells (HL_1) is created in MORIA. The discussion of the model is presented in Chapter 4.3.2, after a short description of this type of cell line (Chapter 4.2.1).

4.3.1 Description

HeLa cells, named after the cancer patient Henrietta Lacks from whose tumour the immortal cell line was derived [Scherer et al., 1953], is a cell type widely used in scientific research, comprising the oldest human cell line. HeLa cells are named ”immortal” due to their property of unlimited division in a laboratory cell culture plate, given a nutritive medium. Indeed, normal cells can only divide by mitosis a limited number of times, since the telomeres, the nucleotide sequences that protect the chromosomes from deteriorating, become shorter in each division, which constituted the Hayflick limit [Hayflick and Moorhead, 1961]. On the other hand, cancer cells, such as the HeLa cell, are able to produce telomerases, enzymes responsible for the elongation of the telomeres, and as such can divide indefinitely.

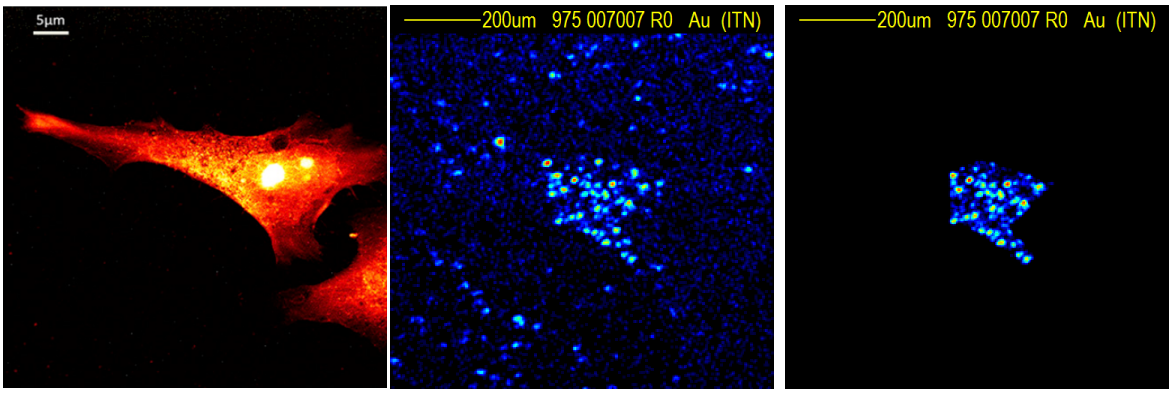

(a) (b) (c)

Figure 4.16: (a) STIM image of a HeLa cell, cultured in an environment with AuNP. Adapted from [Chen et al., 2013a]; (b) RBS distribution of Au in the image of the HL_1 sample; c) Definition of the $HL_{1,M}$ mask region.

Since first isolated and cultured, HeLa cells, presented in Figure 4.16a, have been used extensively in biological research, being involved in the discovery of the vaccine to *Polio* [Scherer et al., 1953] and the first human cell cloning [Puck and Marcus, 1955], due to their fast growth rate. As such, this cell line is ideal to perform scientific research in the biological effects of nanoparticles and the toll of their toxicity.

4.3.2 Analysis results

Contrary to the analysis presented in Chapters 4.1 and 4.2, the experimental analysis of this sample was not made in the microbeam facility in CTN, but was conducted in the Centre for Ion Beam Applications at the National University of Singapore (CIBA@NUS), and the output file of the analysis was kindly provided by CIBA@NUS. As such, much of the experimental parameters were taken directly from the file itself, or from [Chen et al., 2013b].

The Singapore microbeam facility uses a custom data acquisition and imaging system, termed IonDAQ [Bettiol et al., 2009], which enables the customization of the data acquisition process and treatment to their unique microbeam facility. As such, the provided file was incompatible with the OMDAQ software currently used in CTN. Please note that in IonDAQ files, the event coordinates are stored as the sequential pixel number in a 2048×2048 resolution grid, contrary to the pair of coordinates in a 256×256

grid typical of OMDaq files. Still, through reverse engineering of the file, the file was converted into a compatible LM file, compressing the coordinate values and adding the default header structures, named `HeLaRBS.LMF`.

Although the new file contains the data storage structure typical of LM files, presented in Chapter 3.2.1, and MORIA is able to retrieve the multiple energy events, with associated (X,Y) coordinates, the information regarding the calibration of the system and the detector resolution was not present in the file. As such, a new calibration was performed in OMDAQ, previous to the sample's matrix determination, using the noticeable surface energy barriers of Gold and Silicon. Additionally, the detector resolution (FWHM$= 20.0$ keV) was taken from [Chen et al., 2013a]. The results of the new calibration, whose coefficients are defined as in equation 3.1, along with the experimental parameters used are presented in Table 4.13.

Table 4.13: Experimental parameters of the HL_1 analysis, including energy calibration.

Beam Species	Helium ($Z_1 = 2, A_1 = 4$)	RBS Detector FWHM (keV)	20.0
Beam energy E_0 (MeV)	1.6	RBS Detector angle θ_1 (º)	40
LM file name (.LMF)	HeLaRBS	Scan Size (μm^2)	20×20
Calibration C_0 (keV)	137.48	Calibration C_1 (keV/ch)	1.04

After the energy calibration of the spectrum, it is now possible to determine the composition and stoichiometry of the HL_1 matrix, using once again the OMDAQ program. In this case, a region mask of the area containing most of the Au events visible in Figure 4.16b was taken ($HL_{1,M}$), which is represented in Figure 4.16c in order to minimize the effects of the silicon nitrate (Si_3N_4) backing with 50 nm, that is used to hold the samples [Minqin et al., 2007]. The fit of the simulated spectrum to the experimental data of the $HL_{1,M}$ region is presented in Figure 4.17.

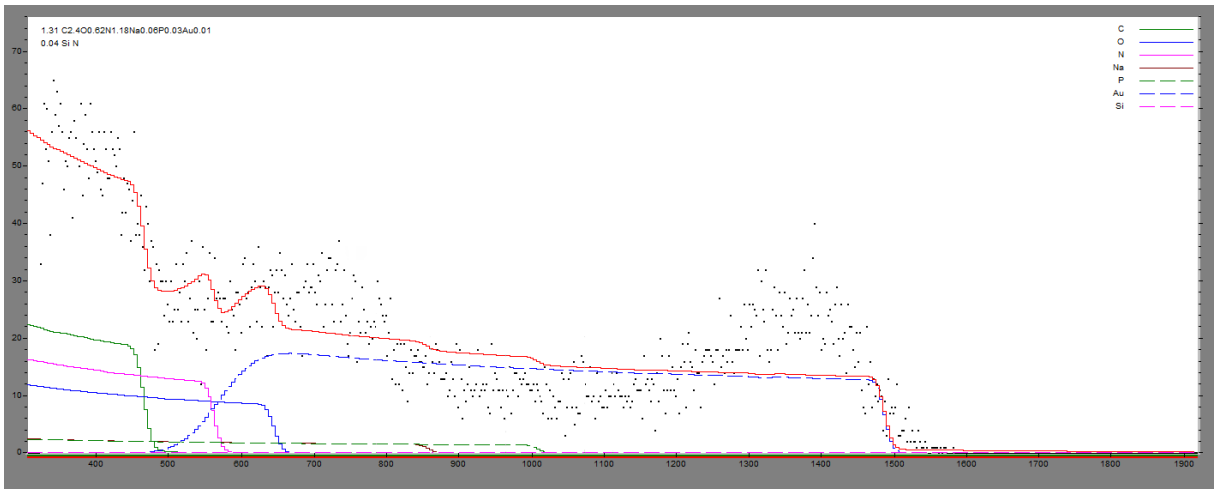

Figure 4.17: Fit of the experimental $HL_{1,M}$ RBS spectrum, using 1.6 MeV ^{4}He ions, obtained in OMDAQ.

The fit seems to be adjusted well to the experimental data. However, it is visible the presence of the receded Si peak, which results from the combination of the events originating from silicon nitride backing after transversing the HeLa cell and events from the borders of the $HL_{1,M}$ mask, which originate from

the backing without transversing the cell completely. This effect could be further minimized by taking a more restrict region for the mask. However, the significant loss in number of events from doing that procedure would degrade considerably the quality of the matrix obtained. Still, the fit is able to justify the experimental data and, as such, the determined elemental matrix is presented in Table 4.14.

Table 4.14: $HL_{1,M}$ RBS spectrum matrix and density, concerning the *HeLa* cell sample.

Matrix	C(2.4)O(0.62)N(1.18)Na(0.06)P(0.03)Au(0.01)
Sample width (μm)	1.312
Density (g/cm^3)	1.529

In order to analyse the behaviour of the beam along the sample, a simulation concerning the passage of 30000 ^{4}He ions, with energy $E_0 = 1.6$ MeV, through a layer, with width$= 3\,\mu$m, of the HeLa cell matrix, was conducted in SRIM. The simulation results concerning the depth achieved by the ions, and the transverse section of the beam, are presented in Figures 4.18a and 4.18b, respectively.

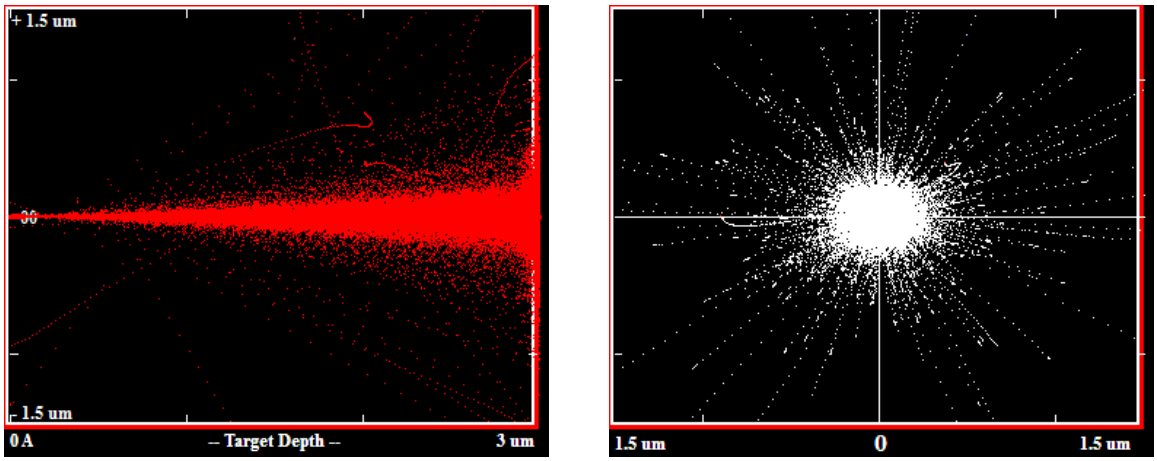

(a) (b)

Figure 4.18: (a) Simulation of the trajectory of a 1.6 MeV ^{4}He beam in the HL_1 sample matrix; (b) Simulation of the transverse section of a 1.6 MeV ^{4}He beam at its maximum range in HL_1.

As expected, the beam is able to completely transverse the sample, although some straggling is evident, due to the low energy of the beam. Still, the analysis in MORIA can be conducted with minimum concerns for straggling effects, whose results are presented in Table 4.15 and the several renders of created model for the distribution of the AuNP in the HL_1 sample are presented in Figures 4.19a to 4.19d. The 3D distribution of Au in the sample is presented in Figure 4.19a. Indeed, due to the increased resolution of the Singapure ion beam for RBS, which is able to achieve a 300 nm beam spot size, the resolution of the model can also be increased to a 128×128 grid with no loss of quality in the visual representation. From Figures 4.19a and 4.19b, the distribution of AuNP across the cell, whose contour can be seen in Figure 4.19d, does not seem homogeneous, but occurring in discrete agglomerates. As such, the discrete agglomerates of nanoparticles in the cell are consistent with their mechanism of entry in the cellular space by endocytosis, by being enclosed in endossomal vesicles [Iversen et al., 2011]. Still, in order to have complete confirmation of this mechanism, further studies are required. However,

Table 4.15: Results of the HL_1 model analysis, obtained using MORIA

Model k_{UL}	Au ($Z_{UL} = 79, A_{UL} = 197$)	t_E (keV/nm)	0.502
K_{UL}	0.931	t_{CH}^{Max}	23
E_{UL} (keV)	1490	t^{Max} (nm)	892
k_{LL}	Si ($Z_{LL} = 14, A_{LL} = 28.1$)	ΔG	18
K_{LL}	0.603	*Unit* dimensions (X_B, Y_B, Z_B) (μm)	$(0.16, 0.16, 0.18)$
E_{LL} (keV)	965	*Unit* volume (μm^3)	0.004

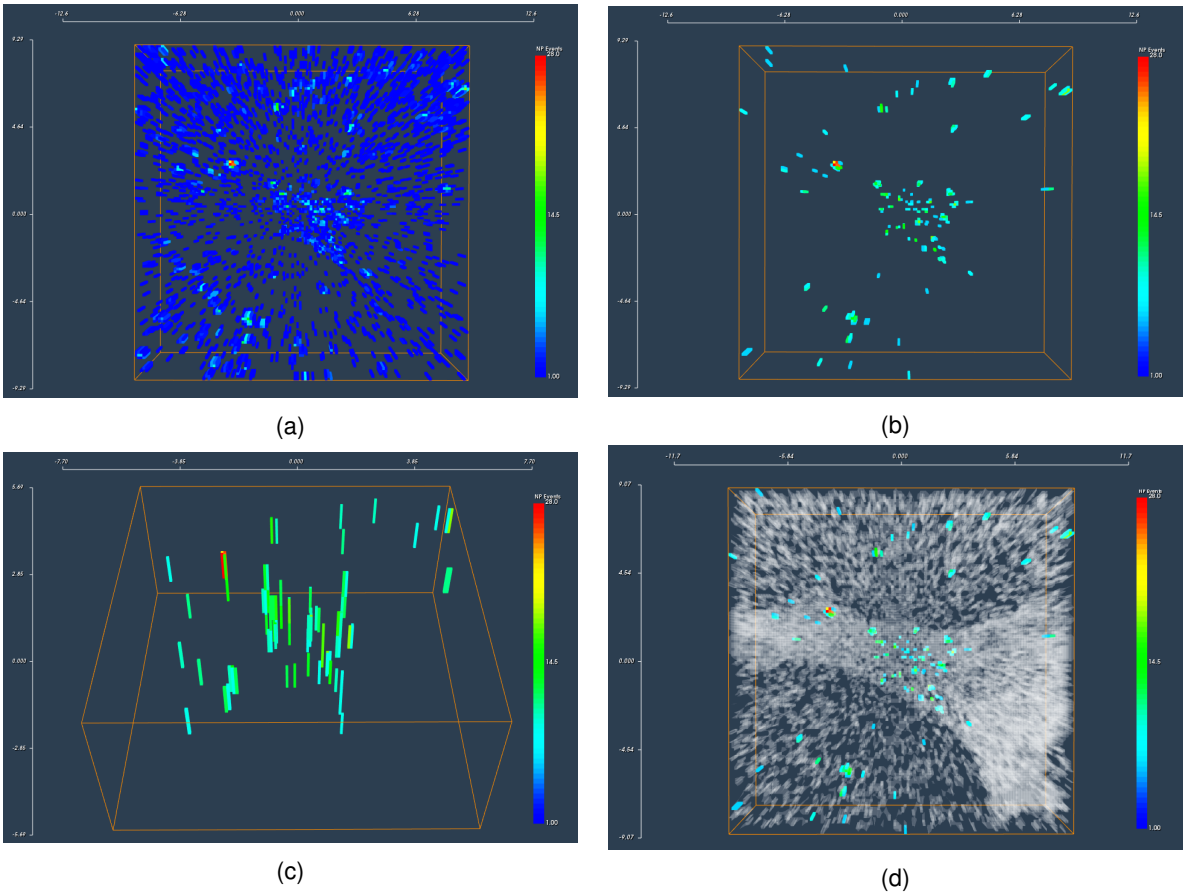

(a) (b) (c) (d)

Figure 4.19: MORIA output of the HL_1 sample analysis: (a) 3D distribution of Au in the sample, with 5 layers; (b) 3D distribution of Au in the sample, with $\delta n_e = 20\%$, using the function *Sensitivity*, with 5 layers.; (c) Secondary view of the 3D distribution of Au in the sample, with 5 layers and $\delta n_e = 20\%$, highlighting the different depths at which the AuNP agglomerates exist in the sample; d) Surface model of the HL_1 sample, created using a Na(O,1) matrix, highlighting the contour of the HeLa cell.

individual agglomerates of nanoparticles can not be differentiated, due to the low depth resolution, when compared to the size of the nanoparticles ($r_{NP} \approx 20$ nm), the low number of events in the sample and the influence of straggling which, as seen in Figure 4.18a, can further decrease the resolution of the beam. As such, the use of complementary techniques, such as STIM, are recommended for a more detailed

understanding of the phenomenon, as conducted in [Chen et al., 2013a].

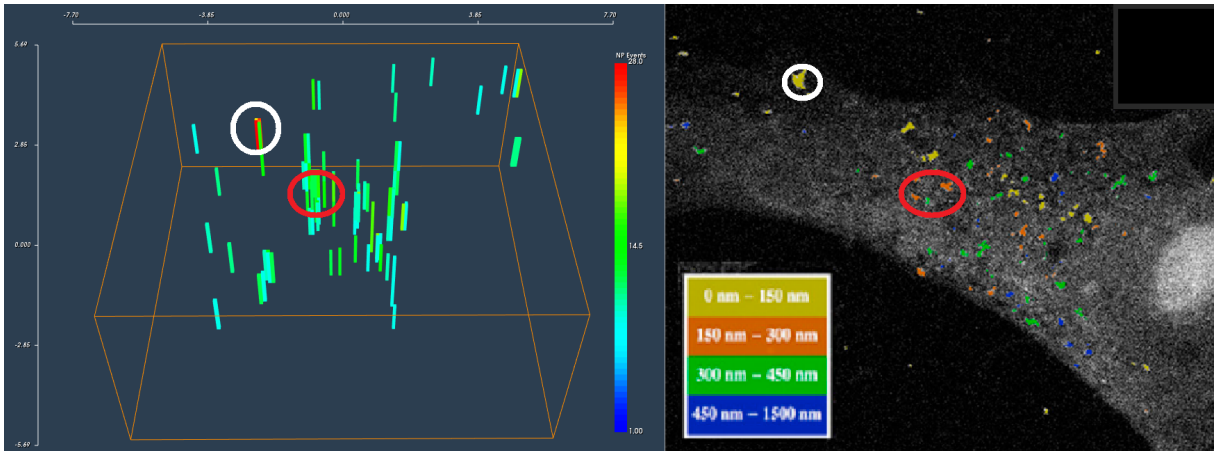

Figure 4.20: Secondary view of the 3D distribution of Au in the sample, with 5 layers and $\delta n_e = 20\%$, highlighting the different depths at which the AuNP exist in the sample along with the distribution of the AuNP in the HeLa cell, with color information regarding its depth (adapted from [Chen et al., 2013a]), which allows the correspondence of the nanoparticle agglomerates in both images.

Still, the created model can effectively achieve the same result of a color scaling to translate depth information in a fully 3D environment, as seen by the correct identification and correspondence of the AuNP agglomerates in Figure 4.20.

Chapter 5

Conclusions and Future Work

The advent and the subsequent rapid development of nanotechnology has lead to its dissemination across a multitude of scientific and industrial fields. Undeniably, one of its sub-fields which has sparked more scientific interest in recent times is nanoparticle research, which has been widely applied to the biomedical, material analysis and electronic fields. However, the proliferation of these small particles may present both significant medical and environmental danger. In order to assess the full potential danger, further research is needed, more specifically regarding nanoparticle quantization and transport mechanisms in the cellular environment. Thus emerges the necessity for improved imaging techniques, which are simultaneously able not only to spatially differentiate individual agglomerates but also to retrieve the depth profile of such agglomerates.

Ion beam analysis has been used extensively in the material analysis field, due to the versatility of its methods and the precision of its results, enabling the description of an unknown sample through the analysis of the output of the interaction between the incident ions of the beam and the sample matrix atoms. Moreover, several ion beam techniques can be performed simultaneously, improving the level of detail of the analysis, such as PIXE, STIM and RBS. In particular, RBS, the detection and analysis of backscattered ions after interacting with the sample's atoms, is able not only to identify the basic elemental matrix of the sample, but also to profile the distribution of those elements along the depth of the sample. As discussed in Chapter 2, the identification of the sample's element is consequence of the elasticity of the interaction of the ion projectile, resulting in a discrete energy loss for the backscattered ions, which is a function only of the masses of the particles and the angle of scattering. Theoretically, at a surface level, the detection of the energy of the backscattered ions should result in distinct barriers, and the identification of the elements that compose the sample's matrix should be straightforward. However, the acceptance of a significant range of angles by the detector, and the fact that the detector has a non-null energy resolution, along with possible tilt angles in the sample are responsible for degrading these barriers. A smaller detection angle, encompassing backscattering angles close to 180^{o}, could be used to minimize the increase the mass resolution of the system, although the cost of lowering the value of the interaction cross-section would be to great for any significant analysis. The depth profiling of the elements of the matrix is a consequence of the energy loss of the projectile ions in the sample

which, for energy ranges in the order of hundreds of keV, should impart small angles in the trajectory of the ions, although the possibility of the occurrence of multiple scattering events, in which the discrete loss of energy takes place multiple times in the trajectory of an ion, is not to be discarded, especially concerning events occurring at deeper depths in the sample, in which the ion has lost a considerable amount of energy and the Rutherford cross-section, if valid, is increased.

Experimentally, the position of a given event in the sample's plane is taken as the position of the beam at the moment of its detection and the depth coordinate is a function of the loss of energy of the particle, in the inward and outward path, characterized by the sample's stopping power. As such, the type of beam, its energy and its resolution become even more paramount in the analysis. As discussed in Chapter 2, the higher stopping power of helium ions in matter, in comparison with protons, translates into an increase in the depth resolution of the system. However the increase in depth channels available for analysis is not followed by a proportional increase in the mass resolution, i.e. the energy difference between the surface barriers of different elements, and as such the total depth accessed by the helium ion analysis is significantly less than the depth accessed by proton beam analysis. This could be resolved by the usage of a higher energy beam which would decrease the value of the stopping power, yet the problem of the validity of the assumption of the Rutherford cross-section would arise. Thus, the choice of the beam species becomes a function of the purpose of the analysis: the inspection of surface and sub-surface sample volumes with high depth resolution, in the order of tens of nanometres, using ^{4}He ions, or a more global analysis of the distribution of a given element in the sample, using ^{1}H ions. The beam spot and resolution are also fundamental parameters to take into account in the quality assessment of analysis since it directly effects the intrinsic resolution of the distribution created. As expected, in respect to the nominal radius of a CuO-NP of 20 nm, it is still understandable the impossibility of defining each individual particle, even more taking into account the $3 \times 3\ \mu$m^2 resolution of the ion beam available at CTN. Another important consideration in the analysis of the quality of the methodology concerns the effect of lateral straggling, which is responsible for further decreasing the resolution of the model, especially for deeper layers in the sample, in which the energy loss of the projectile is more significant. This effect is further exacerbated in the case of ^{4}He ions, which have a lower range in a biological sample in comparison with ^{1}H ions, due to their increased stopping power. Still in the cases of thin biological samples, the effect of lateral straggling, more significant for ^{4}He ions, is minimized due to two factors: the small depth accessible for analysis, which is considerably less than the depth at which straggling becomes notable, and the intrinsic beam resolution, which is commonly greater than the lateral spread originated by a factor of 10. Thus, for biological samples, with thickness in the order of micrometers, RBS constitutes a capable technique for its analysis.

The concurrent capacity of identifying the elemental origin of an event and the ability of placing it in the 3D sample space turns RBS into a powerful imaging technique. However, there existed no dedicated mechanism to readily translate the technique's output data into visual information, which could be more easily understood and analysed. As such, the core focus of this thesis was to fill this gap, through the creation of a new tool, which could be able to display the 3D distribution of a chosen element in the sample's space and interact, in real-time, with the created model. Thus, as presented in Chapter 3, the

MORIA program was created. MORIA is a C++ application, developed using wxWidgets, for the creation of its GUI, and VTK, for the model rendering and real-time interaction mechanisms. wxWidgets allows for cross-platform programming and, as such, the future migration for other operating systems other than Windows can be easily done, at the cost of the lack of personalization of the aspect of the program. VTK also runs in a variety of operating systems and, using its pipeline architecture, is able to integrate, process and render large volume scientific data, with minimal memory footprints. However, the usage of C++ as the basic language of a graphics intensive program leads to a necessity of extremely careful memory management, which for updated versions of the program must be optimized. The program's input was chosen to be the proprietary Listmode filetype, which contains an event-by-event recollection of the analysis, in order to facilitate the data handling between the analysis usually carried out in OMDAQ at CTN and the analysis in MORIA, since LM files already contain many of the parameters needed for the creation of the 3D distribution. However, there should not exist any imperative in the usage of this file and, as such, future versions of the program should allow the use of any ASCII files, containing information regarding the position of the beam and the energy detected. Regarding the program's data processing pipeline, some mechanisms can also be improved in future updates. Currently, the calculation of the energy loss in the sample resorts to the "surface-energy approximation", whose validity for samples with thickness over 1 μm can be argued. Moreover, as discussed in Chapter 2, the energy loss of ions in a sample is not constant along their path in the sample and, as such, and increase in depth resolution should be expected for deeper layers in the model. Still, the principal of using a linear calibration factor could still be valid, if the average of the values of stopping power in the sample are taken. However, the mechanism of the energy loss calculation should be updated in future versions of the program. The "Surface Creator" function should also be updated, especially regarding the calculation of the NP events whose coordinates are equal to those of the surface model. Currently, the function is not able to create the closed volume that correspond to the surface of a biological sample due to the usual non uniformity of the distribution of the elements that compose the surface model in its interior. Hence, NP events inside the corresponding biological body may not be accounted for. However, the solution for this problem is not straight-forward due to the absence of a characteristic element only confined to the exterior limits of the biological body, and, commonly, the distribution of the elements of the surface presents severe spread outside the body. This issue, along with the creation of other supporting functions, needs to be addressed in future updates of the program.

For validation of the program's methodology, several biological samples were analysed, as presented in Chapter 4. The analysis on samples of *Saccharomyces cerevisiae* (Chapter 4.1), exposed to CuO-NP, was conducted using ^{1}H and ^{4}He beams in order to obtain the 3D distribution of the nanoparticles in the cells, which could give insight on the mechanisms of cellular NP intake, and the effectiveness of each beam species for analysis of thin samples. Concerning the case of the proton analysis of the cells, in the complete scan of the sample, the influence of the polycarbonate backing was clearly visible, due to interaction of the beam with the backing in areas where no cells existed. The presence of a backing in which the sample is supported is a necessary hindrance in the analysis, but its effects could be minimized using a thinner backing, composed of elements not commonly present in biological matrices.

In the analysis, in order to minimize this problem, the biological matrix of the sample was identified from the RBS spectrum from a single point in a cell. This methodology was applied to all analyses carried out in CTN. The 3D model of the distribution of Cu, up to a depth $t^{\text{Max}} \approx 1.1$ μm, in two *Saccharomyces cerevisiae* cells revealed that the nanoparticle intake of the cells was significant, yet, the distribution inside the cells exhibits volumes where the presence of NPs was considerably low, which indicates the non-uniformity of their distribution in the celular environment, a suggestion of the impenetrability of cellular organelles for NPs. However, the low resolution of the beam (3×3 μm^2) and the low depth resolution ($\delta z \approx 350$ nm) make it problematic to assert the level of impenetrability. In order to increase the depth resolution obtained by the system, an analysis resorting to ^{4}He ions was also performed. As expected, the depth resolution of the model was increased ($\delta z \approx 40$ nm), at the cost of decreasing significantly the total depth achieved ($t^{\text{Max}} \approx 400$ nm). In this case, the distribution of CuO-NP's inside the cell seems once again non-uniform, with a considerable amount of events originating from surface layers of the cell, which indicates some degree of nanoparticle impenetrability by the cellular wall. In order to evaluate the effect of a thicker sample in the analysis, a sample of *Nematode* organisms were analysed using a ^{4}He ion beam, as presented in Chapter 4.2. As expected from the typical thickness of the *Nematode* body and the simulations carried out of the passage of ^{4}He ions in the biological matrix representative of the organism, the ion beam is unable to access the deeper layers of the animal. Moreover, due to the choice of the species of the beam, the model of the distribution of Cu can only achieve a depth of $t^{\text{Max}} \approx 300$ nm. As such, any conclusions about the model can only account for the surface and sub-surface layers of the model. Still, it is visible the significant difference between the number of events in the surface of the animal and inside the animal which seems to indicate both the external impermeability of the animal to CuO-NPs and the negative bias of the intake of CuO-NPs by the animal. However, a more in depth analysis is required to fully assert the hypothesis.

Finally, to evaluate the effect of a higher resolution beam in the model, the event-by-event recollection of an analysis of HeLa cells, exposed to Au nanoparticles, was kindly provided by the Centre for Ion Beam Applications at the National University of Singapore (CIBA@NUS). The analysis of the provided file is discussed in Chapter 4.3. Due to the impossibility of obtaining a point RBS spectrum, for this analysis a area mask on the original spectrum was created, in order to minimize the presence of the silicon nitrate background. While minimized, the presence of the background is still visible due to the borders of the selected mask, which could not be further constrained due to the decrease in the number of events of the resulting spectrum. In the model, it is clearly visible the potential of a higher resolution beam for the creation of the 3D distribution of nanoparticles in cells, since it enables both the definition of the position of agglomerates of AuNP's in the sample's space, which seem to be discrete contrary to the apparent continuous distribution of CuO-NP's in the *Saccharomyces cerevisiae* cells. As such, the discrete agglomerates of nanoparticles in the cell are consistent with the endocytosis mechanism of entry in the cellular space, enclosed in endossomal vesicles.

The necessity for improved imaging techniques is only expected to increase in the near future, and with it the necessity for improved experimental methodologies and analytical techniques. RBS, due to its maturity in the material analysis field and precision of its results, can also be recognized as a powerful

imaging technique, especially taking into account its ability to probe not only the surface but also the sub-surface of biological samples. At the same time, the ever-changing nature of a computational program such as MORIA allows for the implementation of improvements, many of which already discussed, in future updates, in order to construct a more complete and useful scientific tool. Thus, hopefully, the real value of the work presented will lie in its purpose in scientific research and, hopefully, in its assistance in the never-ending development of improved imaging techniques.

Bibliography

I. A. E. Agency. *NRABASE 2.0. Charged-particle nuclear reaction data for ion beam analysis*. International Atomic Energy Agency, 1997.

I. A. E. Agency. *Instrumentation for PIXE and RBS*. International Atomic Energy Agency, 2000.

U. Amaldi and G. Kraft. Radiotherapy with beams of carbon ions. *Rep. Prog. Phys.*, 68(8):1861–1882, 2005. doi: 10.1088/0034-4885/68/8/r04.

H. H. Andersen, F. Besenbacher, P. Loftager, and W. Moller. Large-angle scattering of light ions in the weakly screened rutherford region. *Phys. Rev. A*, 21(6):1891–1901, 1980. doi: 10.1103/physreva.21.1891.

G. S. Bench. *Scanning Transmission Ion Microscopy*. PhD thesis, University of Melbourne, 1991.

M. J. Berger. ESTAR, PSTAR, and ASTAR: Computer programs for calculating stopping-power and range tables for electrons, protons, and helium ions. Technical report, 1992.

H. Bethe and J. Ashkin. Passage of radiations through matter. *Experimental Nuclear Phys.*, 1:253, 1953.

A. Bettiol, C. Udalagama, and F. Watt. A new data acquisition and imaging system for nuclear microscopy based on a field programmable gate array card. *Nuclear Instruments and Methods in Physics Research Section B: Beam Interactions with Materials and Atoms*, 267(12):2069–2072, 2009.

M. Bozoian. Deviations from rutherford backscattering for z = 1, 2 projectiles. *Nuclear Instruments and Methods in Physics Research Section B: Beam Interactions with Materials and Atoms*, 58(2):127–131, 1991. doi: 10.1016/0168-583x(91)95577-z.

M. Bozoian. A useful formula for departures from rutherford backscattering. *Nuclear Instruments and Methods in Physics Research Section B: Beam Interactions with Materials and Atoms*, 82(4):602–603, 1993. doi: 10.1016/0168-583x(93)96017-7.

M. Bozoian, K. M. Hubbard, and M. Nastasi. Deviations from rutherford-scattering cross sections. *Nuclear Instruments and Methods in Physics Research Section B: Beam Interactions with Materials and Atoms*, 51(4):311–319, 1990. doi: 10.1016/0168-583x(90)90548-9.

M. B. H. Breese, D. N. Jamieson, and P. J. C. King. *Materials analysis using a nuclear microprobe*. John Wiley, 1996.

J. Chadwick. Liv. the gamma rays excited by the beta rays of radium. *Philosophical Magazine Series 6*, 24(142):594–600, 1912. doi: 10.1080/14786441008637362.

Y.-N. Chang, M. Zhang, L. Xia, J. Zhang, and G. Xing. The toxic effects and mechanisms of cuo and zno nanoparticles. *Materials*, 5(12):2850–2871, 2012. doi: 10.3390/ma5122850.

X. Chen, C.-B. Chen, C. Udalagama, N.B., M. Ren, K. E. Fong, L. Y. L. Yung, P. Giorgia, A. A. Bettiol, and F. Watt. High-resolution 3d imaging and quantification of gold nanoparticles in a whole cell using scanning transmission ion microscopy. *Biophysical journal*, 104(7):1419–1425, 2013a. doi: 10.1016/j.bpj.2013.02.015.

X. Chen, C.-B. Chen, C. N. Udalagama, M. Ren, K. E. Fong, L. Y. L. Yung, P. Giorgia, A. A. Bettiol, and F. Watt. High-resolution 3d imaging and quantification of gold nanoparticles in a whole cell using scanning transmission ion microscopy. *Biophysical journal*, 104(7):1419–1425, 2013b.

W. K. Chu. Calculation of energy straggling for protons and helium ions. *Phys. Rev. A*, 13(6):2057–2060, 1976. doi: 10.1103/physreva.13.2057.

R. Danovaro, C. Gambi, A. Dell'Anno, C. Corinaldesi, S. Fraschetti, A. Vanreusel, M. Vincx, and A. J. Gooday. Exponential decline of deep-sea ecosystem functioning linked to benthic biodiversity loss. *Current Biology*, 18(1):1–8, 2008.

Digitalmars.com. Implib, 2016. URL `http://digitalmars.com/ctg/implib.html`.

H. Dong, L. Xia, Z. Peng, and J. Zhang. 3d-visualization for dicom series based on itk and vtk. *AMM*, 263-266:2530–2533, 2012. doi: 10.4028/www.scientific.net/amm.263-266.2530.

Y. Q. Feng and K. Wang. 3-d image reconstruction in optical coherence tomography systems based on vtk in oct systems. *AMR*, 459:320–323, 2012. doi: 10.4028/www.scientific.net/amr.459.320.

J.-J. Fernandez. Computational methods for electron tomography. *Micron*, 43(10):1010–1030, 2012. doi: 10.1016/j.micron.2012.05.003.

O. Firsov. Calculation of the Interaction Potential of Atoms. *Soviet Journal of Experimental and Theoretical Physics*, 6:534, 1958.

B. Fischer. The heavy-ion microprobe at gsi - used for single ion micromechanics. *Nuclear Instruments and Methods in Physics Research. Section B: Beam Interactions with Materials and Atoms*, 30(3):284–288, 1988. doi: 10.1016/0168-583x(88)90012-2.

R. Fox. *Invertebrate zoology: A functional evolutionary approach*. Wadsworth Publishing., 2001.

M. Frank, L. J. Hiller, J. B. le Grand, C. A. Mears, S. E. Labov, M. A. Lindeman, H. Netel, D. Chow, and A. Barfknecht. Energy resolution and high count rate performance of superconducting tunnel junction x-ray spectrometers. *Rev. Sci. Instrum.*, 69(1):25, 1998. doi: 10.1063/1.1148474.

H. Geiger and E. Marsden. Lxi. the laws of deflexion of a particles through large angles. *Philosophical Magazine Series 6*, 25(148):604–623, 1913. doi: 10.1080/14786440408634197.

R. M. Godinho, M. T. Cabrita, L. C. Alves, and T. Pinheiro. Imaging of intracellular metal partitioning in marine diatoms exposed to metal pollution: consequences to cellular toxicity and metal fate in the environment. *Metallomics*, 6(9):1626, 2014. doi: 10.1039/c4mt00105b.

E. Goldstein. Ueber eine noch nicht untersuchte strahlungsform an der kathode inducirter entladungen. *Ann. Phys.*, 300(1):38–48, 1898. doi: 10.1002/andp.18983000105.

C. Green. Nematode ecology and plant disease. *Agro-Ecosystems*, 1:269–270, 1974. doi: 10.1016/0304-3746(74)90035-3.

G. Grime and M. Dawson. Recent developments in data acquisition and processing on the oxford scanning proton microprobe. *Nuclear Instruments and Methods in Physics Research Section B: Beam Interactions with Materials and Atoms*, 104(1):107–113, 1995.

G. Grime and F. Watt. A survey of recent pixe applications in archaeometry and environmental sciences using the oxford scanning proton microprobe facility. *Nuclear Instruments and Methods in Physics Research Section B: Beam Interactions with Materials and Atoms*, 75(1-4):495–503, 1993. doi: 10.1016/0168-583x(93)95703-8.

R. W. Hamm and M. E. Hamm. *Industrial accelerators and their applications*. World Scientific, 2012.

G. Han, L. R. Martinez, M. R. Mihu, A. J. Friedman, J. M. Friedman, and J. D. Nosanchuk. Nitric oxide releasing nanoparticles are therapeutic for staphylococcus aureus abscesses in a murine model of infection. *PLoS ONE*, 4(11):e7804, 2009. doi: 10.1371/journal.pone.0007804.

L. Hayflick and P. S. Moorhead. The serial cultivation of human diploid cell strains. *Experimental cell research*, 25(3):585–621, 1961.

I. Herskowitz. Life cycle of the budding yeast saccharomyces cerevisiae. *Microbiological reviews*, 52(4):536, 1988.

C.-M. J. Hu, R. H. Fang, J. Copp, B. T. Luk, and L. Zhang. A biomimetic nanosponge that absorbs pore-forming toxins. *Nature Nanotech*, 8(5):336–340, 2013. doi: 10.1038/nnano.2013.54.

T.-G. Iversen, T. Skotland, and K. Sandvig. Endocytosis and intracellular transport of nanoparticles: present knowledge and need for future studies. *Nano Today*, 6(2):176–185, 2011.

P. Jorgensen, N. P. Edgington, B. L. Schneider, I. Rupeš, M. Tyers, and B. Futcher. The size of the nucleus increases as yeast cells grow. *Molecular Biology of the Cell*, 18(9):3523–3532, 2007.

F. M. Klis, P. Mol, K. Hellingwerf, and S. Brul. Dynamics of cell wall structure in saccharomyces cerevisiae. *FEMS Microbiology Reviews*, 26(3):239–256, 2002.

F. M. Klis, C. G. de Koster, and S. Brul. Cell wall-related bionumbers and bioestimates of saccharomyces cerevisiae and candida albicans. *Eukaryotic Cell*, 13(1):2–9, 2014.

T. Kluge. c++ cubic spline interpolation library, 2016. URL `http://kluge.in-chemnitz.de/opensource/spline/`.

J. Knapp, D. Brice, and J. Banks. Trace element sensitivity for heavy ion backscattering spectrometry. *Nuclear Instruments and Methods in Physics Research Section B: Beam Interactions with Materials and Atoms*, 108(3):324–330, 1996. doi: 10.1016/0168-583x(95)01051-3.

M. Knoll and E. Ruska. Das elektronenmikroskop. *Zeitschrift für Physik*, 78(5-6):318–339, 1932.

P. Lambshead. Recent developments in marine benthic biodiversity research. *Oceanis*, 19:5–5, 1993.

C. R. Landry, J. P. Townsend, D. L. Hartl, and D. Cavalieri. Ecological and evolutionary genomics of saccharomyces cerevisiae. *Molecular ecology*, 15(3):575–591, 2006.

P. Lechner, H. Soltau, C. Fiorini, A. Longoni, G. Lutz, and L. Struuder. Silicon drift detectors for high resolution, high count rate x-ray spectroscopy at room temperature. *Powder Diffr.*, 18(2):175, 2003. doi: 10.1154/1.1706959.

J. L'Ecuyer, J. Davies, and N. Matsunami. How accurate are absolute rutherford backscattering yields. *Nuclear Instruments and Methods*, 160(2):337–346, 1979. doi: 10.1016/0029-554x(79)90612-8.

G. J. F. Legge, C. D. McKenzie, and A. P. Mazzolini. The melbourne proton microprobe. *Journal of Microscopy*, pages 185–200, 1979.

J. Lindhard and M. Scharff. Energy dissipation by ions in the kev region. *Phys. Rev.*, 124(1):128–130, 1961. doi: 10.1103/physrev.124.128.

S. Lorenzen et al. *The phylogenetic systematics of free living nematodes.* Ray society, 1994.

M. Mayer. Simnra, a simulation program for the analysis of nra, rbs and erda. In *American Institute of Physics Conference Proceedings*, pages 541–544. Iop Institute Of Physics Publishing LTD, 1999.

R. Mendes Godinho, J. Raimundo, C. Vale, B. Anes, P. Brito, L. Alves, and T. Pinheiro. Micro-scale elemental partition in tissues of the aquatic plant lemna minor l. exposed to highway drainage water. *Nuclear Instruments and Methods in Physics Research Section B: Beam Interactions with Materials and Atoms*, 306:150–152, 2013. doi: 10.1016/j.nimb.2012.10.032.

R. Minqin, J. Van Kan, A. Bettiol, L. Daina, C. Y. Gek, B. B. Huat, H. Whitlow, T. Osipowicz, and F. Watt. Nano-imaging of single cells using stim. *Nuclear Instruments and Methods in Physics Research Section B: Beam Interactions with Materials and Atoms*, 260(1):124–129, 2007.

V. Mohanraj and Y. Chen. Nanoparticles: a review. *Tropical Journal of Pharmaceutical Research*, 2006. URL `http://www.tjpr.freehosting.net`.

R. K. Mortimer and J. R. Johnston. Genealogy of principal strains of the yeast genetic stock center. *Genetics*, 113(1):35–43, 1986.

D. Mous, R. Haitsma, T. Butz, R.-H. Flagmeyer, D. Lehmann, and J. Vogt. The novel ultrastable hvee 3.5 mv singletron accelerator for nanoprobe applications. *Nuclear Instruments and Methods in Physics Research Section B: Beam Interactions with Materials and Atoms*, 130(1-4):31–36, 1997. doi: 10.1016/s0168-583x(97)00186-9.

D. Muller, L. F. Kourkoutis, M. Murfitt, J. Song, H. Hwang, J. Silcox, N. Dellby, and O. Krivanek. Atomic-scale chemical imaging of composition and bonding by aberration-corrected microscopy. *Science*, 319(5866):1073–1076, 2008.

M. Nastasi, J. W. Mayer, and Y. Wang. *Ion beam analysis: fundamentals and applications*. CRC Press, 2014.

R. Norarat, V. Marjomski, X. Chen, M. Zhaohong, R. Minqin, C.-B. Chen, A. Bettiol, H. Whitlow, and F. Watt. Ion-induced fluorescence imaging of endosomes. *Nuclear Instruments and Methods in Physics Research Section B: Beam Interactions with Materials and Atoms*, 306:113–116, 2013. doi: 10.1016/j.nimb.2012.12.052.

M. Oberkofler, R. Piechoczek, and C. Linsmeier. Optimized analysis of deuterium depth profiles in beryllium. *Physica Scripta*, 2011(T145):014011, 2011. URL `http://stacks.iop.org/1402-4896/2011/i=T145/a=014011`.

N. Ogrinc, P. Pelicon, P. Vavpetic, M. Kelemen, N. Grlj, L. Jeromel, S. Tomic, M. Colic, and A. Beran. Quantitative assay of element mass inventories in single cell biological systems with micro-pixe. *Nuclear Instruments and Methods in Physics Research Section B: Beam Interactions with Materials and Atoms*, 306:121–124, 2013. doi: 10.1016/j.nimb.2012.12.060.

P. Pelicon, N. C. Podaru, P. Vavpetic, L. Jeromel, N. Ogrinc Potocnik, S. Ondracka, A. Gottdang, and D. J. Mous. A high brightness proton injector for the tandetron accelerator at jozef stefan institute. *Nuclear Instruments and Methods in Physics Research Section B: Beam Interactions with Materials and Atoms*, 332:229–233, 2014. doi: 10.1016/j.nimb.2014.02.067.

T. T. Puck and P. I. Marcus. A rapid method for viable cell titration and clone production with hela cells in tissue culture: the use of x-irradiated cells to supply conditioning factors. *Proceedings of the National Academy of Sciences of the United States of America*, 41(7):432, 1955.

S. Rubin, T. O. Passell, and L. E. Bailey. Chemical analysis of surfaces by nuclear methods. *Anal. Chem.*, 29(5):736–743, 1957. doi: 10.1021/ac60125a001.

W. F. Scherer, J. T. Syverton, and G. O. Gey. Studies on the propagation in vitro of poliomyelitis viruses iv. viral multiplication in a stable strain of human malignant epithelial cells (strain hela) derived from an epidermoid carcinoma of the cervix. *The Journal of Experimental Medicine*, 97(5):695–710, 1953.

W. Schroeder, K. Martin, and B. Lorensen. *VTK*. Kitware, 2015.

M. Scott, C.-C. Chen, M. Mechlenburg, C. Zhu, R. Xu, C. Regan, J. Miao, P. Ercius, and U. Dahmen. Electron tomography at 2.4 å resolution. *Microscopy and Microanalysis*, 18(S2):522–523, 2012.

G. T. Seaborg and J. J. Livingood. Artificial radioactivity as a test for minute traces of elements. *J. Am. Chem. Soc.*, 60(8):1784–1786, 1938. doi: 10.1021/ja01275a018.

A. Sedighi, M. Montazer, and N. Hemmatinejad. Copper nanoparticles on bleached cotton fabric: in situ synthesis and characterization. *Cellulose*, 21(3):2119–2132, 2014. doi: 10.1007/s10570-014-0215-5.

A. Shariff, V. Auzelyte, M. Elfman, P. Kristiansson, K. Malmqvist, C. Nilsson, J. Pallon, and M. Wegdon. The lund nuclear microprobe sub-micron set-up. part i: Ion optics calculation. *Nuclear Instruments and Methods in Physics Research Section B: Beam Interactions with Materials and Atoms*, 231(1-4): 1–6, 2005. doi: 10.1016/j.nimb.2005.01.026.

F. Sherman. Getting started with yeast. *Methods in Enzymology*, 350:3–41, 2002.

E. Silver, M. LeGros, N. Madden, J. Beeman, and E. Haller. High-resolution, broad-band microcalorimeters for x-ray microanalysis. *X-Ray Spectrom.*, 25(3):115–122, 1996. doi: 10.1002/(sici)1097-4539(199605)25:3⟨115::aid-xrs140⟩3.0.co;2-s.

J. Smart, K. Hock, and S. Csomor. *Cross-platform GUI programming with wxWidgets*. URL `https://www.wxwidgets.org/docs/book/`.

J. Stark. Zur diskussion uber die intensitutsverteilung im kanalstrahlenspektrum. *Ann. Phys.*, 344(16): 1185–1200, 1912. doi: 10.1002/andp.19123441607.

H. Takayama, K. Iwasaki, K. Hayashi, and M. Takai. Development of nanoprobe tof-rbs system for semiconductor process. *Nuclear Instruments and Methods in Physics Research Section B: Beam Interactions with Materials and Atoms*, 210:108–112, 2003. doi: 10.1016/s0168-583x(03)01049-8.

A. C. Telea. *Data Visualization*. CRC Press, 2014.

S. Thabet, F. Simonet, M. Lemaire, C. Guillard, and P. Cotton. Impact of photocatalysis on fungal cells: depiction of cellular and molecular effects on saccharomyces cerevisiae. *Applied and environmental microbiology*, 80(24):7527–7535, 2014.

S. Van Aert, K. J. Batenburg, M. D. Rossell, R. Erni, and G. Van Tendeloo. Three-dimensional atomic imaging of crystalline nanoparticles. *Nature*, 470(7334):374–377, 2011.

Y. Wang. *Handbook of modern ion beam materials analysis*. Materials Research Society, 2009.

F. Watt, M. B. Breese, A. A. Bettiol, and J. A. van Kan. Proton beam writing. *Materials Today*, 10(6): 20–29, 2007. doi: 10.1016/s1369-7021(07)70129-3.

B. Weischer and D. J. Brown. *An introduction to nematodes: general nematology: a student's textbook*. Number 1.

C. v. Weizsäcker. Zur theorie der kernmassen. *Zeitschrift für Physik A Hadrons and Nuclei*, 96(7): 431–458, 1935.

Wxvtk.sourceforge.net. wxvtkrenderwindowinteractor, 2003. URL `http://wxvtk.sourceforge.net/`.

J. F. Ziegler, J. P. Biersack, and M. D. Ziegler. *SRIM, the stopping and range of ions in matter*. SRIM Co., 2008. URL `http://www.srim.org/SRIM/SRIMPICS/STOPPLOTS.htm`.

L. Zolnai and S. Szilgyi. An effective method for spectra storage. *Nuclear Instruments and Methods in Physics Research Section B: Beam Interactions with Materials and Atoms*, 14(3):360–362, 1986. doi: 10.1016/0168-583x(86)90606-3.

Appendix A

Energy Straggling

As discussed in Chapter 2.3.1, the energy loss mechanism for ion beams in a given sample is mainly due to discrete interactions with atomic electrons. As such, the exact number of these collisions and the geometrical after-effect are subjected to statistical uncertainty, which results in the distribution of the initial mono-energetic beam ions, after traversing a given length in the sample. This phenomenon is titled energy straggling Ω_{E}, given by:

$$\left(\Omega_{\mathsf{E}}\right)^2 = \sum_i \left(\Omega_i\right)^2 \tag{A.1}$$

where Ω_i refers to the several contributions, statistical and non-statistical, to the overall energy straggling. The distribution of the energy loss of the ions in the beam at a given depth can be modelled through a Gaussian distribution, with variance $\left(\Omega_{\mathsf{E}}\right)^2$:

$$P(E)dE = \frac{1}{\sqrt{2\pi}\Omega_{\mathsf{E}}} \exp\left(\frac{-E^2}{2\Omega_{\mathsf{E}}^2}\right) dE \tag{A.2}$$

The statistical dependence of the energy straggling arises from fluctuations in the electronic interactions, becoming more important in the high-energy regime defined in Chapter 2.3.1. In this regime, the fully-stripped ions interact with the atomic electrons and the energy straggle Ω_{B} (Bohr energy straggle) can be defined as:

$$\Omega_{\mathsf{B}}^2 = \left\langle T^2 \right\rangle \tag{A.3}$$

where T is the kinetic energy transferred by the ion to the electron. The probability of a incident ion interacting with an atomic electron, by crossing a distance Δx in the sample, and transferring to the electron an energy between T and $T + \delta T$ is given by:

$$P(T)dT = n_e \Delta x d\sigma \tag{A.4}$$

where $n_e = NZ_2$ is the electron density, the differential cross-section, $d\sigma$ is given by [Nastasi et al., 2014]

$$d\sigma(T) = 2\pi b db \tag{A.5}$$

and the relationship between the impact parameter b and the energy transferred T is given by [Nastasi et al., 2014]

$$T = \frac{2Z_1^2 e^4}{b^2 m_e v^2} \tag{A.6}$$

Thus, the mean squared average energy transferred can be given by:

$$\langle T^2 \rangle = \int T^2 P(T) dT = 2\pi N Z_2 \Delta x \frac{\left(Z_1 e^2\right)^2}{m_e v^2} \left(T_{\text{max}} - T_{\text{min}}\right) \tag{A.7}$$

where T_{max} and T_{min} refer to the energy transferred corresponding to an interaction with the minimum and maximum impact parameter b_{min} and b_{max}, respectively. Classically, the maximum energy transferred to the electron corresponds to a head-on collision (b_{min}), where $m_e << M_1$, given by $T_{\text{max}} = 2m_e v^2$. Taking the limit of $T_{\text{max}} >> T_{\text{min}}$, the Bohr value of electronic energy straggling is obtained:

$$\Omega_{\text{B}}^2 = 4\pi Z_1^2 e^4 N Z_2 \Delta x \tag{A.8}$$

Thus, in the same sample and distance transversed, a ^{4}He ion will have 4 times more the energy straggle than a ^{1}H ion, an important aspect to take into account in high-resolution ion beam analysis. As previously stated, Bohr's approach to the energy straggle is valid in the ion high-energy limit, where the energy loss straggle is independent of the ion energy. However, for lower ion energies equation A.8 ceases to be adequate and corrections are needed to take into account the deviations due to electron binding in the target atoms. As such, for lower energies the Bohr straggling value is multiplied by the Chu correction factor $H(E_1/M_1, Z_2)$, which decreases considerably the value of the statistical energy straggling component [Chu, 1976].

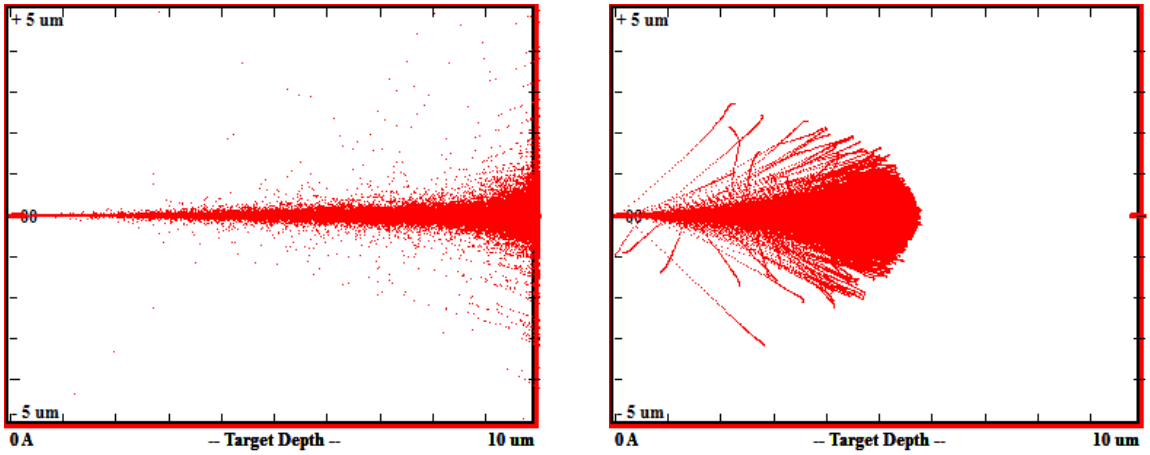

(a) (b)

Figure A.1: (a)Simulation of the trajectory of a 2 MeV proton ($M_1 = 1$, $Z_1 = 1$) and (b) helium ($M_1 = 4$, $Z_1 = 2$) (b) beam in a carbon ($M_1 = 12$, $Z_1 = 6$) sample with $10\,\mu m$ width.

The energy straggle effect also results in the variation of the distance transversed by individual ions on the target, which is called longitudinal straggle. Another important aspect to consider is the effect of the geometry, associated with the variations in the number of collisions, of the ion-electron interaction which provides transverse momentum to the ion, altering its trajectory in the transverse plane. This

phenomenon is called lateral straggle. Figures A.1a and A.1a present Monte-Carlo simulations, using SRIM [Ziegler et al., 2008], of the passage of 2 MeV ^{4}He and ^{1}H ions through a carbon ($M_2 = 12$, $Z_2 = 6$) sample where the effects of lateral straggling are clearly visible. The consideration of these effects are quite important in the planning of ion beam analysis, since they limit the possible values of depth and lateral resolution attainable. For RBS analysis, the depth and mass resolution obtainable is directly limited by the energy straggle (as well as experimental parameters such as the detector's resolution). Lateral straggling also defines the minimum spatial resolution obtained by the experimental setup, instead of the beam's spot size at the surface. Still, the lateral and depth resolution obtained by light MeV ion beam analysis is a significant improvement over electron analysis, and proves to be a powerful tool in attaining high-resolution, depth information of an unknown sample, and one of the leading approaches to obtain that is through RBS.

Appendix B

MORIA Functions

The analysis component of MORIA was complemented with the creation of several functions, accessible in the Visualization options panel (4) present in Figure 3.1, which are able to modify and extract information from the elemental model in real-time, serving as an assistance to the experimental data analyst. These functions are specific to 3D or 2D rendering and, as such, the Visualization options panel (4), present in Figure 3.1, is composed of two alternating sub-panels: `OptionsPanel_3D`, which includes all functions for 3D rendering, and `OptionsPanel_2D`, which includes the functions for 2D rendering. The review of the goal of functions for 3D, and 2D, analysis, along with the analysis of the internal mechanisms of each, are discussed in Appendix B.0.3, and B.0.4, respectively.

B.0.3 3D Functions

B.0.3.1 *Reset* Function

The most basic, and most commonly used, function in the MORIA program is the *Reset* function, which is responsible for resetting the model, if it has been subjected to any modification, and resetting the position and orientation of the active `vtkCamera` object to its default values. The flowchart describing the function's procedure is presented in Figure B.1.

Initially all `vtkProps`, such `VTK3D_Model_Actor` (modified or not), `VTK3D_Active_Camera` and the accessory props, are removed from `VTK3D_Renderer`, through the function `RemoveAllViewProps()` and the `VTK_RenderWinInt` is set to its default `vtkInteractorStyle`, given by `vtk3D_IntStyle_Default`. Afterwards, the default `vtkProps`, more precisely the default `VTK3D_Model_Actor` and accessory props, are added to the `VTK3D_Renderer`, as well as the `VTK3D_Active_Camera`, which takes the position and focal point values of `VTK3D_Default_Camera`, given by equations 3.20 and 3.21, respectively. Finally, the scene is presented through the calling of the renderer member function `Render()`.

B.0.3.2 *3D/2D* Function

The goal of this function is to alternate between the 3D, set by default, and the 2D rendering mode of MORIA, and vice-versa. The mechanism responsible for such change is presented in Figure B.2.

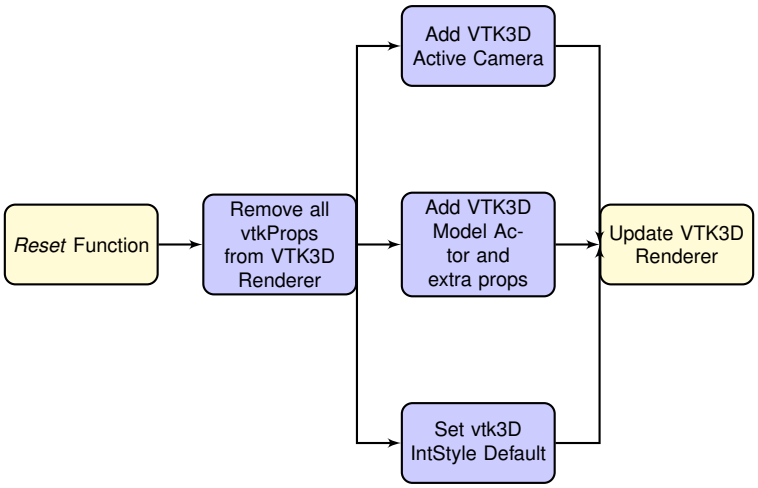

Figure B.1: Flowchart of the *Reset* Function

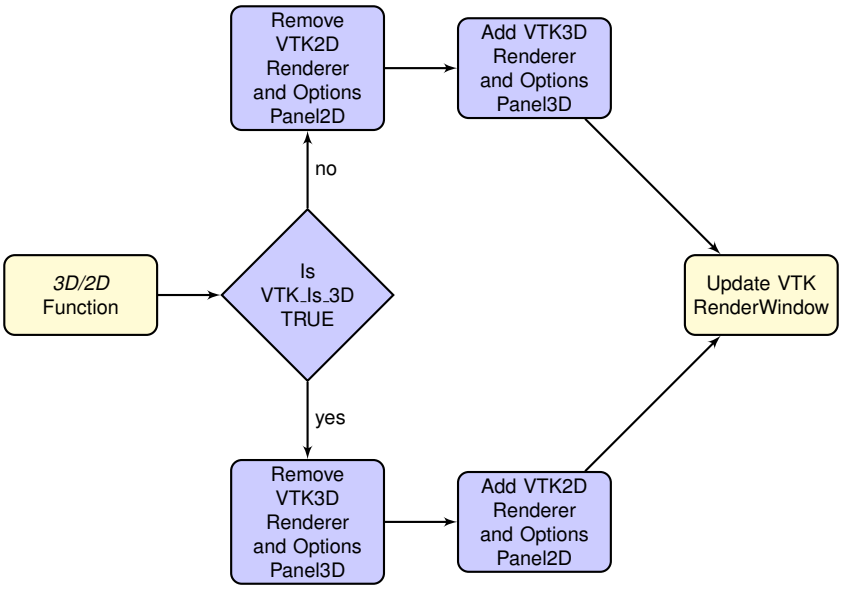

Figure B.2: Flowchart of the *3D/2D* function.

After selecting the function, the program identifies the current mode of rendering through the boolean variable `VTK_Is_3D`, which is taken as `TRUE` for the 3D rendering mode and `FALSE` for the 2D rendering mode. If `VTK_Is_3D=TRUE`, the `VTK3D_Renderer` is removed from `VTK_RenderWindow`, and subsequently `VTK2D_Renderer` is added to it. The option panel `OptionsPanel_3D` is also replaced by the `OptionsPanel_2D`. A similar procedure is applied in the case of `VTK_Is_3D=FALSE`, with `VTK2D_Renderer` being removed from `VTK_RenderWindow`, and `VTK2D_Renderer` being added to it. The options panel `OptionsPanel_2D` is also replaced by the default `OptionsPanel_3D` panel. In each case, the altered scene is presented through the calling of the VTK function `Render()`.

B.0.3.3 *Resolution* Function

The main goal of the *Resolution* function is the change in real-time of the number of cells in each layers, more precisely by selecting a new value of ΔG, defined by $\Delta G'$. The procedure is described in

Figure B.3.

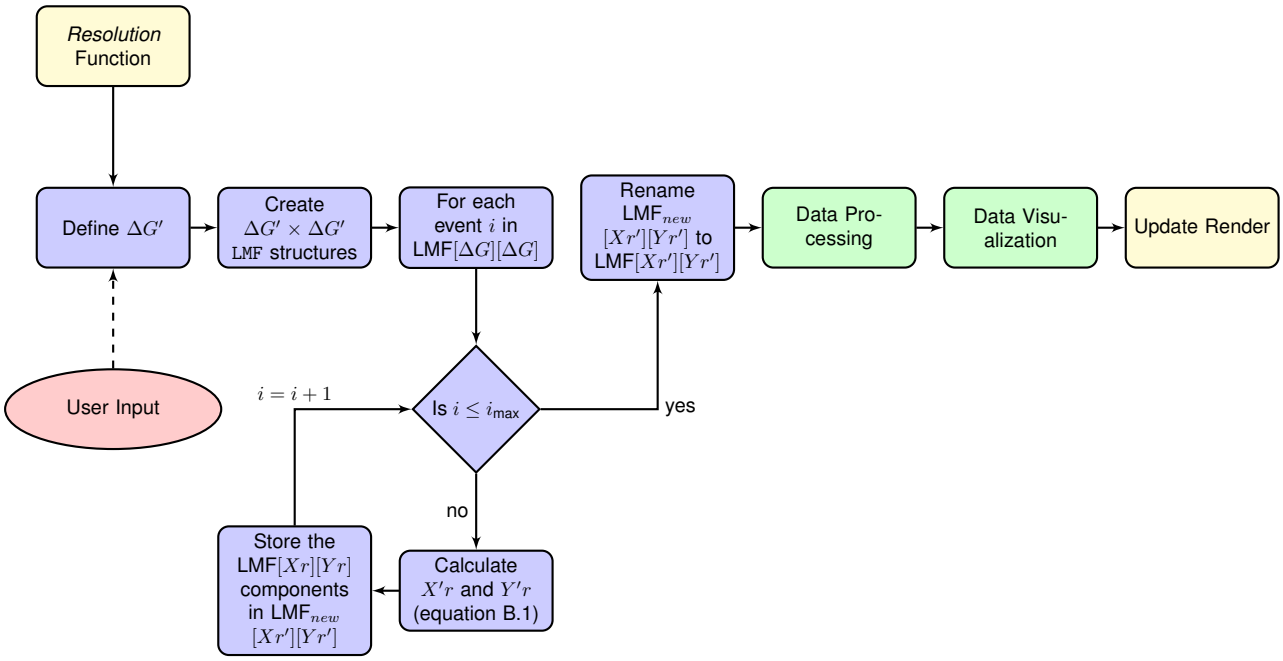

Figure B.3: Flowchart of the *Resolution* function.

The number of cells in each layer, previously defined as the grid dimensions, ΔG is a fundamental parameter in the MORIA analysis, which was introduced in the early discussion of the file input reading mechanism in Chapter 3.2.1. As such, after the selection of the new value $\Delta G'$ by the user, the procedure requires the creation of a new vector of structures LMF$_{\text{new}}[Xr'][Yr']$, defined in Figure 2.18, to store the energy values in the new coordinates, where the new reduced coordinates Xr' and Yr' are, similarly to equation 3.2, given by:

$$Xr'_i = \left\lfloor x_i \times \frac{256}{\Delta G'} \right\rfloor \ , \ Yr'_i = \left\lfloor y_i \times \frac{256}{\Delta G'} \right\rfloor \tag{B.1}$$

However, this procedure does not require any interaction with the initial user-chosen file, since the information regarding the coordinates of each event were stored in the original LMF$[Xr_i][Yr_i]$ structure, in the X and Y components correspondent to each E entry. As such, the new structure is initialized and filled, accordingly to Figure B.4:

After the new vector of structures LMF$'[Xr'][Yr']$ is created and filled, the data present in the old structure LMF$[Xr][Yr]$ is cleared and the structure itself is deleted. From this point, the analysis would be identical to the one presented in Chapters 3.2.2 and 3.2.3. However, in would require the creation of new functions designed for this structure, as the ones used before did not take into account the name of the new structure. So, in order to reduce programming complications, each LMF$_{\text{new}}[Xr][Yr]$ structure is copied to a new structure, once again named LMF$[Xr][Yr]$, which enables the use of the same chain of procedures and functions as before, discussed in depth in Chapters 3.2.2 and 3.2.3, to produce the visualization taking into account the updated value of $\Delta G = \Delta G'$.

for each event i **do**:

$Xr'_i \leftarrow \lfloor \text{LMF}[Xr_i][Yr_i].X(i) \times \frac{256}{\Delta G'} \rfloor$

$Yr'_i \leftarrow \lfloor \text{LMF}[Xr_i][Yr_i].Y(i) \times \frac{256}{\Delta G'} \rfloor$

$\text{LMF}_{\text{new}}[Xr'_i][Yr'_i].X' \leftarrow \text{LMF}\ [Xr_i][Yr_i]\,.X(i)$

$\text{LMF}_{\text{new}}[Xr'_i][Yr'_i].Y' \leftarrow \text{LMF}\ [Xr_i][Yr_i]\,.Y(i)$

$\text{LMF}_{\text{new}}[Xr'_i][Yr'_i].E' \leftarrow \text{LMF}\ [Xr_i][Yr_i]\,.E(i)$

Figure B.4: Pseudo-code of the new event storage algorithm in the *Resolution* function in MORIA.

B.0.3.4 *Relayer* Function

Using the *Relayer* function, the user is able to change the number of layers of the model, which by default is given by an integer multiple of the depth resolution as presented by equation 3.15. While the default method gives the maximum number of layers, in some cases, due to low number of events in each cells, a lower number of layers is preferable to analyse. The procedure of this function is presented in Figure B.5:

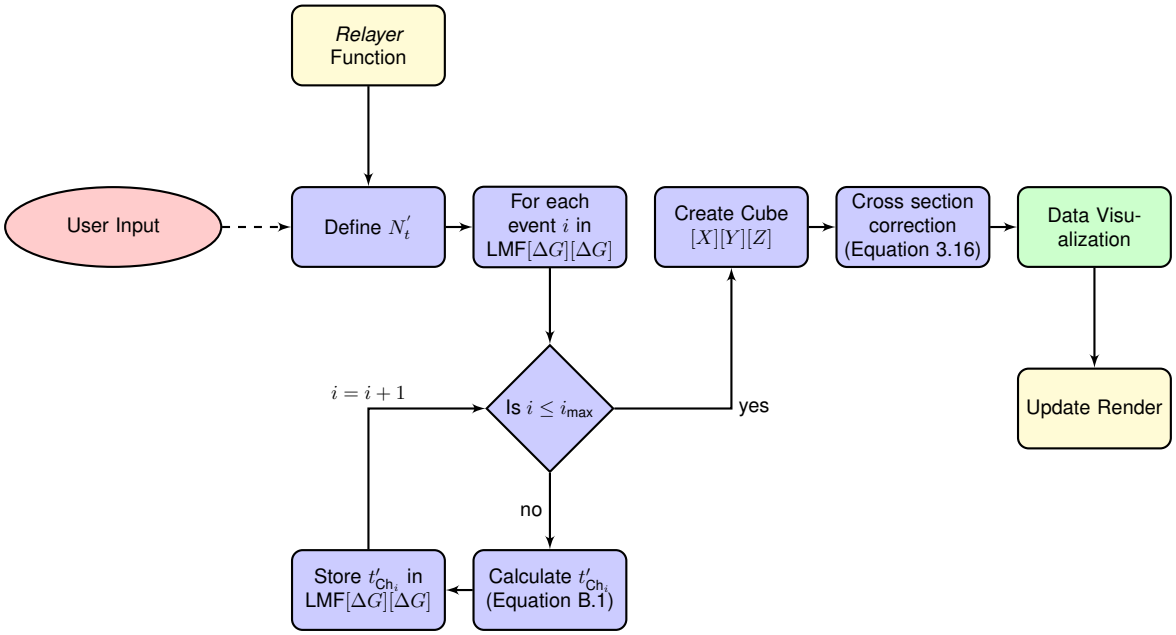

Figure B.5: Flowchart of the *Relayer* function.

Through the selection of a new number of layers, defined as $N_t^{'}$, also a new value of depth width $\Delta t'$ for each layer is defined, such that:

$$\Delta t' = \frac{t^{\text{Max}}}{N_t'} \tag{B.2}$$

where t^{Max} is the maximum depth achieved by the analysis, previously defined in Chapter 3.2.2. Thus, the values of the depth channel $\texttt{LMF}\ [Xr][Yr].T_{\text{CH}}$ associated to each depth $\texttt{LMF}\ [Xr][Yr].T_i$ must be updated. The mechanism for the update is presented in Figure B.6.

```
clear LMF [Xr_i][Yr_i].T_CH
for Xr, Yr ∈ [0, ΔG[
  for each event i
    t'_CH_i ← ⌊ LMF[Xr][Yr].T(i) / Δt' ⌋
    LMF [Xr][Yr].T_CH ← t'_CH_i
```

Figure B.6: Pseudo-code of the updated depth sorting algorithm of the *Relayer* function of MORIA.

From this point on, the procedure is analogous to the one described in Chapters 3.2.2 and 3.2.3.

B.0.3.5 *Sphereview* Function

The *Sphereview* rendering mode is an alternative rendering mode to the default rendering model, where each individual cell is not represented by a cube data object but by a sphere, whose color and radius is a function of the number of events in that cell. The procedure initiated with this function is presented in Figure B.7.

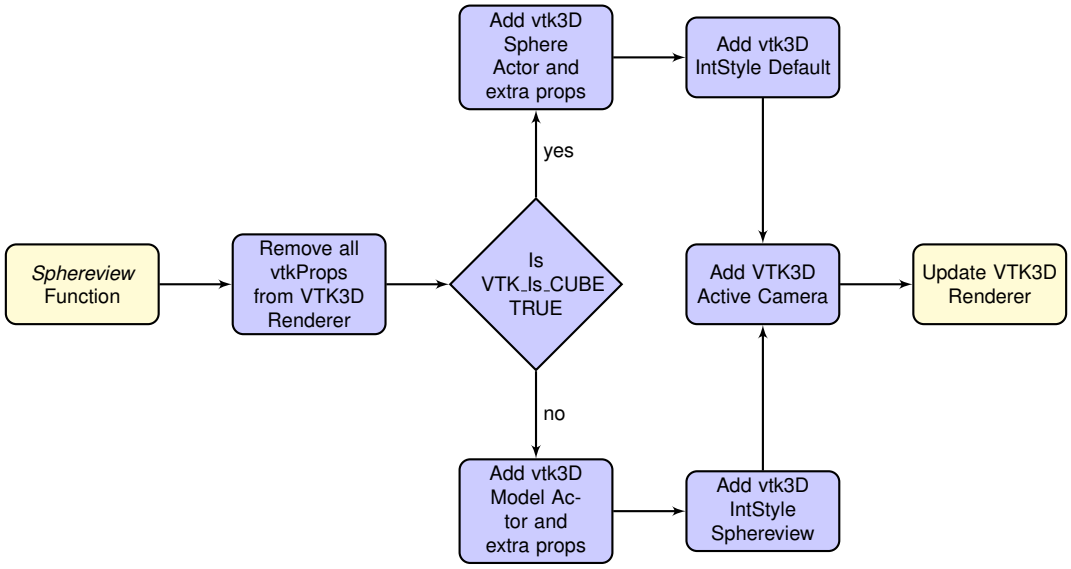

Figure B.7: Flowchart of the *Sphereview/Cubeview* function.

It is important to note that this function, similarly to the *3D/2D* function, serves as a mere switch to exchange the rendering `vtkProp` objects present in the `vtk3D_Renderer`, mediated through the boolean variable `VTK_Is_CUBE`. Indeed, although not presented in Chapter 3.2.3, the procedure responsible for the initialization this mode is done immediately after the initialization of the 2D rendering mode, which is now discussed in depth.

The process of creation of the `vtk3D_Sphere_Actor` is in all analogous to the creation of the default `VTK3D_Model_Actor`, discussed in Chapter 3.2.3. In this case, in order for each cell to be represented

by a sphere, the source data object to be used is the `vtkSphereSource` object, whose radius r_{SPHERE} is a function of the number of events in each cell, stored in the corresponding $\texttt{Cube}[X][Y][Z]$ vector, given by:

$$r_{\text{SPHERE}} = \begin{cases} \frac{\texttt{Cube}[X][Y][Z]}{n_{\text{ev}}^{\text{Max}}} \times \frac{\Delta S}{\Delta G} & \text{if } \frac{\Delta S}{\Delta G} < \delta t \times 10 \\ \frac{\texttt{Cube}[X][Y][Z]}{n_{\text{ev}}^{\text{Max}}} \times \delta t & \text{if } \frac{\Delta S}{\Delta G} \geq \delta t \times 10 \end{cases} \tag{B.3}$$

While the radius of each sphere translates visually the number of events, the information regarding this quantity is also presented through the color of the sphere. Thus, the same pipeline described in Chapter 3.2.3 is applied: each `vtkSphereSource` object, designed as a sphere *unit*, is translated into a `vtkPolyData` object, whose full set is combined into a single object through the use of a `vtkAppendPolyData` filter. Afterwards, the similar chain of mapper, `vtkPolyDataMapper`, and an actor, `vtk3D_Sphere_Actor`, is used.

Thus, in order to switch the `vtkActor` objects, after the selection of the function, all `vtkProp` elements are removed from `VTK3D_Renderer`, using the renderer member function `RemoveAllViewProps()`. If `VTK_Is_CUBE=TRUE` the `vtk3D_Sphere_Actor` is added to the 3D renderer `VTK3D_Renderer`, along with the accessory props (`vtkScalarBarActor`, `vtkLegendScaleActor` and the model bounding box). On the other hand, if `VTK_Is_CUBE=FALSE` it is the default `vtk3D_Sphere_Actor` that is added to the renderer. After the switch, the scene is renderer using the renderer member function `Render()`.

Also important to note, is the creation of a dedicated `vtkInteractorStyle`, named `vtk3D_IntStyle_Sphereview`, for this function, in order to simultaneous enable the identification of a sphere *unit*, selected through a double left mouse button, and presenting the user with information about it regarding its position and the number of events, while also enable the identification of its position on the Sample Map panel, panel (2) in Figure 3.1. The selection of the sphere *unit* is not trivial, as in the case of the *Cut* function, since due to the `vtkPolyData` appending procedure, the information regarding each individual *unit* is lost and the interactor, using the member function `FindPickedActor()`, is only able to identify the appended model. As such, by using the left mouse button, the coordinates of the intersection between a virtual ray emitted in the direction selected by the user and the full model (X_m, Y_m, Z_m) is stored and transformed into the regular *unit* coordinates (X, Y, Z), using:

$$X = X_m \frac{\Delta G}{\Delta S} \tag{B.4}$$

$$Y = Y_m \frac{\Delta G}{\Delta S} \tag{B.5}$$

$$Z = \frac{Z_m}{\delta t \times 10}, \tag{B.6}$$

After this selection, the chosen *unit* is highlighted, by superimposing on the default sphere model a single sphere *unit* model with diffuse lighting (`SetDiffuse(1.0)`) , and an information box is created, using the `vtkLegendBoxActor`, which presents the positional information of the *unit* and the number of events it represents. The highlighted actor and the information box is removed by using again the left mouse button.

B.0.3.6 *Sensitivity* Function

The *Sensitivity* Function serves as the implementation of a virtual minimum level of detection bias on the number of events presented in the visualization model. More precisely, this functions creates a new `vtkActor` object, named `vtk3D_Sense_Actor`, from `vtkCubeSource` sources corresponding to elements with `Cube`$[X][Y][Z]$ number of entries higher than an user-defined limit δn_e, such that:

$$\delta n_e \leq \frac{\text{Cube}[X][Y][Z]}{n_{\text{ev}}^{\text{Max}}} \tag{B.7}$$

where $\delta n_e \in [0, 1]$. The function's procedure is presented in Figure B.8.

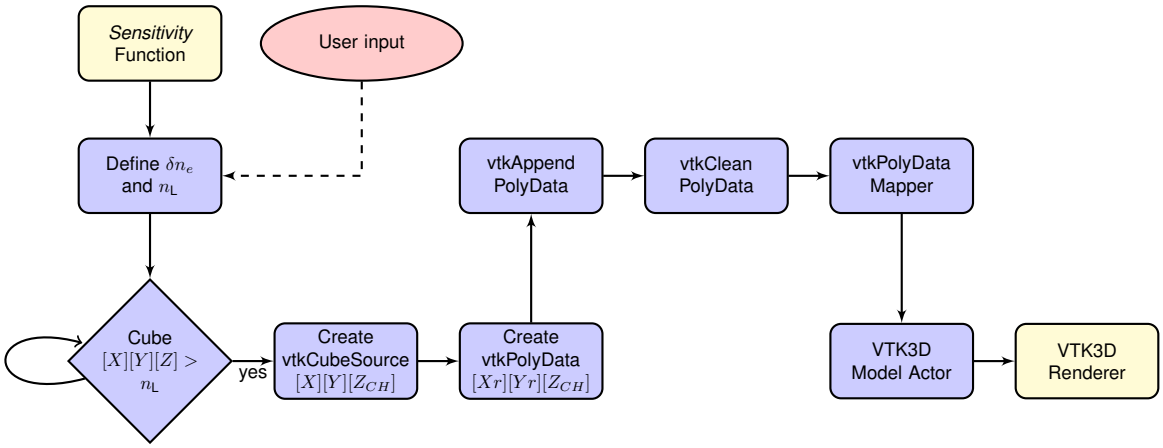

Figure B.8: Flowchart of the *Sensitivity* function.

As such, after translating each data source object into a `vtkPolyData` object, only `vtkPolyData` with number of entries higher than n_{L}, with $n_{\text{L}} = \delta n_e \times n_{\text{ev}}^{\text{Max}}$ will be appended, through the `vtkAppendPolyData` filter. Afterwards the same pipeline is used, composed of a mapper, `vtkPolyDataMapper`, and an actor, `vtk3D_Sense_Actor`. In order to update the renderer scene all `vtkProp` elements are removed from `VTK3D_Renderer`, using the `RemoveAllViewProps()` function, and subsequently the updated actor is added, along with the accessory props, and the scene is rendered, using the `Render()` function.

B.0.3.7 *Cut* Function

The goal of *Cut* function is to produce a cross-section model, in any vertical or horizontal direction, of the default elemental model. The procedure to accomplish that is presented in Figure B.9.

After selecting the function, the user directly chooses the initial and final point of the desired cut line. This is accomplished through a custom interaction style, named `VTK3D_Cut_IntStyle`, using the left mouse button. By selecting the left mouse button, the coordinates of the mouse in the screen for the initial point (X_{initial}, Y_{initial}) and for the final point (X_{final}, Y_{final}), obtained using the interactor function `GetEventPosition()`, are defined. Afterwards, the decision of the position and the orientation of the cut is made resorting to the highest difference between corresponding coordinates, such as presented in Figure B.10.

Please note that, in Figure B.10, the boolean variable `VTK_CUT_H`, which has `TRUE` value for a horizontal

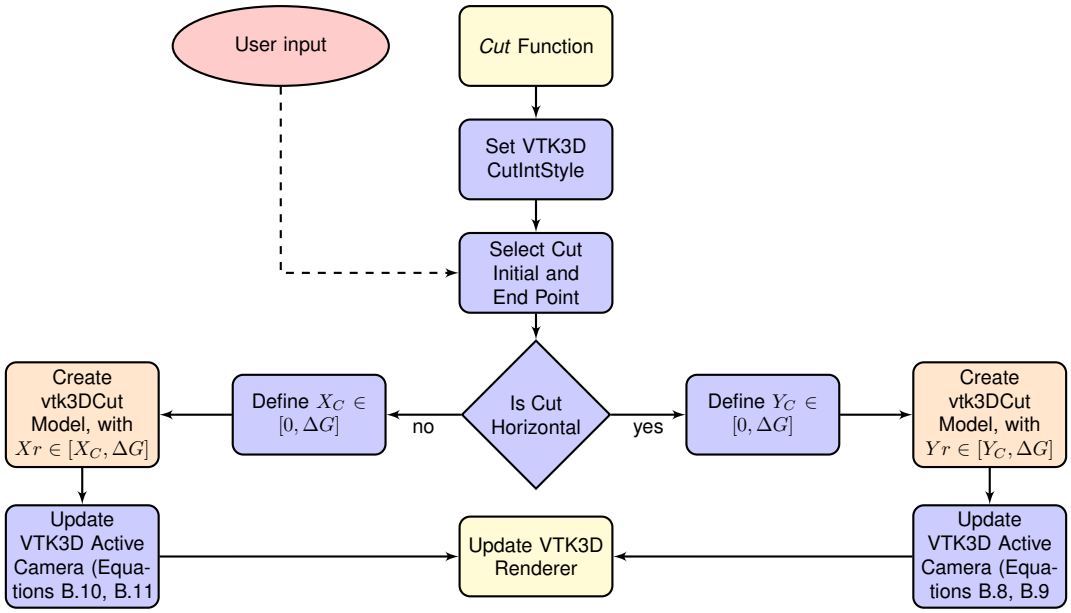

Figure B.9: Flowchart of the *Cut* function.

if $|X_{\text{initial}} - X_{\text{final}}| > |Y_{\text{initial}} - Y_{\text{final}}|$

VTK_CUT_H = TRUE

$Y_C = \lfloor (Y_{\text{initial}} + Y_{\text{final}})/2 \times \frac{\Delta G}{\Delta S} \rfloor$

if $|X_{\text{initial}} - X_{\text{final}}| < |Y_{\text{initial}} - Y_{\text{final}}|$

VTK_CUT_H = FALSE

$X_C = \lfloor (\rfloor X_{\text{initial}} + X_{\text{final}})/2 \times \frac{\Delta G}{\Delta S}$

Figure B.10: Pseudo-code of the cut selection procedure of the *Cut* function in MORIA.

cut and `FALSE` value for a vertical cut, represents the direction of the cut and (X_C, Y_C) the position of the cut in the $\Delta G \times \Delta G$ grid space. The procedure for the selection of the `vtkPolyData`, derived from the base `vtkCubeSource` data objects, that compose the updated model is presented in Figure B.11.
After the selection, the `vtkAppendPolyData` object is mapped into a `vtkActor` object, named `vtk3D_Cut_Model` and added into the 3D renderer. The position and focal point of the active camera object `VTK3D_Active_Camera` is also updated to allow the visualization of the traversal cut on the elemental model, according to the value of boolean variable `VTK_CUT_H`. If `VTK_CUT_H=TRUE`, then the position and focal point of the active camera is given by:

$$X_{\text{Cut Camera}} = \Delta S/2 \ , \ Y_{\text{Cut Camera}} = j \times \frac{\Delta S}{\Delta G} - 2.4\Delta S \ , \ Z_{\text{Cut Camera}} = \frac{t_{\text{CH}}^{\text{Max}} \times \delta t \times 10}{2} \tag{B.8}$$

$$X_{\text{FP}} = \Delta S/2 \ , \ Y_{\text{FP}} = j \times \frac{\Delta S}{\Delta G} \ , \ Z_{\text{FP}} = \frac{t_{\text{CH}_{Max}} \times \delta t \times 10}{2} \tag{B.9}$$

```
if VTK_CUT_H = TRUE
  for X ∈ [0, ΔG[ , Y ∈ [Y_C, ΔG[ , Z ∈ [0, t_CH^Max]
    vtkAppendPolyData ← vtkPolyData [X, Y, Z]

if VTK_CUT_H = FALSE
  for X ∈ [X_C, ΔG[ , Y ∈ [0, ΔG[ , Z ∈ [0, t_CH^Max]
    vtkAppendPolyData ← vtkPolyData[X, Y, Z]
```

Figure B.11: Pseudo-code of the source data object selection procedure of the *Cut* function in MORIA.

On the other hand, if `VTK_CUT_H=TRUE` the position and focal point of the camera is given by:

$$X_{\text{Cut Camera}} = j \times \frac{\Delta S}{\Delta G} - 2.4\Delta S \ , \ Y_{\text{Cut Camera}} = \Delta S/2 \ , \ Z_{\text{Cut Camera}} = \frac{t_{\text{CH}}^{\text{Max}} \times \delta t \times 10}{2} \tag{B.10}$$

$$X_{\text{FP}} = j \times \frac{\Delta S}{\Delta G} \ , \ Y_{\text{FP}} = \Delta S/2 \ , \ Z_{\text{FP}} = \frac{t_{\text{CH}}^{\text{Max}} \times \delta t \times 10}{2} \tag{B.11}$$

Finally, the scene is rendered using the `vtkRenderer` member function `Render()`.

B.0.3.8 *Surface Creator* Function

The main objectives of the *Surface Creator* function are the creation of a multi-elemental model, named `VTK3D_Surface_Model_Actor`, in order to display simultaneously with the default `VTK3D_Model_Actor`, and the identification of the areas where both models are superimposed, and the subsequent accounting of the number of events that occur in such areas. The function's procedure is described in Figure B.12.

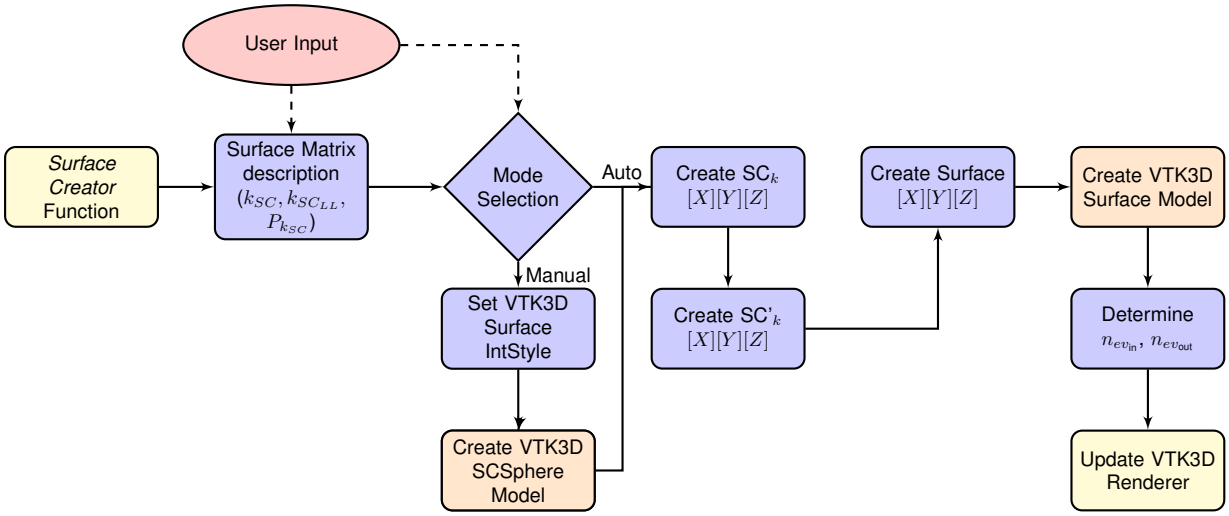

Figure B.12: Flowchart of the *Surface Creator* function.

Before the creation of the multi-elemental model, the choice of the k_{max} elements that compose the model k_{SC}, along with the lower energy limit $k_{SC_{LL}}$ and the preponderance of the element $P_{k_{SC}} \in [0, 1]$ in the model must me done by the user, in the dialog window presented after selecting the function. Afterwards, two different options exist for the creation procedure itself: manual creation, where the area of analysis is a function of the user input, and automatic creation, where the entire rendering space is considered for analysis.

In the manual creation option, the multi-elemental model will only be considered in an sphere area, whose radius and position are defined by the user input, more precisely through two consecutive left mouse button clicks. As such, a custom interaction style, defined as `VTK3D_Surface_IntStyle`, was created to enable the mouse inputs: after the selection of the position of the center of the analysis sphere, given by (X_{Cir}, Y_{Cir}), any mouse movement is registered and the provisional radius of analysis is presented through a circumference with coordinates (X_R, Y_R), defined using a `vtkRegularPolygonSource` data object and the common visualization pipeline composed of a `vtkMapper` and `vtkActor`, named `vtk3D_SC_Manual_Circ_Actor`. The circumference is superimposed on the elemental model and its radius is updated with each mouse movement. After the second left mouse button click, the final analysis radius is defined, given by equation:

$$R_{\text{SC}} = \sqrt{(X_{Cir} - X_R)^2 + (Y_{Cir} - X_R)^2} \tag{B.12}$$

Please note, that the depth coordinate is neglected in this construction, since the definition of the area is done at the surface level and, as such, radii $R_{\text{SC}} < 10t_{\text{CH}}^{\text{Max}}$ will not be able to take into account all layers of the model. After the area selection is done, a `vtk3D_SC_Manual_Circ_Actor` is removed from the renderer `VTK3D_Renderer` and replaced by `vtk3D_SC_Manual_Sphere_Actor`, derived from a `vtkSphereSource` data source object, with center (X_C, Y_C) and radius R_{SC}.

After the selection of the area of analysis, the procedure becomes the same for manual and automatic analysis and, as such, is discussed here for both methods. Initially, for each element k_{SC}, a specific 3D vector $\texttt{SC}_k[X][Y][Z]$, initially with all entries null, to hold the number of events in each depth channel, similar to the $\texttt{Cube}[X][Y][Z]$ vector , is created using the same procedure described in Chapter 3.2.2: the energy component of the vector storage structure $\texttt{LMF}[Xr][Yr].E(i)$ is analysed and events with energy between the surface energy of the chosen element E_{UL_k} and the surface energy of the lower-energy-limit element E_{LL_k}, given by equation 3.13, are selected. Subsequently, the corresponding depth t_i and depth channel position t_{CH_i} are determined, using equations 3.14 and 3.15 respectively, and the event increments by one the value present in the vector $\texttt{SC}_k[X][Y][Z]$, with $X = Xr$, $Y = Yr$ and $Z = t_{\text{Ch}_i}$. This process is repeated for all k_{max} elements.

The number of events in each depth channel is not a preponderant factor for the creation of the multi-elemental model, since the goal of the function is not the study of the distribution of the elements in a new model but to present the volume where the chosen elements exist. As such, for each k element,

the value of $\texttt{SC}_k[X][Y][Z]$ is changed to $\texttt{SC'}_k[X][Y][Z]$ accordingly to:

$$\text{SC'}_k[X][Y][Z] = \begin{cases} 0 & \text{if SC}_k[X][Y][Z] = 0 \\ 1 & \text{if SC}_k[X][Y][Z] \neq 0 \end{cases} \tag{B.13}$$

Finally, the last step before the creation of the surface model is the decision of the volume of the model, described by the non-null entries $\texttt{Surface}[X][Y][Z]$ vector, made using the pondered sum over the number of entries of the elements in each $[X][Y][Z]$ position, taking into account the preponderance $P_{k_{SC}}$ of each element in the surface. The decision variable $D_{[X][Y][Z]}$ for each position, is given by:

$$D_{[X][Y][Z]} = \frac{\sum_0^{k_{max}} \text{SC'}_k[X][Y][Z] \times P_{k_{SC}}}{k_{max}} \tag{B.14}$$

where $D_{[X][Y][Z]} \in [0, 1]$. As such, if $D_{[X][Y][Z]} \leq 0.5$, $\texttt{Surface}[X][Y][Z] = 0$, else $\texttt{Surface}[X][Y][Z] = 1$. After this selection, the surface model can be created, using a similar procedure to the one discussed in Chapter 3.2.3: for each position defined by $[X][Y][Z]$, with a corresponding non-null entry in $\texttt{Surface}_k[X][Y][Z]$, a `vtkCubeSource` data object, with dimensions defined in equations 3.18 and 3.19, is mapped to a `vtkPolyData` object. Please note that the model presents a uniform white color, since no information regarding the number of entries in each object is required. Also, this procedure is simultaneously able to determine the number of events from the elemental model `VTK3D_Model_Actor` that are contained in the *units* of the surface model `VTK3D_Surface_Model_Actor`, in order to give an estimation of the amount of events that are on the surface model, $n_{ev_{\text{on}}}$, and outside of the surface model, $n_{ev_{\text{out}}}$, from the total number of events $n_{ev_{\text{tot}}}$. The procedure to do so is presented in Figure B.13.

$n_{ev_{\text{on}}} = n_{ev_{\text{out}}} = n_{ev_{\text{tot}}} = 0$

for $X \in [0, \Delta G[\,, Y \in [0, \Delta G[\,, Z \in [0, t_{\text{CH}}^{\text{Max}}]$

  $n_{ev_{\text{tot}}} = n_{ev_{\text{tot}}} +$ Cube$[X][Y][Z]$

  if Surface+$[X][Y][Z] = 1$

    $n_{ev_{\text{on}}} = n_{ev_{\text{on}}} +$ Cube$[X][Y][Z]$

Figure B.13: Pseudo-code of the determination of the position of the events in regards to the surface model in the *Surface Creator* function in MORIA.

The percentage of events that are on P_{on} and outside P_{out} the surface model are determined accordingly to equation:

$$\begin{aligned} P_{\text{on}} &= \frac{n_{ev_{\text{on}}}}{n_{ev_{\text{tot}}}} \\ P_{\text{out}} &= \frac{n_{ev_{\text{tot}}} - n_{ev_{\text{on}}}}{n_{ev_{\text{tot}}}} \end{aligned} \tag{B.15}$$

These values are presented in a dialog window accessible from the main window of the function.

Please note that these quantities does not signify the number of events that exist in a regular volume, such as inside a spherical cellular wall of an organism, but only the number of events whose coordinates are common to the surface model *units*. Continuing the visualization pipeline, the multiple `vtkPolyData` objects are then appended into a single object, using the `vtkAppendPolyData` filter. In order for `VTK3D_Surface_Model_Actor` to have a more continuous aspect, instead of the *blocky* look of the default model, the `vtkAlgorithm` pipeline is composed of a `vtkCleanPolyData` filter, which is able to merge duplicate points, remove unused points and remove degenerate cells in the appended model, a `vtkFeatureEdges` filter to extract only the edges of the input polygonal data, ending in the usual `vtkPolyDataMapper`, responsible for mapping the data into the `VTK3D_Surface_Model_Actor`. In order to be able to easily distinguish the two models in the scene, the actor's transparency is set to 70% using the `vtkActor` member function `GetProperty()->SetOpacity(0.3)`. Finally, the actor is added to the renderer and the scene is presented using the `vtkRenderer` member function `Render()`.

B.0.3.9 *Save Render* Function

The *Save Render* function serves as a capture tool to save the rendering scene in an high-resolution PNG image file. The function's mechanism is presented in Figure B.14.

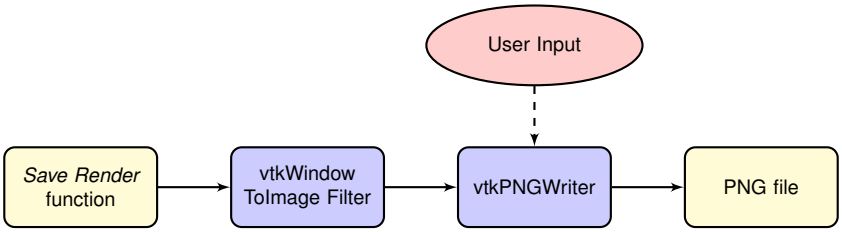

Figure B.14: Flowchart of the file input and reading mechanism in MORIA.

The rendering scene is first saved using a `vtkWindowToImageFilter` filter, which reads the data in the rendering window `VTK_RenderWindow` in RGBA (Red-Green-Blue-Transparency) channels and use it as input to the further imaging pipeline. After the data is read, a custom dialog window is created, in order for the user to specify the path of the image file. Finally, the PNG file is created at the selected path, using a `vtkPNGWriter` class object, a subclass of the global `vtkImageWriter`.

B.0.4 2D Functions

Although more limited in scope, the 2D rendering mode also includes specific functions to control the depth channel represented in the scene and to save the rendering scene, which is identical to the function discussed in Chapter B.0.3.9.

B.0.4.1 *Up* and *Down* Functions

The main goal of the *Up* and *Down* functions is to control the depth that the `VTK2D_Model_Actor` corresponds to and, as such, their procedure is almost identical, which is presented in Figure B.15.

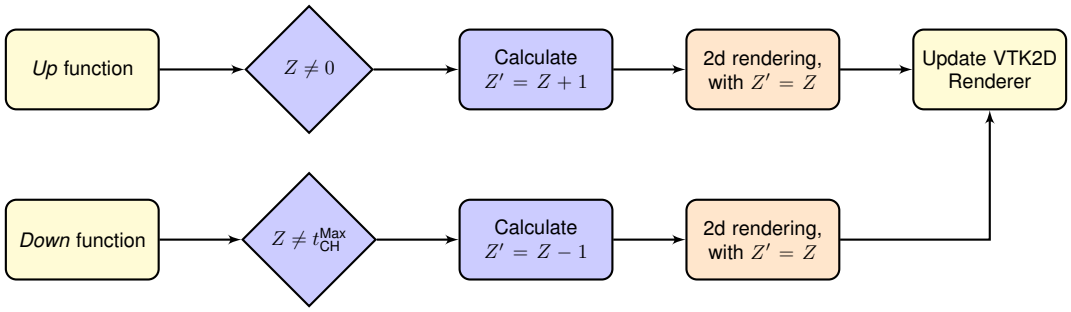

Figure B.15: Flowchart of the file input and reading mechanism in MORIA.

For a `VTK2D_Model_Actor` corresponding to a given Z, the *Up* function renders the model for $Z' = Z-1$, if $Z \neq 0$ and the *Down* function renders the model for $Z' = Z+1$, if $Z \neq t_{CH}^{Max}$. Once again, the model creation procedure is identical to the one discussed in Chapter 3.2.3 for the 2D rendering mode, now taking into account the updated value of Z' in the color mapping of the multiple `vtkPolyData` objects, using the defined `vtkLookupTable` mapping table. Afterwards, the `vtkPolyData` objects are appended into a single object, using the `vtkAppendPolyData` filter. The previous model is removed from the 2D renderer `VTK2D_Renderer`, and the updated `VTK2D_Model_Actor`, mapped from the `vtkAppendPolyData` output object using an instance of `vtkPolyDataMapper`, is added to the renderer. Finally, the scene is rendered using the `vtkRenderer` member function `Render()`.

Appendix C

Additional Information

The MORIA installation package (`Moria.rar`), available for Windows operative systems, contains the program installation executable (`Setup_Moria.rar`) and an auxiliary installation guide (`Moria_Guide.pdf`). The installation executable is responsible for the installation of the following items:

- `MORIA.exe` - The main executable of the program.
- `Manual.pdf` - The program's manual, available in the installation sub-folder "*Documents*", containing a simple description of the program interface and its functions.
- `Tutorial.pdf` - A walk-through example of an application of the program to a biological sample.

The program also includes an example of `.LMF` file, for testing purposes: `S1.LMF`, containing 2 *Saccharomyces cerevisiae* cells exposed to cooper-oxide nanoparticles.